#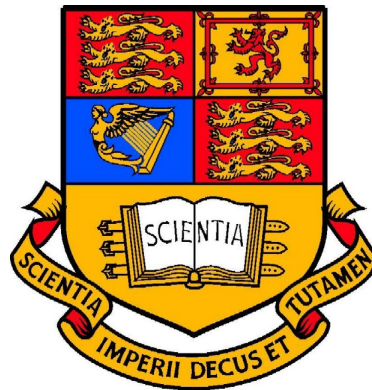 A Search for Supersymmetry in Events with Photons and Jets from Proton-Proton Collisions at $\sqrt{s} = 7\,\mathrm{TeV}$ with the CMS Detector

Robin James Nandi

High Energy Physics

Blackett Laboratory

Imperial College London

A thesis submitted to Imperial College London

for the degree of Doctor of Philosophy

and the Diploma of Imperial College.

May 2012

Abstract

An exclusion of Gauge Mediated Supersymmetry Breaking at 95% confidence level is made in the squark mass vs gluino mass parameter space using $1.1\,\mathrm{fb}^{-1}$ of proton-proton collisions data from the Large Hadron Collider. The event selection is based on the strong production signature of photons, jets and missing transverse energy. Missing transverse energy is used to distinguish signal from background. The background is estimated with a data driven technique. The CLs method is used to exclude models with squark mass and gluino mass up to around $1\,\mathrm{TeV}$.

Declaration

This thesis is my own work. Information taken from other sources is appropriately referenced.

Robin J. Nandi

Acknowledgements

Contents

List of Figures

8

List of Tables

Chapter 1

Introduction

The Large Hadron Collider (LHC) [13] was built to explore the TeV energy scale with proton-proton collisions to increase our understanding of particle physics. Two general purpose detectors at the LHC, the Compact Muon Solenoid (CMS) [6] and A Toroidal LHC AparatuS (ATLAS) [14], were designed specifically for this purpose. The main focus of the analysis at these experiments in terms of new physics has been to search for the Higgs boson, which is predicted by the electroweak theory in the Standard Model (SM) [15] but has not been observed, and Supersymmetry (SUSY) [16] which is a theory of new physics beyond the SM which seeks to solve the hierarchy problem [17].

SUSY is a theory with many parameters and many possible experimental signatures depending on the value of these parameters. This thesis searches for a restricted set of SUSY models in the data based on the experimental signature of photons, jets and missing transverse energy ($\gamma + \text{jets} + \not{E}_T$) and puts a limit on the cross-section of these models. The exclusion limit is compared with the results of other analyses looking at the same models.

The introductory section below sets out the units and conventions used in this thesis which are standard in particle physics and an outline of the thesis is given.

1.1 Units and Conventions

In this thesis natural units are used ($c = \hbar = 1$) to naturally embody special relativity and quantum effects. So all energies, momenta and masses are given in units of energy

(e.g. GeV).

For lengths and times where special relativity is not important (e.g. detector size) metres (m) and seconds (s) will be used.

Greek letters (e.g. α, μ) are reserved for Lorentz indices and take values 0, 1, 2, 3 with the 0-index corresponding to the energy/time component and the other indices corresponding to the momentum/spatial components.

Latin letters (e.g. a, i) are used for all other index requirements.

Following Einstein's summation convention repeated indices are summed over. For example, the component of the spin s_a in the direction of the momentum p_a, known as the helicity, can be written as in Equation 1.1.

$$
\begin{aligned}
\frac{s_a p_a}{\sqrt{p_a p_a}} &= \frac{s_1 p_1 + s_2 p_2 + s_3 p_3}{\sqrt{p_1 p_1 + p_2 p_2 + p_3 p_3}} \\
&= \frac{\vec{s} \cdot \vec{p}}{|\vec{p}|}
\end{aligned}
\tag{1.1}
$$

When Lorentz indices are involved use of the Minkowski metric, $\eta_{\mu\nu} = \mathrm{diag}(1, -1, -1, -1)$, is implied. In this thesis there is no distinction between "up" indices (e.g. p^μ) and "down" indices (e.g. p_μ). For example, the invariant mass squared of a particle with four-momentum p_μ is $p_\mu p_\mu$ (Equation 1.2).

$$
\begin{aligned}
p_\mu p_\mu &= p_0 p_0 - p_1 p_1 - p_2 p_2 - p_3 p_3 \\
&= E^2 - |\vec{p}|^2 \\
&= m^2
\end{aligned}
\tag{1.2}
$$

Spherical polar co-ordinates (r, θ, ϕ) are used for detector co-ordinates. The nominal interaction point at the centre of the detector is (0, 0, 0). The beam axis is the z-axis.

Often pseudorapidity η is used in place of θ: there is a one-to-one mapping between the two. Pseudorapidity is defined in Equation 1.3. The backward direction, parallel to the beam pipe, has $\theta = 0$ and $\eta = -\infty$. The forward direction, also parallel to the beam pipe,

14

has $\theta = \pi$ and $\eta = +\infty$. The direction perpendicular to the beam pipe has $\theta = \frac{\pi}{2}$ and $\eta = 0$.

$$\eta = -\ln \tan \frac{\theta}{2} \tag{1.3}$$

There is a difference between detector pseudorapidity defined with respect to the nominal interaction point and the pseudorapidity of a particle, which is measured with respect to the interaction vertex. Pseudorapidity is closely related to the rapidity, y, which is given by Equation 1.4. The rapidity has the useful property that it is invariant under Lorentz boosts along the z-axis. For relativistic particles ($E \gg m$), the pseudorapidity is equivalent to the rapidity.

$$y = \frac{1}{2} \ln \frac{E + |p_z|}{E - |p_z|} \tag{1.4}$$

Cylindrical co-ordinates (ρ, z, ϕ) are used to describe radius from the beampipe and position of primary vertices from the interaction point.

Abbreviations

Abbreviations are defined as they are introduced. The more comonly used abbreviations are listed here:

- LHC: Large Hadron Collider – the machine which collides protons at $7\,\mathrm{TeV}$ centre-of-mass energy.

- CMS: Compact Muon Solenoid – the detector which recorded the proton-proton collisions data used in this thesis.

- SM: Standard Model – the current theory of particle physics which describes the properties and interactions of the fundamental particles.

- MC: Monte Carlo – simulated data using random numbers to generate probability distributions.

- ECAL: Electromagnetic Calorimeter – the part of the CMS detector which measures the energy of electrons and photons.

- HCAL: Hadronic Calorimeter – the part of the CMS detector which measures the energy of hadronic particles.

- SUSY: Supersymmetry – a theory which proposes a symmetry between bosons and fermions.

- GMSB: Gauge Mediated SUSY Breaking – the mechanism of SUSY breaking considered in this thesis.

1.2   Outline of this thesis

This thesis describes a search for Gauge Mediated SUSY Breaking (GMSB) in events with photons, jets and missing transverse energy from proton-proton collisions data at centre-of-mass energy $\sqrt{s} = 7\,\mathrm{TeV}$ taken by the Compact Muon Solenoid (CMS) detector.

The theory of the standard model of particle physics is outlined placing emphasis on the structure of the theory and giving the key experimental results that support the theories. Problems with the standard model and reasons to expect to find new physics at the TeV scale are considered. SUSY is introduced as a possible extension to the standard model which solves the problem of the theoretical calculation of the Higgs boson mass being a divergent series. The particular flavour of SUSY considered in this thesis, GMSB, is introduced along with its parameters. Previous results on the exclusion of GMSB from LEP, Tevatron and LHC are mentioned.

The CMS detector is described focussing particularly on those aspects which are relevant to this thesis. The key performance measures for each component of the detector are given. Justifications have been made for design choices and the implications for this analysis have been given to put the information in context. The trigger and computing model which are important aspects of the data taking and analysis are also described. The reconstruction of photons and jets, the main physics objects used in this analysis, are detailed along with the selection variables associated with these physics objects.

The dataset and trigger used in this search are described. Simulated data are examined and compared to the experimentally observed data to establish what the simulation mod-

els well and what it does not. The event selection is motivated by the signature of GMSB: photons, jets and missing transverse energy. The object selection cuts are listed and the event varibles used to search for GMSB are examined.

The background to the search comes mainly from QCD processes which have fake missing transverse energy due to the detector resolution. The sources of background are listed and their properties and relative sizes are examined. Simulated samples are used to validate the data-driven QCD background model and estimate the small electroweak backgrounds.

The prediction of the number of signal events is made and all the sources of systematic uncertainty are considered. A range of possible signals with different parameters are considered. The signal efficiency is determined by applying the event selection to the simulated data. The sources of systematic uncertainty are investigated and their effect on the signal prediction is evaluated.

The CLs method [18] is used to determine the magnitude of the signal that can be excluded at 95% confidence level. An exclusion plot in GMSB parameter space is given based on this analysis and compared with other analyses looking at the same signal.

1.3   Other Work

In a collaboration the size of CMS, no one's work is independent. Everyone relies on the work of others for the detector operation, the data taking, the trigger, the object reconstruction, the jet energy corrections etc. With the exception of these obvious examples, almost all the work presented in this thesis is my own including the event selection, the background estimation, the signal prediction, the determination of systematic uncertainties and the limit setting. The only exceptions are the cross-section calculations and corresponding uncertainties in Section 6.6 and the photon efficiency correction in Section 6.2.

In addition to the work included in this thesis, I also worked on anomalous energy deposits in the electromagnetic calorimeter and a technique to measure the missing transverse energy in W events, which is important for the W cross-section measurement, using $Z \rightarrow ee$

events from data.

Chapter 2

Theory

2.1 Introduction

In this chapter a brief historical background of the standard model (SM) is given with some of the results that inform our current understanding. The role of symmetry in particle physics is discussed and the gauge structure of the SM is examined. The motivation for new physics at the TeV scale is considered. A brief description of supersymmetry, a popular possible extension to the SM, is given and the ideas behind it are discussed. Finally, the current exclusion limits on GMSB are reviewed.

2.2 The Standard Model

The SM of particle physics [19, 20, 21] contains our knowledge of the fundamental particles and the forces between them. Figure 2.1 shows the fundamental particles and the force carriers according to our current knowledge.

Historically the SM was formed by trying to understand atomic spectra. In 1928 Dirac came up with the Dirac equation to describe electrons [22], which was the first theory to deal with relativity and quantum mechanics. Later QED a theory of the interactions of light with matter was developed by Richard Feynman (among others) [23] which explained the Lamb shift in Hydrogen [24] and made a very precise prediction for the magnetic moment of the electron [25].

The neutrino was postulated by Pauli in 1930 [26] to explain the continuous electron en-

Figure 2.1: The fundametal particles according to the SM. Reproduced from [1].

ergy spectrum in β-decay. The neutrino was discovered by direct detection in 1956 [27] by inverse beta decay in a huge detector of water with CdCl$_2$ dissolved in it next to the Savannah River nuclear reactor. Three flavours of neutrinos corresponding to each of the leptons has been discovered. More recently neutrino oscillations have been observed in which neutrinos can change flavour [28]. The flavour change happens due to a difference between the mass eigenstates and the flavour eigenstates indicating that neutrinos have a non-zero mass.

After the discovery of many new hadrons, e.g. π, K, Δ, Σ, it became clear that the neutron and proton are not fundamental particles, but made up of more basic constituents. Gell-Mann and Zweig independenty came up with the quark model in which all hadrons are made up of quarks [29]. There are 6 flavours of quarks with different masses: u, d, c, s, t, b. Each flavour of quark comes in three different colors. Quarks carry color charge and form an SU(3) color triplet. Quarks are not observed as free particles, but only in colorless bound states.

An experiment by C. S. Wu and collaborators [30] showed that parity is violated in weak interactions. The beta decay of Co^{60} was performed in a magnetic field and at low temperature to polarise the nuclei and the angular distribution of electrons was measured. An asymmetry in the distribution between θ and $180° - \theta$ (where θ is the angle between the electron momentum and the orientation of the parent nucleus) was observed providing unequivocal proof that parity is not conserved in beta decay. This is represented in the SM by the vector minus axial vector structure of the weak interaction and the consequent presence of chiral fermions.

Electroweak theory was introduced by Glashow, Salam and Weinberg [31, 32] who proposed that the electromagnetic force and the weak force are parts of the same theory. The $W^{\pm}$ and Z^0 bosons were predicted to have have masses in the ratio $\frac{m_W}{m_Z} = \cos\theta_W$, where θ_W is the weak mixing angle. The $W^{\pm}$ and Z^0 bosons were discovered by the UA1 and UA2 experiments [33] at CERN. Carlo Rubbia and Simon van der Meer won the Nobel Prize for Physics in 1983 for their decisive contributions toward the discovery.

The Large Electron Positron Collider (LEP) [34] made e^+e^- collisions to search for new physics and make precision electroweak measurements. The collision centre of mass energy could be tuned to generate many Z bosons. Looking at the Z width for decays to invisible particles relative to the total Z width indicates that there are exactly three flavours of neutrino into which the Z can decay [35].

2.3 Gauge Symmetries of the SM

There is an important connection between symmetries and conservation laws discovered by Noether [36].

For every symmetry of the theory there is a conserved quantity.

Invariance under translations in time and space give rise to energy and momentum conservation. Invariance under rotation gives rise to conservation of angular momentum. Together with Lorentz invariance and parity these transformations form the Poincaré group. Describing symmetries in terms of group theory was developed by Galois in the 19th Century and was initially used to test the solvability of polynomial equations [37]. These

symmetries are all global, meaning that the transformation is the same for all space-time points.

A theory can be described by a Lagrangian which is equal to the kinetic energy minus the potential energy. The equations of motion of such a theory can be derived by minimising the action (Equation 2.1).

$$S = \int L d^4 x^{\mu} \tag{2.1}$$

Consider a Lagrangian with N scalar fields $\phi(x^{\mu}) = (\phi_1(x^{\mu}), ..., \phi_N(x^{\mu}))$, where x^{μ} is the space-time co-ordinate as in Equation 2.2.

$$L = L(\phi, \partial_{\mu}\phi, x^{\mu}) \tag{2.2}$$

Suppose that this Lagrangian is invariant under the gauge transformation given in Equation 2.3, where the phase is composed of the parameters $\epsilon^a (x^{\mu})$ and the generators of the Lie group T^a. This is a local gauge symmetry rather than a global symmetry since the phase depends on the space-time point.

$$\phi(x^{\mu}) \rightarrow \phi(x^{\mu}) e^{-i\epsilon^a T^a} \tag{2.3}$$

Noether's theorem gives a powerful way of constructing theories based on symmetry which underpins the structure of the standard model. The gauge symmetry of the SM is $SU(3) \times SU(2) \times U(1)$ [38, 39]. SU(3) corresponds to QCD and $SU(2) \times U(1)$ corresponds to the electroweak sector. The gauge structure and matter fields constitute the SM.

2.3.1   Quantum Electrodynamics (QED)

The QED Lagrangian for electromagnetic interactions of electrons can be written as Equation 2.4.

$$L = -\frac{1}{4} F_{\mu\nu} F_{\mu\nu} + \bar{\psi} \gamma_{\mu} D_{\mu} \psi - m_e \bar{\psi} \psi \tag{2.4}$$

The first term represents the free electromagnetic field. $F_{\mu\nu} = \partial_{\mu}A_{\nu} - \partial_{\nu}A_{\mu}$, where A_{μ} is the electromagnetic vector potential. The second term represents the electron kinetic energy and the interaction between electron and photon. $D_{\mu} = \partial_{\mu} - ieA_{\mu}$ is the covariant

22

derivative (i.e. it transforms in the same way as ψ under the gauge transformation). The third term represents the mass of the electron. This Lagrangian is invariant under the U(1) gauge transformation given by Equation 2.6.

$$
\begin{aligned}
\psi &\rightarrow e^{-i\alpha(x)}\psi & (2.5) \\
A_\mu &\rightarrow A_\mu + \frac{1}{e}\partial_\mu\alpha(x) & (2.6)
\end{aligned}
$$

The mass term for the electron is allowed by gauge invariance, but a mass term for the photon is forbidden. Also photon self-interactions are forbidden by gauge invariance. The constraints set by experiments and embodied in gauge invariance describe well the nature of the electromagentic interaction. The photon is a massless particle which interacts with electrons, but not with itself. The electromagnetic force has infinite range.

QED has been tested to very high precision. Consider the magnetic moment of the electron given by Equation 2.7.

$$
\vec{\mu} = -\frac{g\mu_B\vec{S}}{\hbar} \tag{2.7}
$$

where μ_B is the Bohr magneton, $\hbar$ is the Planck constant, $\vec{S}$ is the electron spin and g is a constant factor.

According to Dirac's theory $g = 2$, however QED predicts quantum corrections to this value. The QED prediction agrees with the experimentally measured value [23] to more than 10 significant figures:

$$
\frac{g-2}{2} = 0.00115965218073(28) \tag{2.8}
$$

2.3.2 The Electroweak Sector

The symmetries of the electroweak interaction are SU(2) weak isospin and U(1) hypercharge. SU(2) is the special unitary group of 2×2 matrices U satisfying $UU^\dagger = I$ and $det(U) = 1$. The generators of SU(2) are the Pauli matrices σ_a, $a = 1, 2, 3$, which are given in Equation 2.9.

Group	Fields	Strength	Generators
SU(2)	A_μ^a	g	$T^a = \frac{\sigma^a}{2}$
U(1)	B_μ	g'	$Y = \frac{1}{2}$

Table 2.1: Definitions of the symbols represting the properties of the electroweak groups. $a = 1, 2, 3$ and σ^a are the Pauli matrices.

$$\sigma_1 = \begin{pmatrix} 0 & 1 \\ 1 & 0 \end{pmatrix} \qquad \sigma_2 = \begin{pmatrix} 0 & -i \\ i & 0 \end{pmatrix} \qquad \sigma_3 = \begin{pmatrix} 1 & 0 \\ 0 & -1 \end{pmatrix} \tag{2.9}$$

Table 2.1 defines the symbols for the groups of the electroweak sector of the SM, the corresponding fields and the generators.

Consider a scalar field, ϕ, which is a doublet with respect to SU(2) and with U(1) hypercharge $Y = \frac{1}{2}$. The bosonic sector of the electroweak lagrangain can be written as:

$$L = -\frac{1}{4} F_{\mu\nu}^a F_{\mu\nu}^a - \frac{1}{4} G_{\mu\nu} G_{\mu\nu} + (D_\mu \phi)^\dagger (D_\mu \phi) - \lambda \left(\phi^\dagger \phi - \frac{v^2}{2} \right)^2 \tag{2.10}$$

where

$$F_{\mu\nu}^a = \partial_\mu A_\nu^a - \partial_\nu A_\mu^a + g\epsilon^{abc} A_\mu^b A_\nu^c \tag{2.11}$$

$$G_{\mu\nu} = \partial_\mu B_\nu - \partial_\nu B_\mu \tag{2.12}$$

$$D_\mu \phi = \partial_\mu \phi - i\frac{g}{2} \sigma^a A_\mu^a \phi - i\frac{g'}{2} B_\mu \phi \tag{2.13}$$

The final term is the scalar field potential with a quadratic and quartic term assuming a non-zero vaccuum expectation value for ϕ. There is a continuum of ground states giving equivalent physics, one of which must be chosen by nature. Choosing a particular ground state is known as symmetry breaking. Arbitrarily choose:

$$A_\mu = 0 \qquad\qquad B_\mu = 0 \qquad\qquad \phi_0 = \frac{v}{\sqrt{2}} \begin{pmatrix} 0 \\ 1 \end{pmatrix} \tag{2.14}$$

Finding the unbroken generator, Q, such that $Q\phi_0 = 0$ and Q is hermitian gives:

$$Q = \begin{pmatrix} 1 & 0 \\ 0 & 0 \end{pmatrix} \tag{2.15}$$

or

$$Q = T^3 + Y \tag{2.16}$$

The unbroken generator corresponds to the subgroup $U(1)_{em}$ of $SU(2) \times U(1)$. This should correspond to a massless gauge field – the electromagnetic field. $U(1)_{em}$ is not the same as the U(1) component in $SU(2) \times U(1)$ so the electromagnetic potential, A_μ (without superscript) is not B_μ, but a linear combination of the fields A^3_μ and B_μ.

Consider small perturbations around the ground state:

$$\phi = \frac{1}{\sqrt{2}} \begin{pmatrix} 0 \\ v + H(x) \end{pmatrix} \tag{2.17}$$

Thus we get the following expression for $D_\mu \phi$:

$$D_\mu \phi = \begin{pmatrix} -\frac{ig}{2\sqrt{2}} \left(A^1_\mu - iA^2_\mu \right) (v + H(x)) \\ -\frac{i}{2\sqrt{2}} \left(g'B_\mu - gA^3_\mu \right) (v + H(x)) + \frac{1}{\sqrt{2}} \partial_\mu H(x) \end{pmatrix} \tag{2.18}$$

Introduce new fields:

$$W^\pm_\mu = \frac{1}{\sqrt{2}} (A^1_\mu \mp A^2_\mu) \tag{2.19}$$

$$Z_\mu = \frac{1}{\sqrt{g^2 + g'^2}} (gA^3_\mu - g'B_\mu) = \cos\theta_W A^3_\mu - \sin\theta_W B_\mu \tag{2.20}$$

$$A_\mu = \frac{1}{\sqrt{g^2 + g'^2}} (gB_\mu - g'A^3_\mu) = \sin\theta_W A^3_\mu + \cos\theta_W B_\mu \tag{2.21}$$

Z_μ and A_μ are rotations of the original fields with angle θ_W which satisfies Equation 2.22.

$$\cos\theta_W = \frac{g}{\sqrt{g^2 + g'^2}} \qquad \sin\theta_W = \frac{g'}{\sqrt{g^2 + g'^2}} \tag{2.22}$$

Z_μ and A_μ are determined by the necessity that the covariant derivative, $D_\mu \phi$, does not contain A_μ – it must be invariant under the electromagnetic gauge transformation. To quadratic order the Lagrangian can be written as:

$$L = -\frac{1}{2} \mathcal{W}^+_{\mu\nu} \mathcal{W}^-_{\mu\nu} + m^2_W W^+_\mu W^-_\mu \tag{2.23}$$

$$-\frac{1}{4} \mathcal{Z}_{\mu\nu} \mathcal{Z}_{\mu\nu} + \frac{m^2_Z}{2} Z_\mu Z_\mu \tag{2.24}$$

$$-\frac{1}{4} F_{\mu\nu} F_{\mu\nu} \tag{2.25}$$

$$+\frac{1}{2} (\partial_\mu H)^2 - \frac{m^2_H}{2} H^2 \tag{2.26}$$

25

Field	Mass	Particle
$W_\mu^\pm$	$m_W = \frac{gv}{2}$	$W^\pm$
Z_μ	$m_Z = \frac{\sqrt{g^2+g'^2}v}{2}$	Z^0
A_μ	$m_\gamma = 0$	γ
H	$m_H = \sqrt{2\lambda}v$	Higgs

Table 2.2: The physical fields from electroweak symmetry breaking.

where

$$\mathcal{W}_{\mu\nu}^\pm = \partial_\mu W_\nu^\pm - \partial_\nu W_\mu^\pm \tag{2.27}$$

$$\mathcal{Z}_{\mu\nu} = \partial_\mu Z_\nu - \partial_\nu Z_\mu \tag{2.28}$$

The physical fields can be seen from the Lagrangian and are summarised in Table 2.2.

Thus electroweak theory predicts mixing between the electromagnetic and weak forces and the existence of $W^\pm$ and Z^0 bosons with masses in the ratio given by Equation 2.29.

$$\frac{m_W}{m_Z} = \cos\theta_W \tag{2.29}$$

The electric charge is connected to the weak mixing angle by:

$$e = g\sin\theta_W \tag{2.30}$$

The existence of the $W^\pm$ and Z^0 bosons was confirmed experimentally by the UA1 and UA2 experiments in CERN [33]. The W mass measured by UA2 [40] and the Z mass measured by the LEP experiments [34] are:

$$m_W = 80.35 \pm 0.33 \pm 0.17\,\text{GeV} \qquad m_Z = 91.1875 \pm 0.0021\,\text{GeV} \tag{2.31}$$

The weak mixing angle, θ_W, was measured independently [41] to satisfy $\sin^2\theta_W = 0.23$ in good agreement with the predictions of the electroweak theory.

Both leptons and quarks feel the weak interaction. The $W^\pm$ interact only with left-handed fermions. Handedness (or chirality) is the eigenvalue of the γ^5 matrix ($\gamma^5 = i\gamma^0\gamma^1\gamma^2\gamma^3$ where γ^μ are the 4×4 gamma matrices of the Dirac equation shown using the Weyl basis

26

in 2×2 block form in Equation 2.32). Handedness corresponds to the helicity (the projection of the spin onto the direction of motion) in the relativistic limit $E >> m$. The left-handed and right-handed components of a fermion ψ can be projected out using the operators $\frac{1}{2}(1 - \gamma^5)$ and $\frac{1}{2}(1 + \gamma^5)$ respectively.

$$\gamma^0 = \begin{pmatrix} 0 & I_2 \\ I_2 & 0 \end{pmatrix} \qquad \gamma^k = \begin{pmatrix} 0 & \sigma^k \\ -\sigma^k & 0 \end{pmatrix} \tag{2.32}$$

The left handed components form SU(2) doublets while the right handed components are singlets under SU(2) as in Equation 2.33 for leptons and Equation 2.34 for quarks.

$$E_L = \begin{pmatrix} e \\ \nu_e \end{pmatrix}_L \qquad e_R \tag{2.33}$$

$$Q_L = \begin{pmatrix} u \\ d \end{pmatrix}_L \qquad u_R \qquad d_R \tag{2.34}$$

The quark couplings are:

$$L_{quark} = \sum_{p=1}^{3} \left(\left(\bar{Q}_p \right)_L i\gamma^\mu D_L^\mu \left(Q_p \right)_L + \left(\bar{u}_p \right)_R i\gamma^\mu D_R^\mu \left(u_p \right)_R + \left(\bar{d}_p \right)_R i\gamma^\mu D_R^\mu \left(d_p \right)_R \right) \tag{2.35}$$

where p is an index over the three generations.

The three generation are not separate but interact with each other through flavour changing charged currents. These interactions are described by the CKM (Cabbibo, Kobayashi, Maskawa) matrix. Equation 2.36 shows the current best experimentally determined values for the magnitude of the elements in the CKM matrix. For example, the top decays almost exclusively to the b quark ($t \rightarrow bW^+$) as in Figure 2.2 since $|V_{tb}| \approx 1$.

$$\begin{pmatrix} |V_{ud}| & |V_{us}| & |V_{ub}| \\ |V_{cd}| & |V_{cs}| & |V_{cb}| \\ |V_{td}| & |V_{ts}| & |V_{tb}| \end{pmatrix} = \begin{pmatrix} 0.97428 \pm 0.00015 & 0.2253 \pm 0.0007 & 0.00347^{+0.00016}_{-0.00012} \\ 0.2252 \pm 0.0007 & 0.97345^{+0.00015}_{-0.00016} & 0.0410^{+0.0011}_{-0.0007} \\ 0.00862^{+0.00026}_{-0.00020} & 0.0403^{+0.0011}_{-0.0007} & 0.999152^{+0.000030-0.000045} \end{pmatrix} \tag{2.36}$$
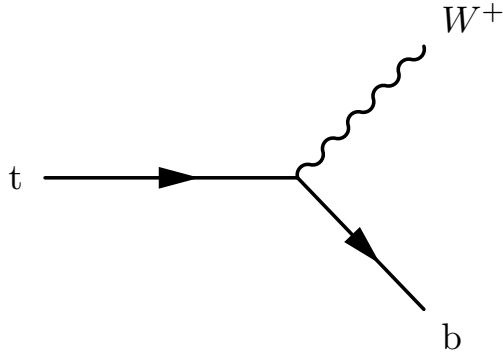
Figure 2.2: An illustration of top decay via flavour changing charged current.
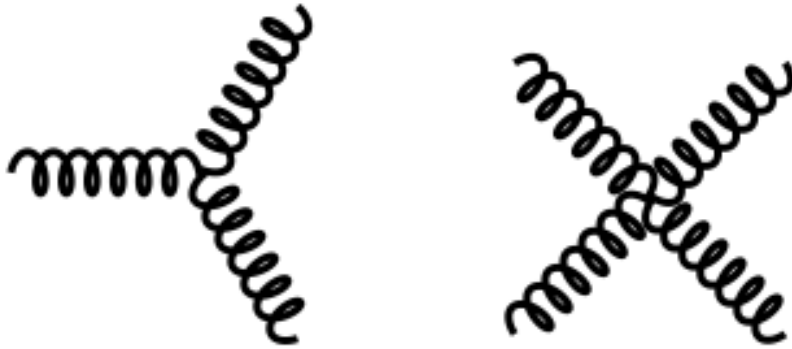
Figure 2.3: Gluon self-interactions occur because gluons carry colour charge. This is due to the non-abelian nature of SU(3).

2.3.3 Quantum Chromodynamics (QCD)

SU(3) is the symmetry group of the strong force which is composed of special unitary 3×3 matrices. Particles which interact via the strong force carry colour charge. Quarks come in 3 colours denoted r, g and b. There are 8 gluons which correspond to the 8 generators of SU(3). Gluons carry colour charge and so interact with each other because SU(3) is a non-abelian group, which means that the group elements do not commute.

Since the data used in this thesis come from a proton collider, the structure of the proton needs to be considered when making predictions. Particularly cross-section predictions rely on knowledge of the Parton Density Functions (PDFs) within the proton.

The Hadron Electron Ring Accelerator (HERA) made electron proton collisions to determine the structure of the proton. Deep inelastic scattering in the H1 [42] and ZEUS [43] detectors revealed that the structure functions of the proton are independent of the momentum transfer, Q, and dependent only on $x = \frac{Q^2}{2p.q}$, where p is the momentum of the incoming electron and q is the momentum of the exchanged virtual photon [44]. This is called Bjorken scaling and led to the parton model in which the proton is made of partons which carry a fraction, x, of the proton momentum. Figure 2.4 shows the independence of the cross-section with Q^2 over 5 orders of magnitude.

The PDFs are the probability distribution for the fraction of the proton momentum carried by each parton. The PDFs need to be known to make reliable Monte Carlo simulations and cross-section predictions for the LHC. Figure 2.5 shows the parton density functions measured by H1 and ZEUS.

The coupling strength of the strong force varies with energy. The strong force is strong at low energies where quarks exist only in colourless bound states. This is known as confinement. At high energies the strong force becomes weaker as the partons behave as free particles. This is known as asymptotic freedom. Figure 2.6 shows the variation in coupling strength of the strong, weak and electromagnetic force as a function of energy.

2.4 Motivation for new physics at the TeV scale

The motivations for expecting the discovery of new physics at the TeV scale are considered.

WW scattering

WW scattering (among other similar processes) has been observed at the Large Electron Positron (LEP) collider and the cross-section has been measured. Without additional couplings the interaction violates unitarity. The Higgs boson is one mechansim to mediate this interaction, but so far the Higgs has not been observed. Whatever the mechanism by which this interaction occurs it must be at the TeV energy scale to avoid violating unitarity [19].
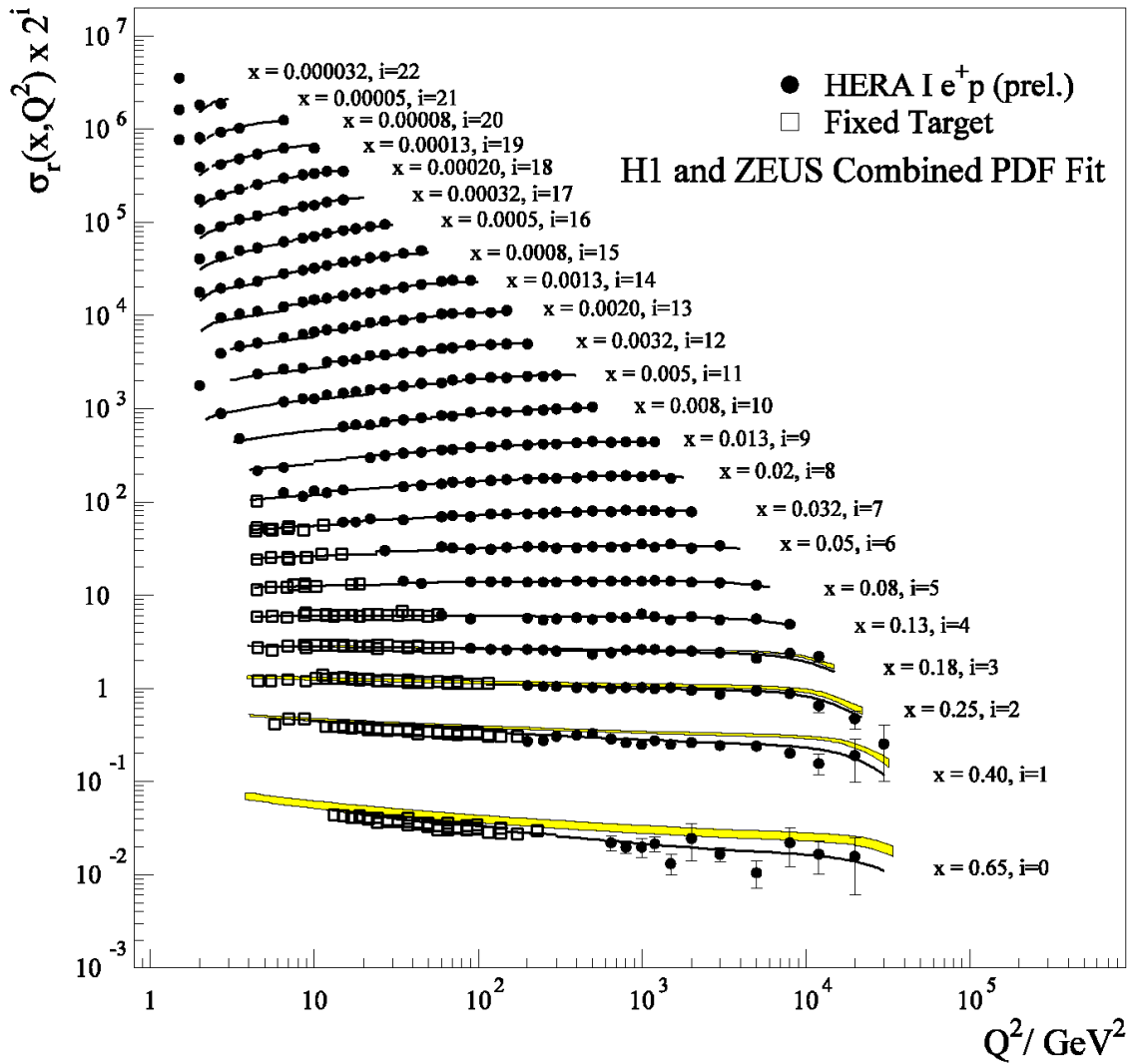
Figure 2.4: The structure functions of the proton are independent of Q^2 over 5 orders of magnitude. Reproduced from [2].
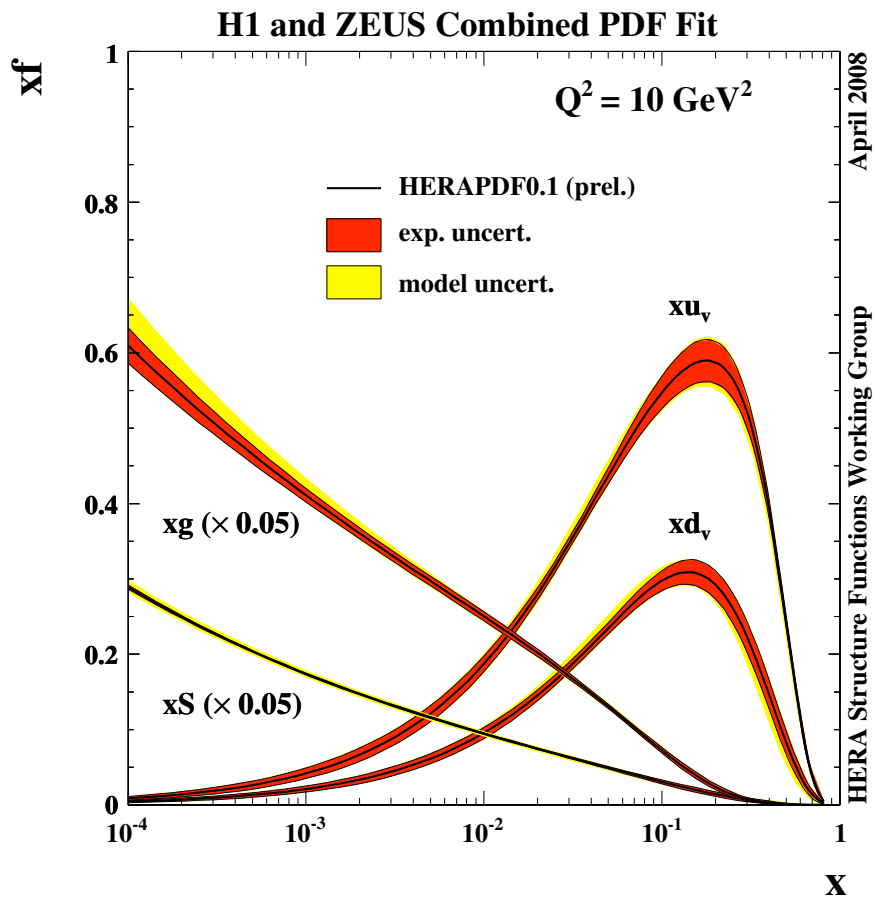
Figure 2.5: The Parton Density Functions (PDFs) measured by H1 and ZEUS. Reproduced from [2].
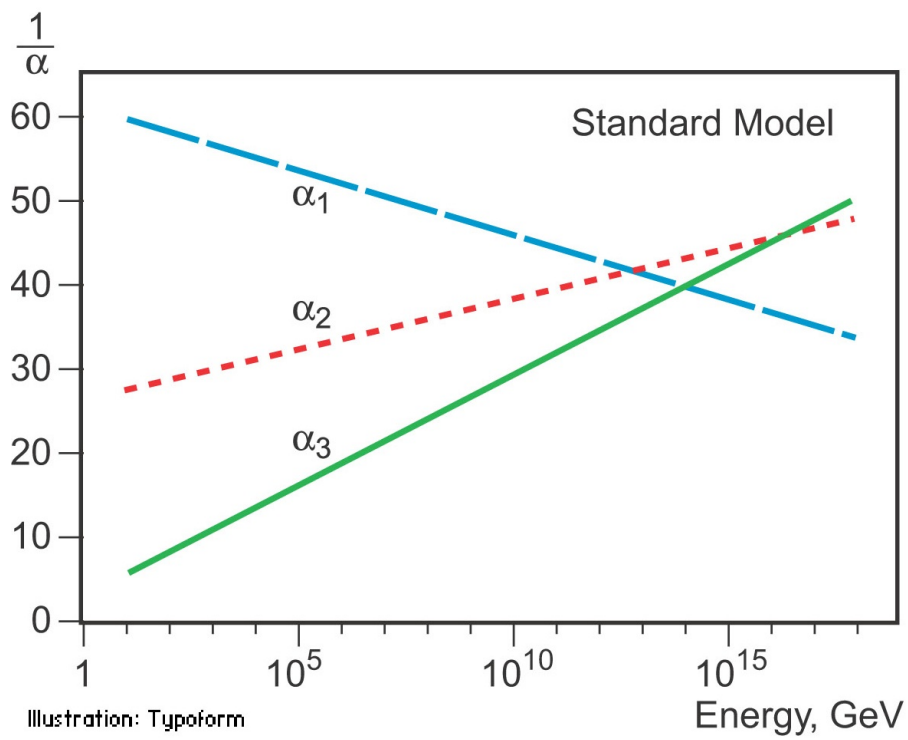
Figure 2.6: The coupling strengths of the electromagnetic force (α_1), the weak force (α_2) and the strong force (α_3) as a function of energy. Reproduced from [3].
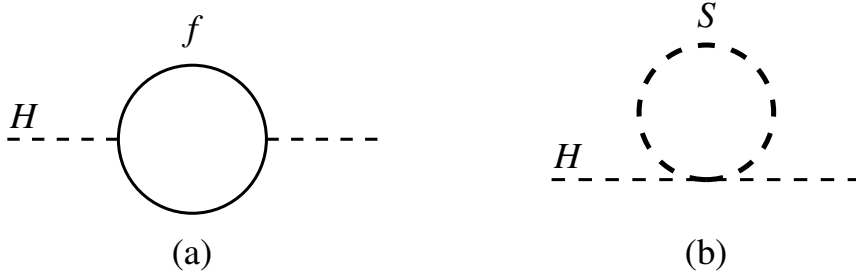
Figure 2.7: Loop corrections to the Higgs mass squared m_H^2 from (a) a fermion f with mass m_f and (b) a scalar S with mass m_S.

New energy scale

This is simply the observation that while exploring a higher energy scale than has previously been explored one can expect to find new things. In the same way as when explorers explore a new land they can expect to see things they have not seen before.

Hierarchy Problem

The hierarchy problem is fundamentally a problem of scale [17]. There are two fundamental energy scales in physics: the Electroweak scale ($\sim 100\,\text{GeV}$) and the Planck scale ($\sim 10^{18}\,\text{GeV}$), where gravity becomes as strong as the gauge interactions. Certainly at the Planck scale the SM will no longer hold because a quantum treatment of gravity is needed. The Electroweak scale is well measured at colliders and the results form our current understanding of particle physics. New physics can affect the mass of the Higgs boson through loop corrections.

The one-loop quantum correction to the Higgs mass squared in Figure 2.7(a) with a fermion coupling $-\lambda_f \phi \bar{f} f$ and a cut-off energy Λ is given by Equation 2.37.

$$\Delta m_H^2 = -\frac{|\lambda_f|^2}{8\pi^2}\Lambda^2 + ... \tag{2.37}$$

For a scalar coupling $-\lambda_S|\phi|^2|S|^2$ and a cut-off Λ the one-loop quantum correction to m_H^2 from Figure 2.7(b) is given by Equation 2.38.

$$\Delta m_H^2 = \frac{\lambda_S}{16\pi^2}\Lambda^2 + ...\tag{2.38}$$

The one-loop quantum corrections to m_H^2 are quadratically divergent depending on the cut-off used to do the calculation. In supersymmetry this problem is solved by introducing a symmetry between fermions and bosons. For every SM particle there is a supersymmetric partner which is a boson for fermions and a fermion for bosons. The fermions give a -1 contribution to m_H^2 while the bosons give a +1 contribution cancelling each other.

Dark Matter candidates

Only 5% of the mass/energy in the universe is normal matter that we observe. The remainder is made up of dark matter (25%) and Dark Energy (70%) [45]. Dark energy is an unknown that is introduced to explain the expansion of the universe. Dark matter is well known.

The existence of dark matter is inferred from its gravitational interaction with normal matter. Dark matter was postulated as unobserved mass to account for the orbital velocities of galaxies in clusters [46]. There have since been other observations that have confirmed the existence of dark matter including the rotational speed of galaxies [47] and the bullet cluster [48].

The bullet cluster provides the best evidence yet on the nature of dark matter. It consists of two colliding clusters of galaxies. The visible matter (stars) pass straight through slowed only by gravitation. The hot gas that represents most of the normal matter is detected through X-rays. The hot gas slows more than the stars due to its electromagnetic interactions. Another piece of information comes from gravitational lensing. In the absence of dark matter the gravitational lensing is expected to follow the normal matter (i.e. the X-ray gas). However, the gravitational lensing is strongest in the separated regions around the visible matter. This provides support to the idea that most of the mass of the galaxies is made up of collisionless dark matter.

If dark matter interacts through the weak force, then it could be observed at the LHC. Dark

matter may not interact weakly. Perhaps it interacts only gravitationally. Additionally it may not show up at the TeV scale. However, SUSY (which is one of the popular theories of physics beyond the SM) predicts a set of supersymmetric particles the lightest of which could be a dark matter candidate. Direct searches from CDMS [49] put an upper limit of $\sim 1\,\mathrm{pb}$ on the cross-section of weakly interacting massive particles over the energy range $10\,\mathrm{GeV}$ to $1\,\mathrm{TeV}$.

2.5 Supersymmetry

Supersymmetry (SUSY) proposes that for every particle there is a supersymmetric partner which is a boson for fermions and a fermion for bosons [16]. If unbroken, such a symmetry ensures cancellation of the divergence in the Higgs boson mass. The operator Q which generates the supersymmetric transformations can be written as Equation 2.39. Since the particles within the supermultiplets must maintain the gauge symmetries of the SM, Q must commute with the internal symmetries of the SM.

$$Q|\mathrm{Boson}> = |\mathrm{Fermion}> \quad Q|\mathrm{Fermion}> = |\mathrm{Boson}> \tag{2.39}$$

Each lepton SU(2) doublet $(\nu_l,\, l)_L$ has two superpartners, both spin-0: a sneutrino $\tilde{\nu}_{lL}$ and a slepton $\tilde{l}_L$. Each singlet l_R has a spin-0 superpartner l_R.

In an analagous way, each quark doublet $(q,\, q')_L$ has squark partners $\tilde{q}_L$, $\tilde{q}'_L$ and each singlet q_R has a partner $\tilde{q}_R$.

The two spin-1/2 higgsino doublets $(\tilde{H}_u^+,\, \tilde{H}_u^0)$, $(\tilde{H}_d^0,\, \tilde{H}_d^-)$, have as partners two spin-0 Higgs doublets $(H_u^+,\, H_u^0)$ and $(H_d^0,\, H_d^-)$.

The spin-1 gauge bosons (before electroweak symmetry breaking) g, $W^\pm$, W^0, B^0 have spin-1/2 partners the gluino, wino and bino $(\tilde{g},\, \tilde{W}^\pm,\, \tilde{W}^0,\, B^0)$.

After electroweak symmetry breaking, three of the eight degrees of freedom of the two complex Higgs doublets become longitudinal modes of the Z^0 and $W^\pm$ bosons. Five Higgs scalars remain: h^0, H^0, A^0, $H^\pm$. The parameter $\tan\beta$ is the ratio of the vacuum expectation values of the neutral Higgs fields.

A straightforward implementation of supersymmetry would predict a whole new set of particles with the same mass and same interactions as the SM particles. Since we do not observe these particles SUSY, if it exists, must be broken. The superpartners can then be at a higher mass scale. There are various different schemes for SUSY breaking [50]. Here only Gauge Mediated SUSY Breaking (GMSB) is considered [51].

Another symmetry R-parity (R_P) is often introduced to SUSY models. R_P is defined in Equation 2.40 where B is the baryon number, L is the lepton number and S is the spin. R_P is +1 for SM particles and -1 for supersymmetric partners.

$$R_P = (-1)^{3(B-L)+2S} \qquad (2.40)$$

If R-parity is conserved, there are two important consequences:

- At colliders supersymmetric partners can only be produced in pairs.

- The lightest supersymmetric particle (LSP) is stable.

The first point ensures that a supersymmetric particle always decays into another supersymmetric particle and that there are always two decay chains of supersymmetric particles in each supersymmetric event. The second point means that SUSY events contain missing energy since the LSP is not detected. The LSP also provides a possible dark matter candidate.

2.6   Gauge Mediated SUSY Breaking (GMSB)

Under GMSB the messenger particles between the visible sector (SM and SUSY particles) and the hidden sector (responsible for the SUSY breaking) are gauge particles. In the Minimal Supersymmetric Standard Model (MSSM) there are 6 parameters describing GMSB:

- Λ – the SUSY beaking scale.

- M_m – the mass scale of the messengers.

- N_5 – the number of messengers.

- $\tan\beta$ – the ratio of the higgs vacuum expectation values.

- $\text{sign}(\mu)$ – the sign of the higgsino mass term.

- C_{grav} – the scale factor of the gravitino coupling.

SUSY events contain real missing transverse energy ($\not{E}_T$) from the Lightest Supersymmetric Particle (LSP). The LSP is the gravitino ($\tilde{G}$) and the Next Lightest Supersymmetric Particle (NLSP) is the lightest neutralino ($\tilde{\chi}_1^0$). The neutralino decays into a photon and a gravitino $\tilde{\chi}_1^0 \to \gamma\tilde{G}$. The events contain two photons coming from separate decay chains.

At lower centre-of-mass energies, for example at LEP (200 GeV) and at the Tevatron (1.96 TeV), the dominant production mechanism is electroweak production through a W or a Z since GMSB involves the production of high mass particles (e.g. squark and gluino) which cannot be produced at low centre of mass energy. The signature for electroweak production GMSB is $\gamma\gamma + \not{E}_T$. ALEPH [52] at LEP (e^+e^- collider) and D0 [53] and CDF [54] at the Tevatron ($p\bar{p}$ collider) have published limits on electroweak production GMSB.

At the LHC energy (7 TeV) the cross section is higher and strong production is dominant since it is possible to produce high mass squarks and gluinos. Figure 2.8 shows an example of a strong production SUSY decay chain. Strong production events must contain at least two jets from the two squarks/gluions. Squarks decay to a quark and the next particle in the SUSY mass hierarchy ($\tilde{q} \to q\tilde{X}$) resulting in one jet. Gluinos decay to a quark anti-quark pair and the next particle in the SUSY mass hierarchy ($\tilde{g} \to q\bar{q}\tilde{X}$) resulting in two jets. The only previous limits on strong production GMSB come from ATLAS [55] and CMS [12] at the LHC.
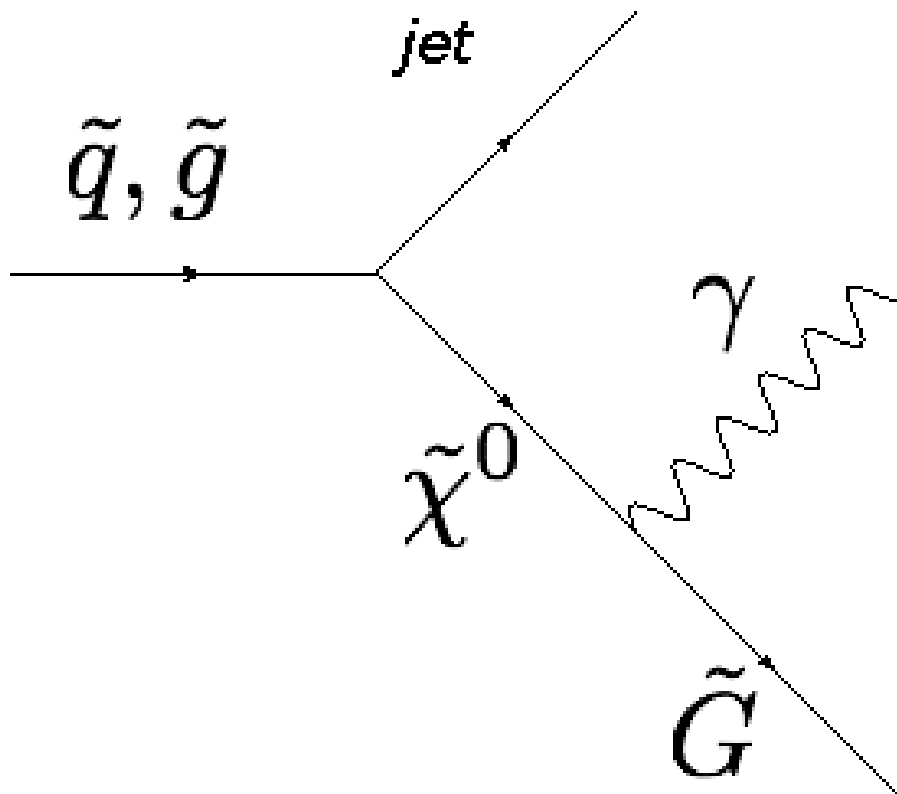
Figure 2.8: An example of a strong production SUSY decay chain.

Chapter 3

CMS Detector and Reconstruction

3.1 Introduction

The LHC is a $27\,\text{km}$ circular particle accelerator which lies across the French-Swiss border about $100\,\text{m}$ underground. It was designed to accelerate and collide beams of protons or heavy ions. The design centre of mass energy ($\sqrt{s}$) for proton-proton collisions is $14\,\text{TeV}$. The design luminosity is $10^{34}\,\text{cm}^{-2}\text{s}^{-1}$. The LHC is the highest energy particle accelerator ever built.

Figure 3.1 shows a diagram of the LHC accelerator complex. Protons are extracted from a cylinder of hydrogen gas and accelerated first by a linear accelerator which injects them into the Proton Synchrotron (PS), which accelerates them to $25\,\text{GeV}$ and feeds the Super Proton Synchrotron (SPS). The SPS accelerates the beams to $450\,\text{GeV}$ and subsequently injects them into the LHC.

The CMS detector is one of two general purpose LHC experiments. It was designed to explore O(TeV) energy proton-proton collisions for indications of physics beyond the Standard Model. The CMS detector is $21.6\,\text{m}$ long and $14.6\,\text{m}$ in diameter and has a total weight of 13 500 tonnes. It is located at Point 5 on the LHC ring near Cessy in France. Figure 3.2 shows the layout of the CMS detector.

In the following sections each component of the CMS detector is described starting from the innermost (closest to the interaction point) and going to the outermost. The CMS
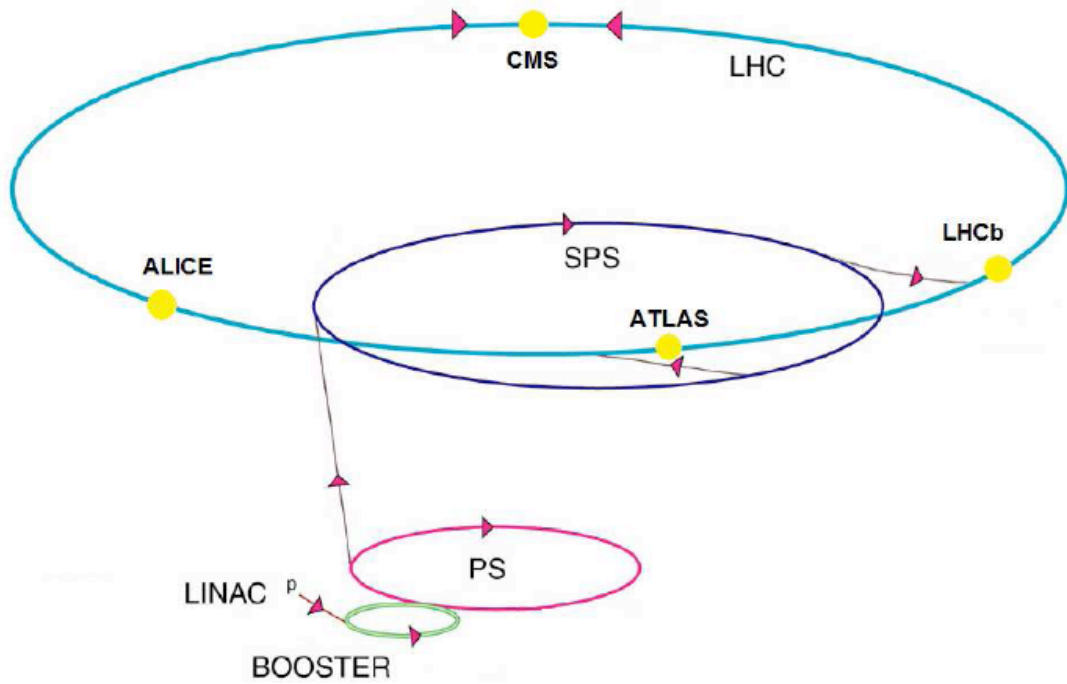
Figure 3.1: A diagram of the LHC accelerator complex. Reproduced from [4].

trigger and the computing model are also described.

3.2 Pixel Detector

The pixel detector consists of 3 barrel layers with 2 endcap disks on each side (Figure 3.3). The barrel layers are at mean radii of 4.4 cm, 7.3 cm and 10.2 cm and have a length of 53 cm. The endcap disks are placed either side at $|z| = 34.5$ cm and 46.5 cm.

The purpose of the pixel detector is to give good primary vertex resolution and to initiate track reconstruction. The pixel size is $100 \times 150\,\mu$m. The spatial resolution is about $10\,\mu$m for the (r, ϕ) measurement and about $20\,\mu$m for the z measurement.

The primary vertex is found by clustering selected tracks in z. A fit is performed based on a weight assigned to each track which is between 0 and 1 depending on the compatibility with the vertex [5].
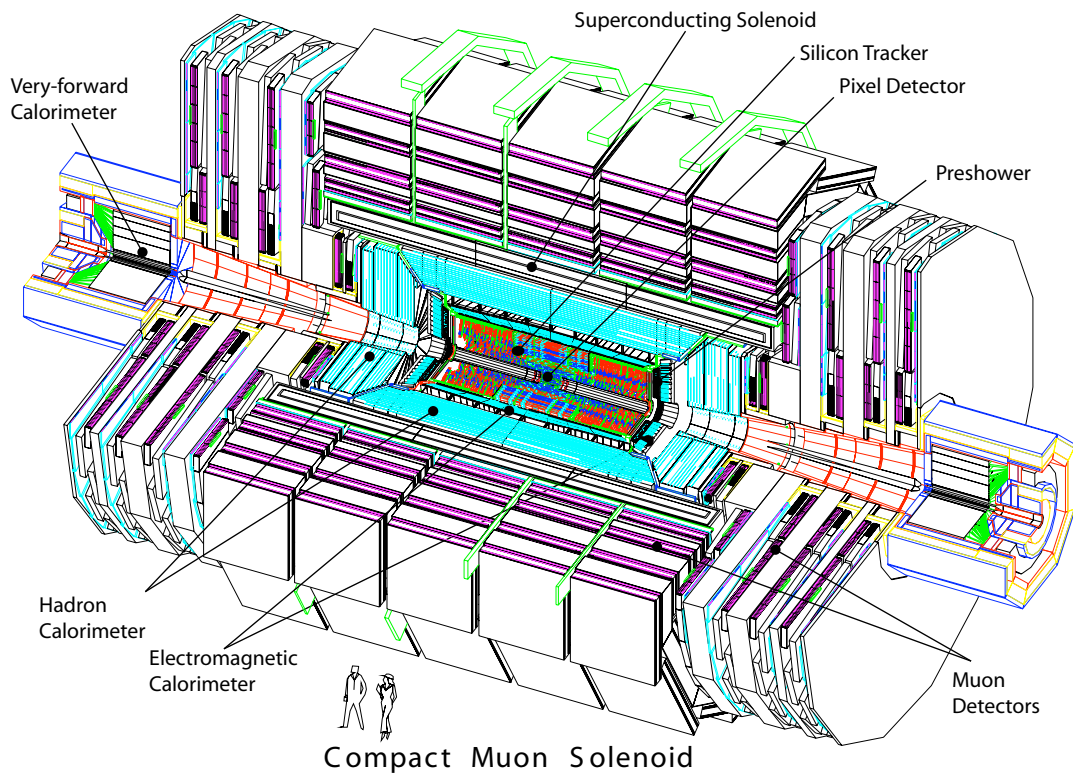
Figure 3.2: A view of the layers inside the CMS detector. Reproduced from [4].
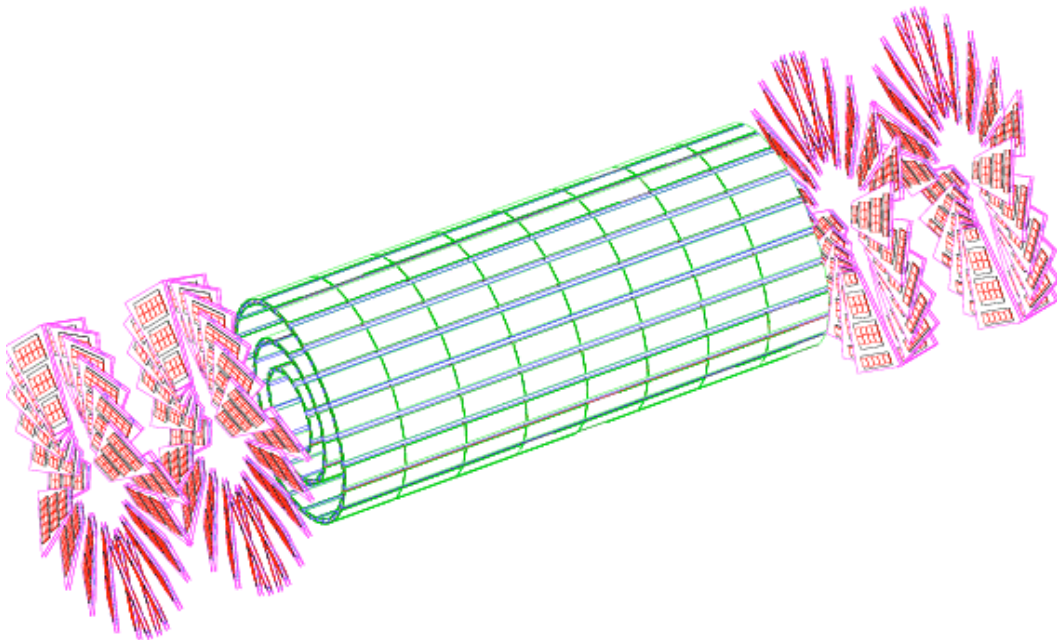
Figure 3.3: A diagram of the pixel detector. Reproduced from [4].
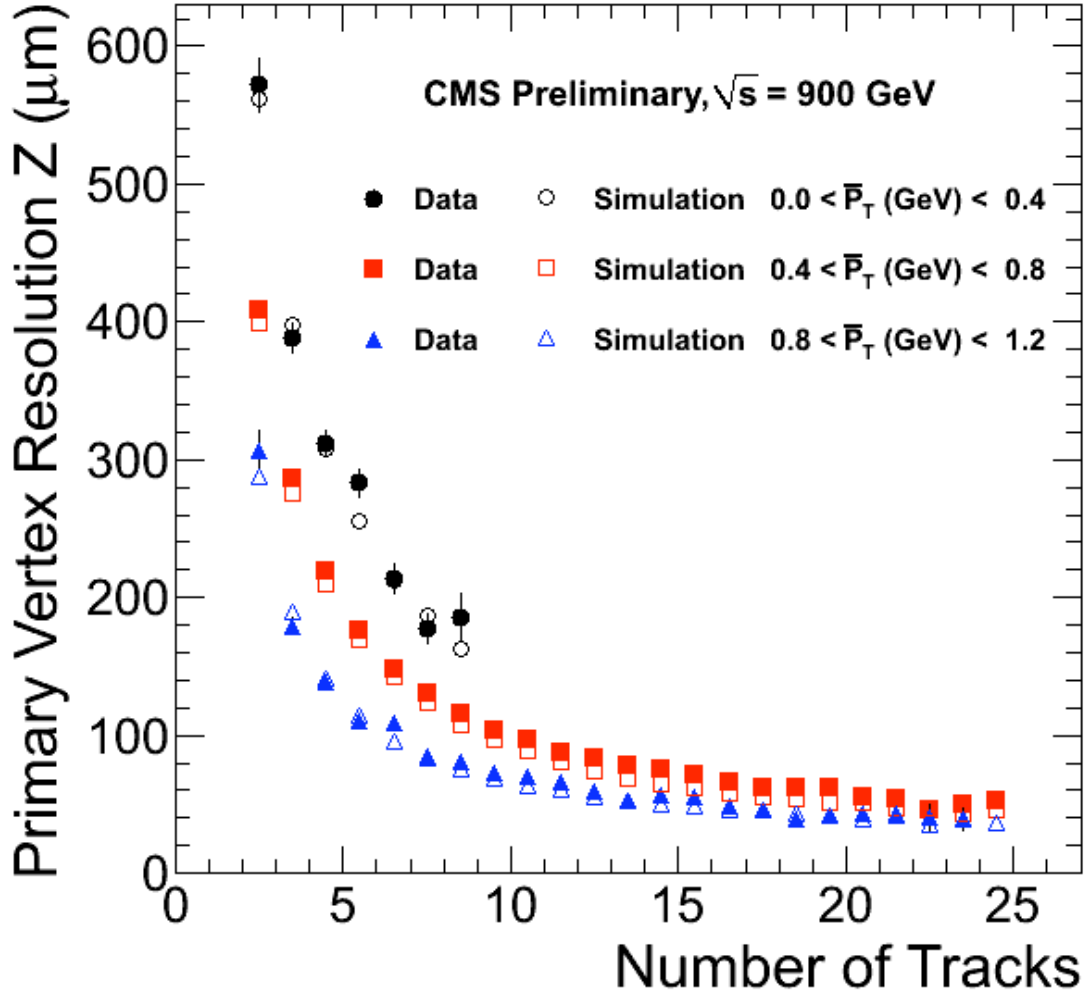
Figure 3.4: The primary vertex resolution as a function of the number of tracks for various average track p_T ranges. Reproduced from [5].

The primary vertex resolution depends strongly on the number of tracks in the fit. Figure 3.4 shows the primary vertex resolution as a function of the number of tracks for various average track p_T ranges.

3.3 Silicon Strip Tracker

The silicon strip tracker is designed to measure the trajectory of charged particles. It is made from strips of silicon which charged particles ionise. The technology is the pn junction with a reverse bias voltage applied that creates a depletion region. Charged particles ionise the silicon in the depleted region creating electron hole pairs which travel to the
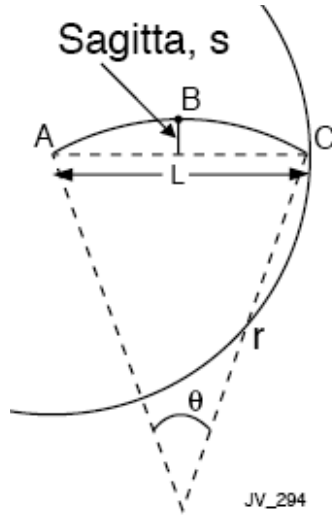
Figure 3.5: Diagram illustrating how the transverse momentum is calculated from the curvature of the track in the magnetic field.

electrodes giving rise to a signal.

The transverse momentum of a particle is measured from the curvature of the track in the magnetic field by Equation 3.1, where p_T is the transverse momentum in GeV, B is the magnetic field in Tesla and r is the radius of curvature in metres. Only the hits are measured directly. The length of the "sagitta", shown in Figure 3.5, is deduced and the transverse momentum is calculated from this. Since s is inversely proportional to p_T, the resolution is worse at higher p_T.

$$p_T = 0.3Br \tag{3.1}$$

The silicon strip tracker is sub-divided into four structural units. Figure 3.6 shows the layout of the tracker. The resolution of the tracker is shown for muons of $p_T = 1$, 10 and 100 GeV in Figure 3.7.

3.4 Electromagnetic Calorimeter

The Electromagnetic Calorimeter (ECAL) measures the energy of electromagnetic showers.
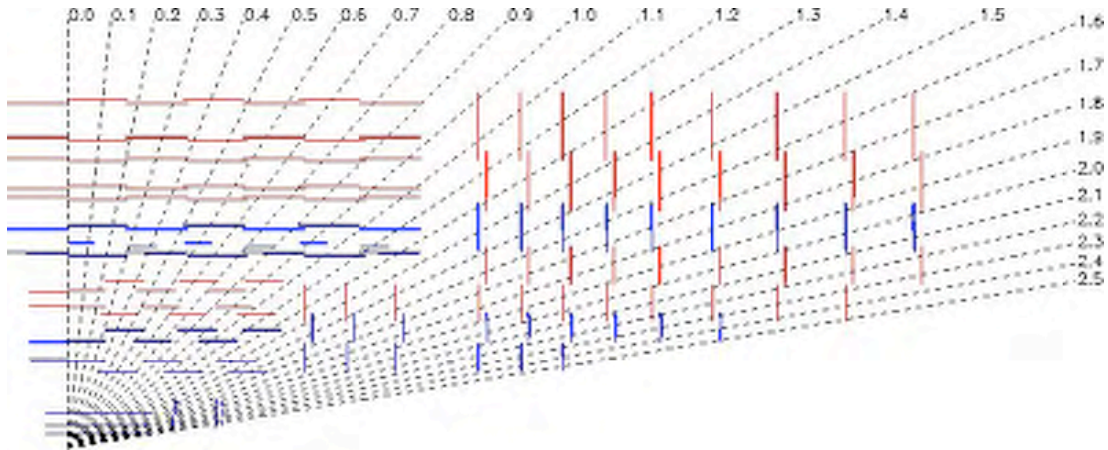
Figure 3.6: The layout of the silicon strip tracker. Reproduced from [4].

The ECAL has 3 components: the ECAL barrel (EB), the ECAL endcap (EE) and the ECAL pre-shower (ES). The EB covers the range $|\eta| < 1.479$. The EB radius is 1.29m and the total length in the z-direction is 6m. The EE consists of two identical detectors on either side of the EB covering the region $1.479 < |\eta| < 3$. The ES is positioned in front of the EE to improve the γ/π^0 discrimination which is important for $H \to \gamma\gamma$ searches. Figure 3.8 shows a diagram of the layout of the ECAL.

An electromagnetic shower progresses through two processes bremsstrahlung, where an electron or positron emits a photon, and pair production, where a photon converts to an electron and a positron. Figure 3.9 shows how an electromagnetic shower progresses. The shower continues until the electrons/photons reach a critical energy, E_c, where energy loss dominates over the production of new shower particles.

Sampling calorimeters have layers of heavy material to initiate the shower and active detector to sample the shower. In homogeneous calorimeters the heavy material and the active detector are one and the same. Materials used for electromagnetic calorimeters have two characteristic lengths which describe the shape of EM showers. Radiation length is the length over which an electron's energy is reduced to 1/e of its initial energy. Moliere radius describes the lateral size of the shower; it is the radius which contains 90% of the energy of the shower.
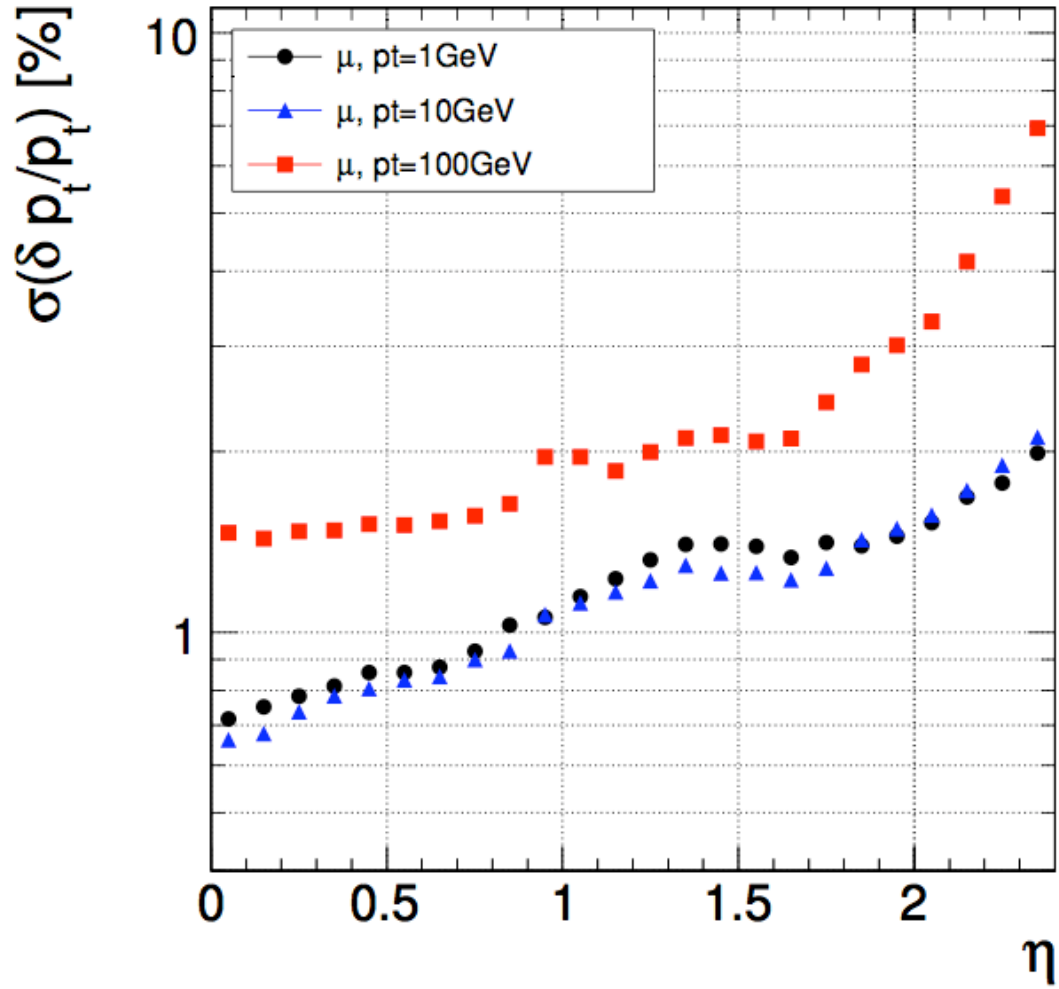
Figure 3.7: The resolution of the tracker as a function of η for muons of $p_T = 1$, 10 and 100 GeV.
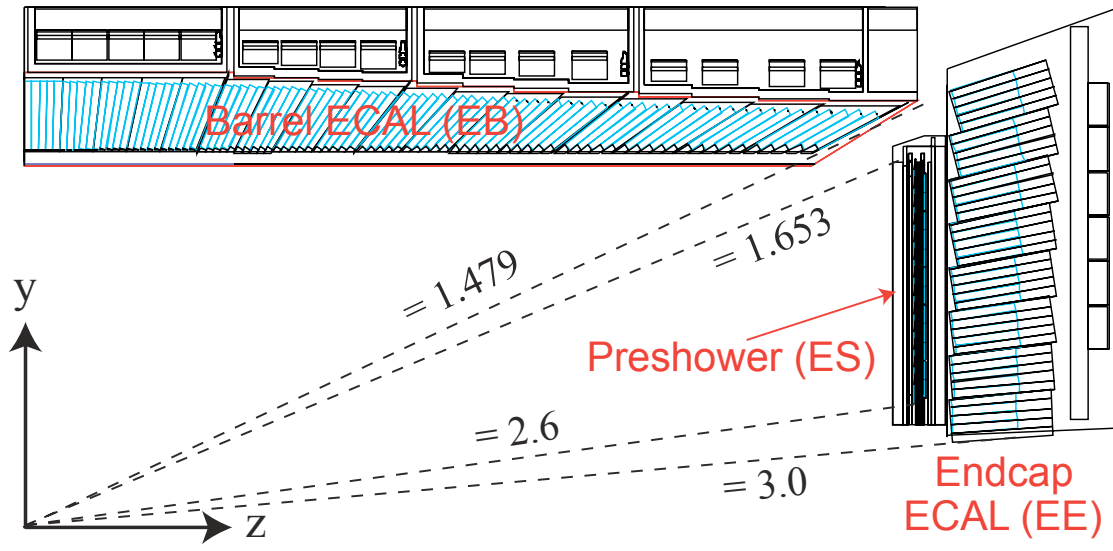
Figure 3.8: A diagram of the layout of the ECAL.
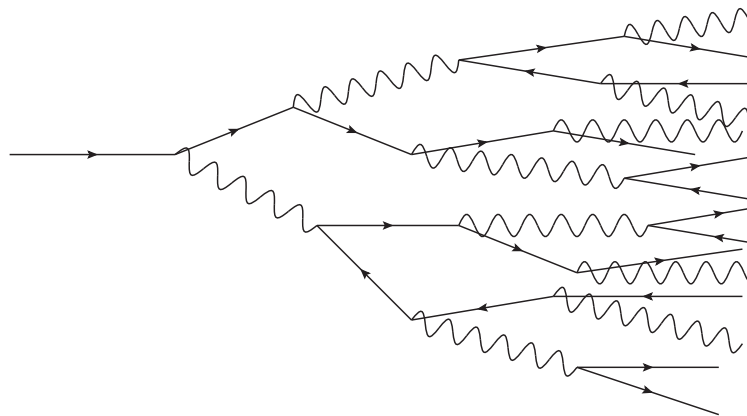
Figure 3.9: An illustration of the development of an EM shower.

The EB and EE are homogeneous calorimeters made of lead tungstate ($PbWO_4$) crystals. This material was chosen because of its short radiation length ($X_0 = 0.89$ cm) and short Moliere radius ($r_m = 2.2$ cm). The crystals have a low light yield, but can withstand high levels of radiation. The scintillation light is blue/green with a maximum at $420 - 430$ nm. The light is detected by Avalanche Photodiodes (APDs) in the EB and Vacuum Phototriodes (VPTs) in the EE. The choice of photodetectors was based on the requirement of adequate electronic gain given the low light yield of the crystals, operation in the magnetic field and the ability to tolerate the high radiation environment particularly in the end-cap regions.

In the EB the length of the crystals is 23 cm (26 X_0) and the cross-section is 0.0174×0.0174 in η-ϕ or about 22 mm $\times$ 22 mm at the front face. Figure 3.8 shows the layout of crystals in the EB. The crystals are angled at 3° with respect to the interaction point to minimise the risk of particles escaping down the cracks between the crystals. The crystals are tapered with the front face smaller than the rear face. This has the advantage of tighter packing with fewer gaps and it focusses the scintillation light. Because the crystal is wider at the back than the front total internal reflection leads light rays to have a smaller with respect to the long axis of the crystal with each reflection. The ECAL is divided into regions called trigger towers (TTs) for which trigger primitives (crystal energy sums) used by the trigger are calculated. There are 85×72 TTs in the EB each consisting of 5x5 arrays of crystals.

In the EE the length of the crystals is 22 cm ($25X_0$). Due to the geometry of the detector the granularity in η-ϕ varies across the EE.

The ES is a sampling device with two layers of active silicon sensors placed in front of the end-caps. Its purpose is to distinguish between isolated photons and π^0s which are a major background to the $H \rightarrow \gamma\gamma$ search. It is made of lead and silicon strip sensors and has a depth of 20 cm ($3X_0$).

The energy resolution, σ, has been parameterised as a function of energy in Equation 3.2.

$$\left(\frac{\sigma}{E}\right)^2 = \left(\frac{S}{\sqrt{E}}\right)^2 + \left(\frac{N}{E}\right)^2 + C \qquad (3.2)$$

The parameters S, N and C represent the stochastic term, the noise term and the constant term respectively.

The stochastic term, S, is related to the uncertainty in the number of photons detected. The number of photons for a given energy electromagnetic shower follows a Poisson distribution. So if n photons are detected, the uncertainty is $\sqrt{n}$. And the energy is proportional to the number of photons, hence the $\sqrt{E}$ dependence of this term. About 1000 shower particles are generated per GeV of the electron or photon.

The noise term, N, comes from electronics noise in the photodetectors and pile-up. It is independent of energy. The noise from the VPTs in the end-cap is significantly higher than for the APDs in the barrel. The noise is about $100\,\mathrm{MeV}$ as measured using the test beam.

The constant term, C, contains those uncertainties which are proportional to energy. The dominant contributors are inter-calibration uncertainties and non-uniformity of the light collection.

Figure 3.10 shows the energy resolution of the ECAL as a function of beam energy measured using the test beam which consisted of electrons with energy $10 - 100\,\mathrm{GeV}$ [6].

3.5   Hadronic Calorimeter

The Hadronic Calorimeter (HCAL) measures the energy of hadronic showers and assists in the triggering and measurement of jets and missing transverse energy.

The HCAL is a sampling calorimeter with brass absorbers and plastic scintillator tiles in the central and endcap regions and steel absorbers with quartz fibre scintillators in the forward region. Brass has a short interaction length ($12\,\mathrm{cm}$) providing adequate containment within the limited space inside the magnet. Steel is used in the forward region. The scintillation light is detected by multi-channel hybrid photodiodes (HPDs) in the central

S = 3.37±0.10 %

C = 0.25±0.02 %

N = 108 MeV
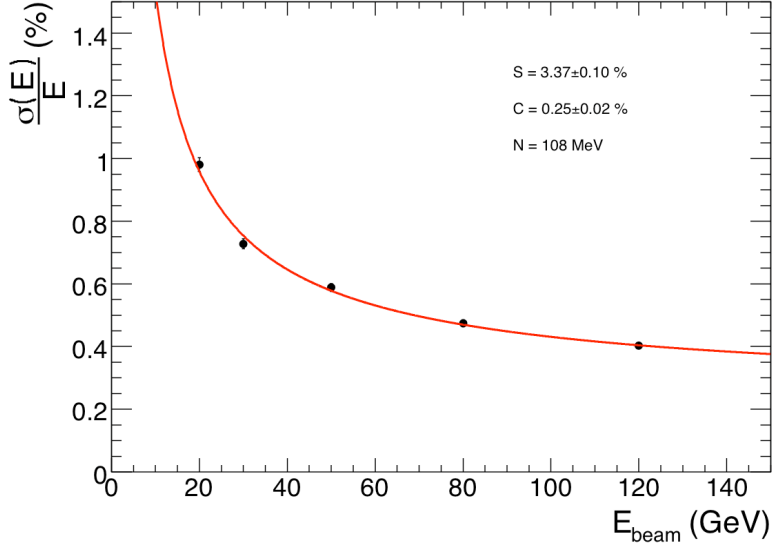
Figure 3.10: The energy resolution of the ECAL as a function of the beam energy as measured using the test beam. The parameterisation of the resolution has been fitted and values extracted for the parameters. Reproduced from [6].

region and photomultiplier tubes (PMTs) in the forward region.

The HCAL covers the range $|\eta| < 5$ and consists of four subdetectors: the Hadron Barrel (HB), the Hadron Outer (HO), the Hadron Endcap (HE) and the Hadron Forward (HF). The HB covers the region $|\eta| < 1.4$ and contains towers with a granularity of $\Delta\eta \times \Delta\phi = 0.087 \times 0.087$. The HB is constrained radially to be between the ECAL outer surface (at r = 1.77m) and the inner surface of the solenoid (at r = 2.95m). This constrains the amount of material that can be put in to absorb the hadronic showers. For this reason the HO lies outside the HB and the magnet in the region $|\eta| < 1.26$ and contains extra scintillators to catch energy leakage from high energy jets. The HE covers the range $1.3 < |\eta| < 3.0$ with a granularity that varies with η from $\Delta\eta \times \Delta\phi = 0.087 \times 0.087$ at $\eta = 1.3$ to $\Delta\eta \times \Delta\phi = 0.350 \times 0.174$ at $\eta = 3.0$. The region $3 < |\eta| < 5$ is covered by the HF.

Figure 3.11 shows a diagram of the development of a hadronic shower.

The jet energy resolution and the missing transverse energy resolution are the key indicators of the performance of the HCAL. Figure 3.12 shows the jet transverse energy
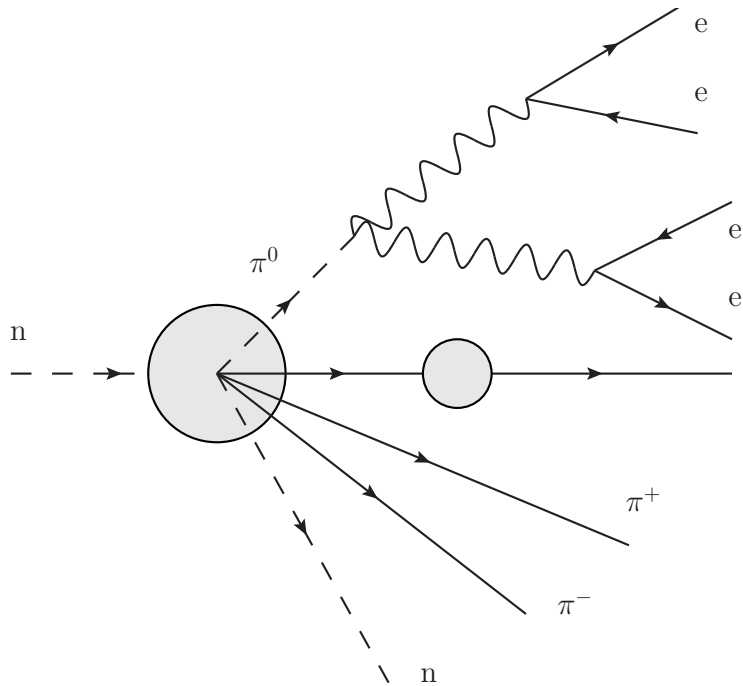
Figure 3.11: An illustration of the development of a hadronic shower.

resolution and the missing transverse energy resolution [7, 8]. The jet resolution for jets with $p_T > 40\,\text{GeV}$ is better than $10\,\%$ and the $\not{E}_T$ resolution is between $5\,\%$ and $10\,\%$.

3.6 Superconducting Solenoid Magnet

The superconducting solenoid generates a uniform 3.8T magnetic field in the tracking volume. The magnetic field is important for determining the charge of particles and for the momentum measurement of charged particles, particularly low momentum charged particles and muons. The solenoid is 12.5m in length and 6m in diameter. The flux is returned through an iron yoke to provide a magnetic field which bends muons in the opposite direction. The iron is in layers between the muon chambers.

The precision of the momentum measurements in the inner tracker relies on a homogeneous magnetic field. Within the tracker the magnetic field is homogeneous to within 5% [56] and has been mapped with a precision better than 0.1% [57].
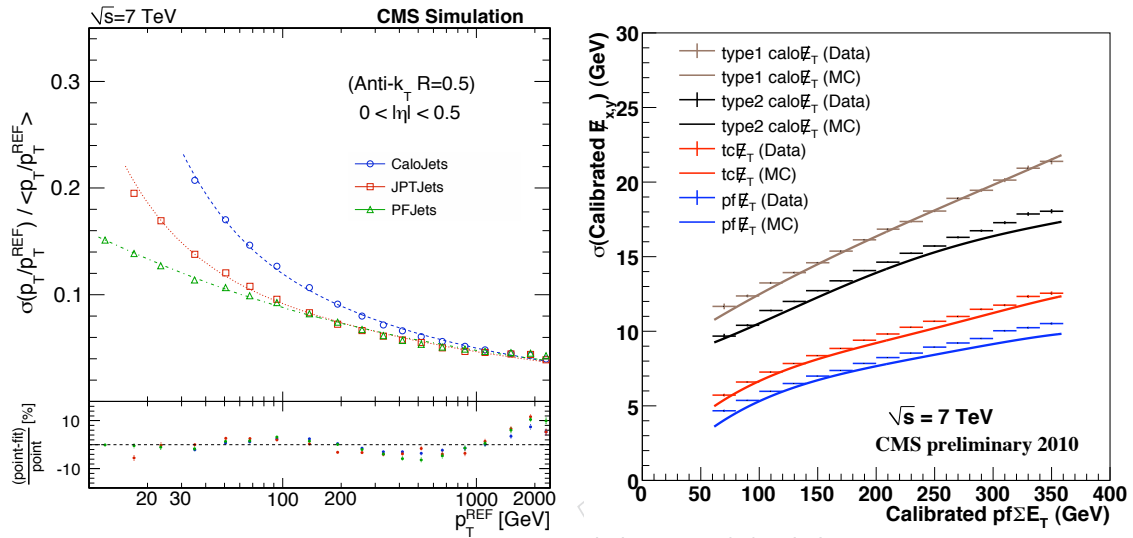
Figure 3.12: Performance measures for the HCAL: (a) the jet p_T resolution as a function of jet p_T for various different jet reconstructions and (b) the $\not{E}_T$ resolution as a function of Sum E_T for different $\not{E}_T$ reconstructions. Reproduced from [7, 8].

3.7 Muon System

The purpose of the muon system is identify muons and produce a muon trigger. It also provides a momentum measurement of the muons.

The muon system has a barrel region in the pseudorapidity range $\eta < 1.2$ and two endcaps with $1.2 < \eta < 2.4$. Standard drift tube chambers are used in the barrel and cathode strip chambers in the endcaps. The muon ionises the gas as it passes through the chamber. The resolution worsens with the p_T of the muon since the straighter the track the more difficult it is to accurately determine the curvature. The resolution is worse in the endcaps where the fake rate is higher and the magnetic field is less uniform. Figure 3.13 shows the muon p_T resolution as a function of muon p_T.

3.8 Trigger

With a soft QCD cross-section of $\sim 1\,\mathrm{mb}$ and a luminosity of $10^{33}\,\mathrm{cm}^{-1}\mathrm{s}^{-1}$ ($1\,\mathrm{nb}^{-1}\mathrm{s}^{-1}$) the event rate is $\sim 1\,\mathrm{MHz}$. However, most of these are uninteresting soft QCD events. Interesting events such as W/Z production, Higgs production or SUSY events have much smaller cross-sections. Figure 3.14 shows the cross-sections of various processes. Also
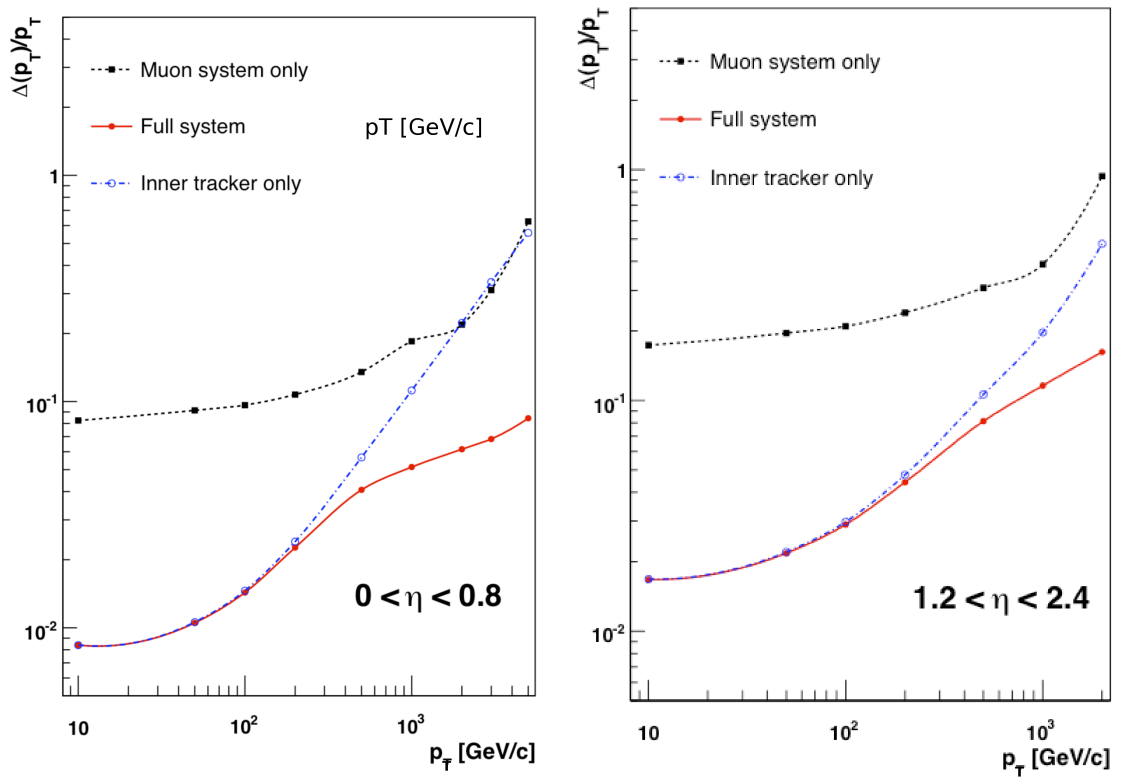
Figure 3.13: The muon p_T resolution as a function of muon p_T for (a) $\eta < 0.8$ and (b) $1.2 < \eta < 2.4$. Reproduced from [6].
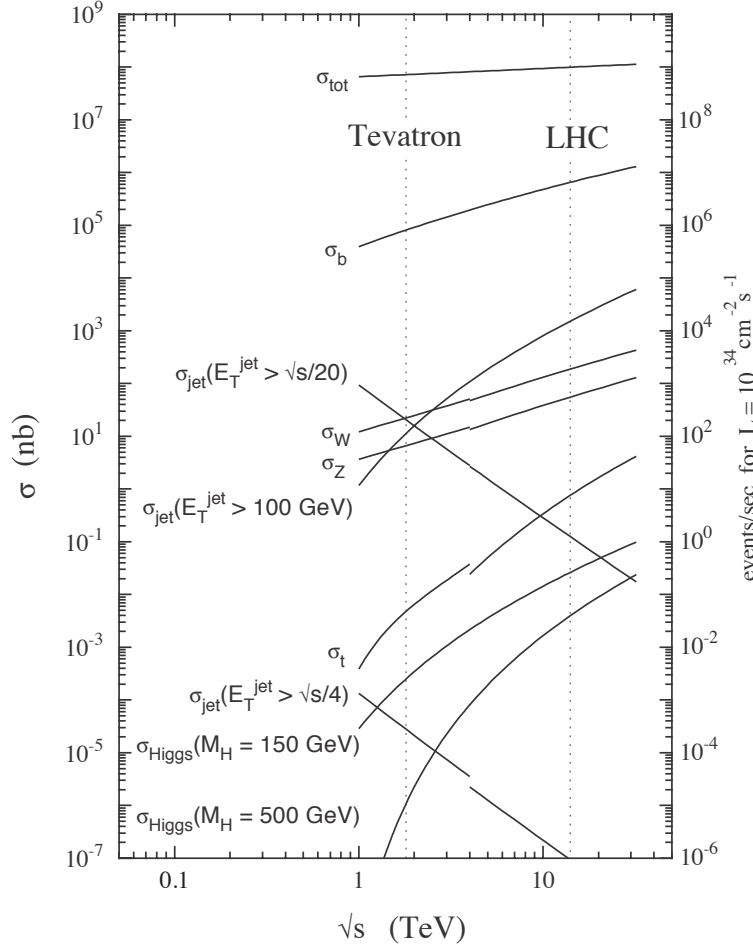
Figure 3.14: The cross-sections of various processes as a function of centre-of-mass energy.

there is a technical limit on the rate at which data can be read out. The CMS data acquisition (DAQ) bandwidth limits the event rate to $\sim 100\,\mathrm{kHz}$. Offline reconstruction and storage facilities further limit the rate to $\sim 100\,\mathrm{Hz}$. The goal of the trigger is to select the interesting events to read out and process.

There are two components to the trigger: Level 1 and Higher Level Trigger (HLT). The aim of the Level 1 trigger is to reduce the rate to $\sim 100\,\mathrm{kHz}$ to satisfy the constraint set by the DAQ bandwidth. It takes "trigger primitives" such as crystal energy sums calculated by on-detector hardware which are transferred by optical link from the CMS detector. The HLT is run on a farm of computers in a room above the CMS detector. It reconstructs physics objects and makes decisions based on the presence and quality of these to further

53

reduce the rate to $\sim 100\,\mathrm{Hz}$ to satisfy the constraint set by the storage and reconstruction facilities.

3.9   CMS Computing Model

CMS has produced O(100PB) of data and the quantity is growing. No single computer centre is capable of handling such a large quantity of data. The CMS computing model involves a network of data centres across the world (Figure 3.15) in a hierarchy of Tiers.

- Tier 0 is the data centre at CERN which is directly connected to the experiment. It stores the raw data and produces the first reconstruction which is subsequently transferred to Tier 1 sites.

- Data from Tier 0 is distributed to 8 Tier 1 sites. Each Tier 1 site is responsible for storing a second copy of the raw and reconstructed data. A lot of reprocessed data is also stored at the Tier 1 sites.

- Data from the Tier 1 sites is transferred to 38 Tier 2 sites. These data centres store data for analysis by CMS physicists. Data at the Tier 2 sites is not complete and is not stored permanently, but is updated according to the requirements of the ongoing analyses.

3.10   Photon Reconstruction

Photons and electrons make electromagnetic showers in the ECAL. Electromagnetic showers are reconstructed from the energy deposits in the ECAL crystals. The clustering algorithm starts with the energy deposits in single crystals and groups these together starting with the highest energy crystal. A strip 5 crystals wide in the η direction and with dynamic ϕ length is used to contain the energy in the cluster or clusters. To incorporate bremsstrahlung from electrons and converted photons, the strip can be extended in the ϕ direction. A description of the superclustering algorithm is given here [58].

Electromagnetic showers have a particular shower shape. Prompt photons can be distinguished from fakes by the shower shape. The main backgrounds to prompt photons come

Figure 3.15: A map showing the geographical distribution of CMS Tier 1 (red dots) and Tier 2 (blue dots) data centres. Reproduced from [9].

from single and multiple π^0s. The π^0 decays to two photons which produce an EM shower in the calorimeter. Shower shape alone does not distiguish single π^0 from prompt photons however it does reject multiple π^0s.

Fake photons from QCD jets tend to have plenty of activity in the surrounding detectors. In contrast, prompt photons tend to be isolated with little surrounding activity. Isolation is one of the variables used to select photons because of its background rejection power. There are three independent isolation measures based on the ECAL, the HCAL and the tracker.

Fake photons from jets also tend to have a hadronic component as well as an electromagnetic component while prompt photons are purely electromagnetic. Photons are distinguished from electrons by the tracker. Electrons, being charged particles, ionise the silicon and so leave a track while photons do not.

Based on these considerations, there are six variables used for the photon selection:

- **ECAL isolation** is defined as the sum of the energy deposited in the crystals of the ECAL in a circle $\Delta R = \sqrt{\Delta\eta^2 + \Delta\phi^2} = 0.4$ circle around the photon. A
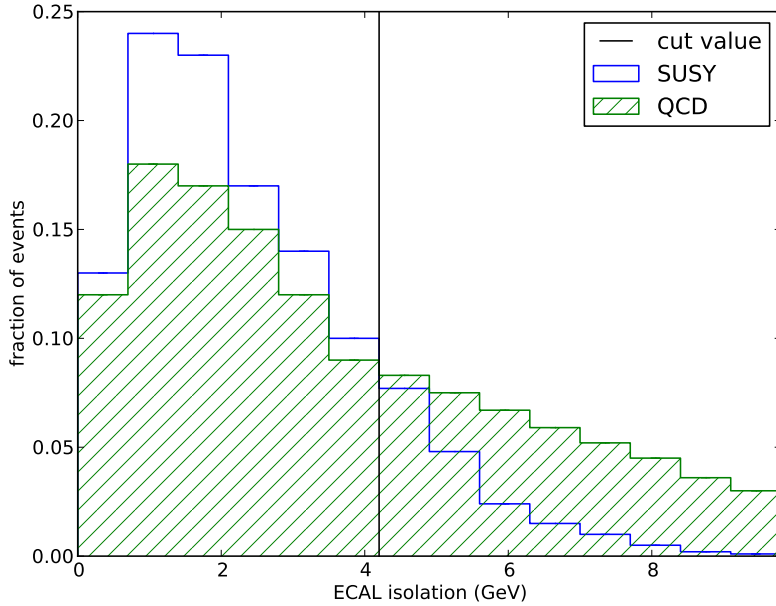
Figure 3.16: The ECAL isolation of photon candidates for a SUSY model and the QCD background along with the cut value used in this analysis.

smaller circle of $\Delta R = 0.1$ around the photon is excluded from the isolation sum to avoid counting the photon itself in the isolation. Also a strip along ϕ of width $\Delta\eta = 0.04$ is excluded from the isolation sum. The $\Delta\eta$ width is chosen to avoid including bremsstrahlung from electrons and photon conversions. Figure 3.16 shows a plot of the ECAL isolation of photon candidates for a SUSY model and the QCD background along with the cut value used in this analysis.

- **HCAL isolation** is defined as the sum of the energy deposited in the HCAL towers in a $\Delta R = 0.4$ circle around the photon position. A smaller circle of $\Delta R = 0.1$ is excluded from the isolation sum to avoid counting rear-leakage from high energy photons in the isolation. Figure 3.17 shows a plot of the HCAL isolation of photon candidates for a SUSY model and the QCD background along with the cut value used in this analysis.

- **Track isolation** is defined as the sum of the p_T of tracks inside a cone of $\Delta R = 0.4$ around the photon and toward the primary vertex. A smaller cone of $\Delta R < 0.1$ is excluded from the isolation sum. Figure 3.18 shows a plot of the track isolation of
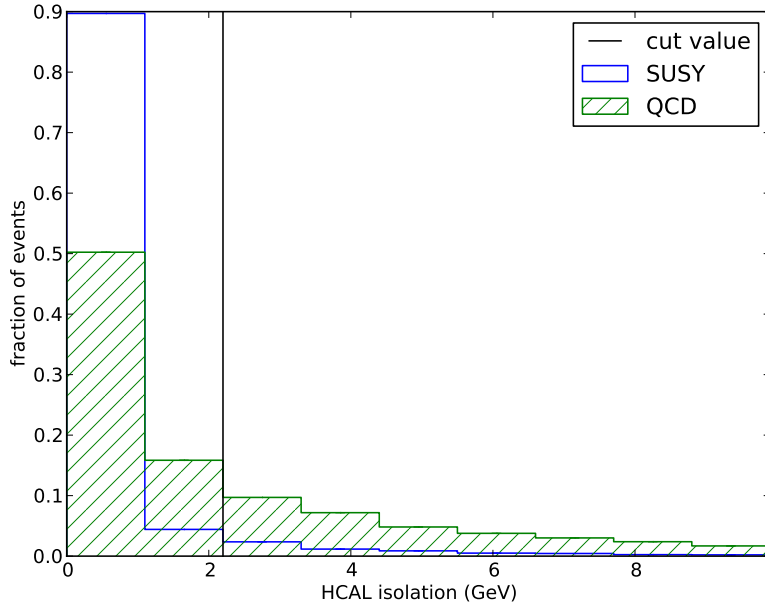
Figure 3.17: The HCAL isolation of photon candidates for a SUSY model and the QCD background along with the cut value used in this analysis.

photon candidates for a SUSY model and the QCD background along with the cut value used in this analysis.

- **H/E** is the ratio of the hadronic energy deposited in the HCAL behind the photon to the photon energy. Jets faking photons are likely to have a significant amount of hadronic energy while for prompt photons the amount of hadronic energy is likely to be small. Figure 3.19 shows a plot of the H/E of photon candidates for a SUSY model and the QCD background along with the cut value used in this analysis.

- **Shower Shape** ($\sigma_{i\eta i\eta}$). The width of the shower in the η direction is used as a measure of the shower shape. The η direction rather than the ϕ direction is used because the magnetic field can cause electromagnetic showers to be spread out in ϕ. $\sigma_{\eta\eta}$ is the r.m.s width of the shower in the η direction. The variable used here is $\sigma_{i\eta i\eta}$, which calculates the width in terms of number of crystals in the η direction rather than η itself. This is better because it does not count the gaps between crystals (where there is no showering) in the width and it is not distorted by the geometry of the detector in the end-cap region. Figures 3.20 and 3.21 show plots of the shower

57
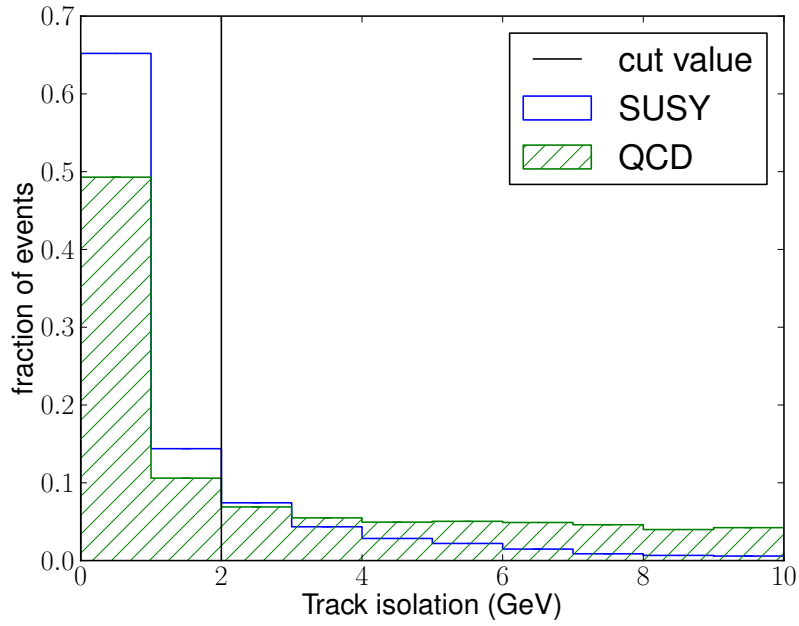
Figure 3.18: The track isolation of photon candidates for a SUSY model and the QCD background along with the cut value used in this analysis.
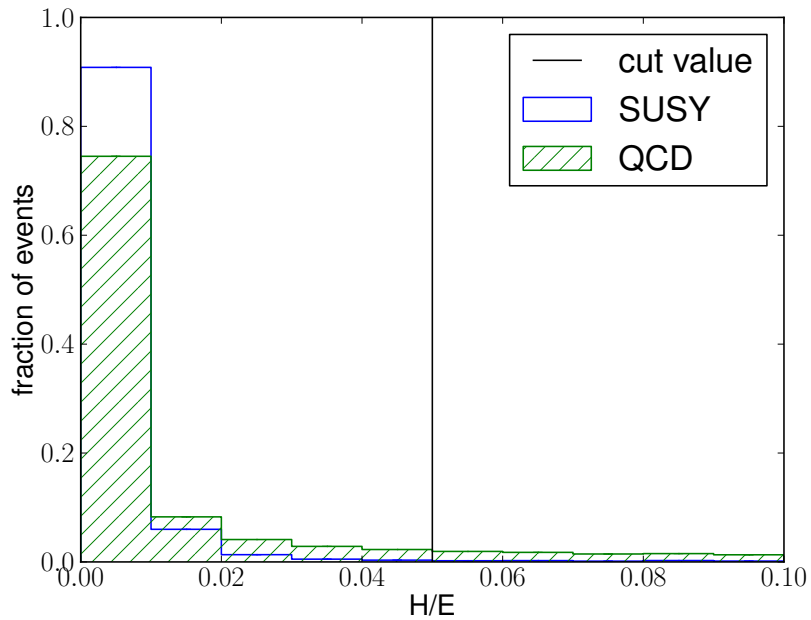
Figure 3.19: The H/E of photon candidates for a SUSY model and the QCD background along with the cut value used in this analysis.
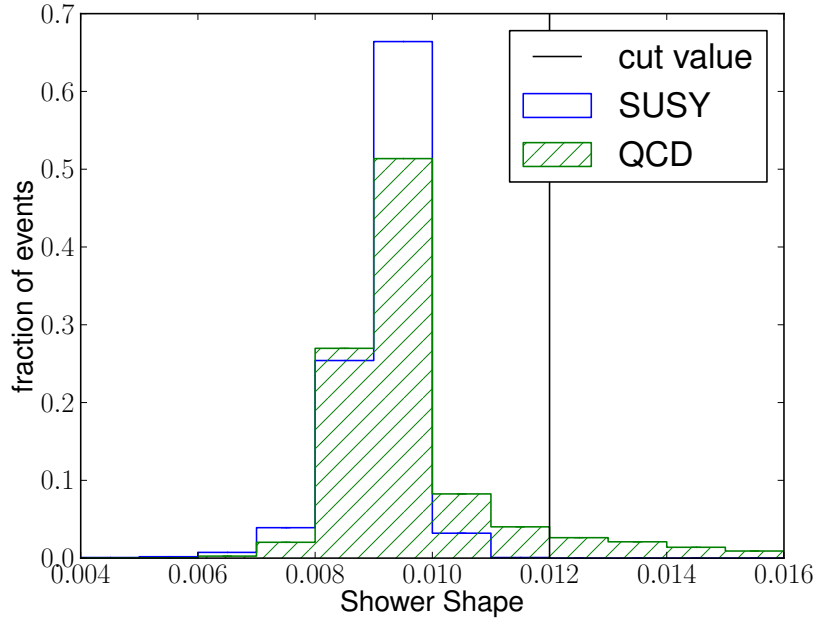
Figure 3.20: The shower shape of photon candidates in the ECAL barrel for a SUSY model and the QCD background along with the cut value used in this analysis.

shape of photon candidates in the ECAL barrel and ECAL end-cap respectively. The distributions are shown for a SUSY model and the QCD background along with the cut value used in this analysis.

- **Pixel Seed**. A pixel seed is a track stub in the pixel detector that is the first step in track reconstruction. The photon selection requires that there is no pixel seed corresponding to the electromagnetic shower.

3.11   Jet Reconstruction

Jets are collimated bunches of hadrons originating from partons (quarks and gluons) after fragmentation and hadronisation. Jets are reconstructed based on energy deposits in the detector using the Anti-KT jet algorithm with a cone size of $\Delta R = 0.5$. The Anti-KT jet algorithm is a clustering, cone algorithm which does not suffer from the problem of infra red and collinear divergences [59].

Under the Anti-KT algorithm energy deposits are clustered together within a cone ac-
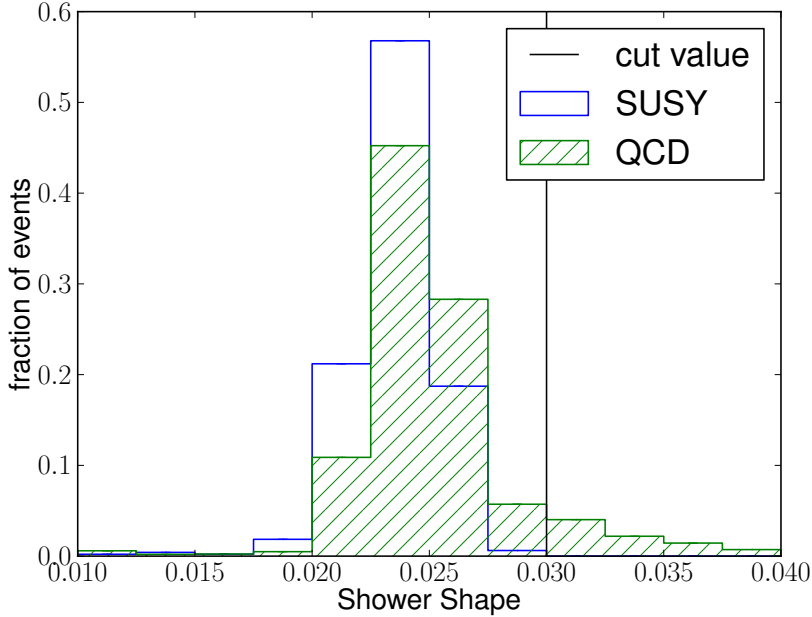
Figure 3.21: The shower shape of photon candidates in the ECAL end-cap for a SUSY model and the QCD background along with the cut value used in this analysis.

cording to their distance from each other. The "distance", d_{ij}, between objects (energy deposits/particles) is defined by Equation 3.3.

$$d_{ij} = min(p_{T1}^{-2}, p_{T2}^{-2})\frac{\Delta_{ij}}{R} \tag{3.3}$$

$\Delta_{ij} = \sqrt{\Delta\eta^2 + \Delta\phi^2}$ and R is the radius of the cone.

The Anti-KT algorithm is the most widely used within CMS because it has good energy resolution and good efficiency [60].

3.12 ECAL Spikes

ECAL Spikes are isolated energy deposits in the ECAL which do not come from EM showers. They tend to be single crystal energy deposits in the ECAL which are often not vetoed by the shower shape variable. The origin of ECAL spikes is energy deposited directly into the sensitive region of the photodetectors (without showering in the ECAL). ECAL spikes lead to fake photons and fake $\not{E}_T$. There are two properties which characterise ECAL

spikes: topology and timing. Some spikes occur at the same time as the rest of the event from pions and other particles in the hadronic shower, while others are out of time with the rest of the event due to slow neutrons travelling from where they were created (the hadronic shower) to the photodetector where they interact. A cut of $1 - e4/e1 < 0.96$ is made to avoid spikes. 1 - e4/e1 is the "Swiss Cross" variable in which e1 is the highest energy crystal in a 3x3 array and e4 is the energy of the four adjacent crystals. The vast majority of spikes are vetoed by the swiss cross cut. Many of the remaining are double spikes (where energy is deposited in the photodetectors of two adjacent crystals). These spikes are vetoed by requiring $e2/e9 < 0.96$ and $|t| < 5\,\mathrm{ns}$, t is the timing of the signal relative to the bunch crossing time. e2 is the energy of the highest energy crystal plus the energy of the highest energy adjacent crystal in a 3x3 array. e9 is the total energy of all the crystals in the 3x3 array. The distribution of spikes remaining after the swiss cross cut is illustrated by Figure 3.22.
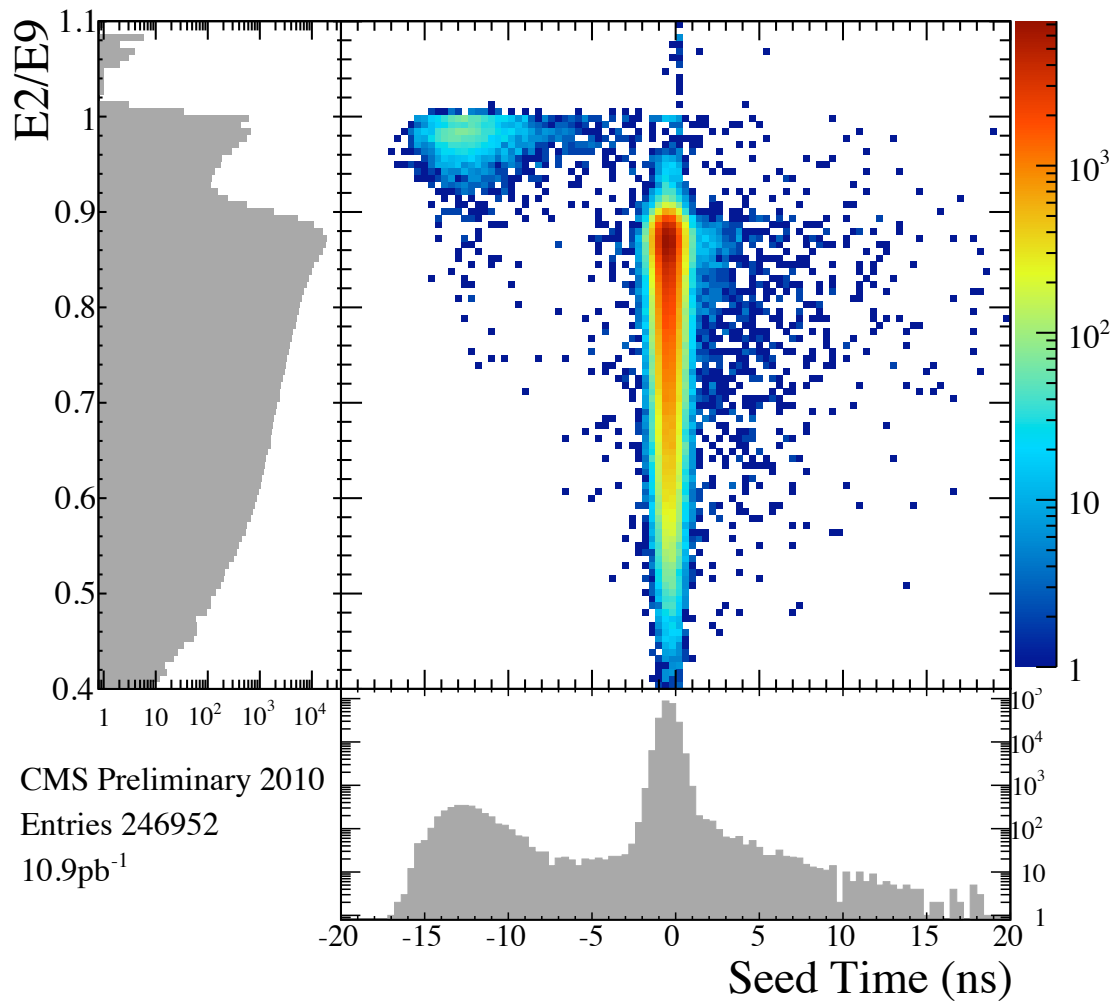
Figure 3.22: A plot of e2/e9 vs seed time to show how double crystal ECAL spikes are vetoed.

Chapter 4

Data, Trigger and Event Selection

4.1   Data

The search for GMSB described in this thesis uses $1.1\,\mathrm{fb}^{-1}$ of data taken from March to June 2011. This corresponds to the data set used for the results presented at the International Europhysics Conference in High Energy Physics in July 2011.

The centre of mass energy of the proton-proton collisions is $7\,\mathrm{TeV}$ which makes the LHC the highest energy particle collider to date. A higher centre of mass energy increases the production cross-section of certain processes, for example stong production SUSY, and also enables the production of more massive particles. It should be noted that the important energy is not the centre of mass energy of the proton collision, but that of the parton collision which is $\sim 1\,\mathrm{TeV}$ on average.

The instantaneous luminosity has increased over the data taking period by increasing the intensity of the beams and the number of bunches. Increasing the intensity of the beams leads to more interactions per bunch crossing – an effect called pile-up. During the period when this data was taken the luminosity was $\sim 10^{33}\,\mathrm{cm}^{-2}\mathrm{s}^{-1}$.

Figure 4.1 shows the integrated luminosity recorded by CMS over time until September 2011.
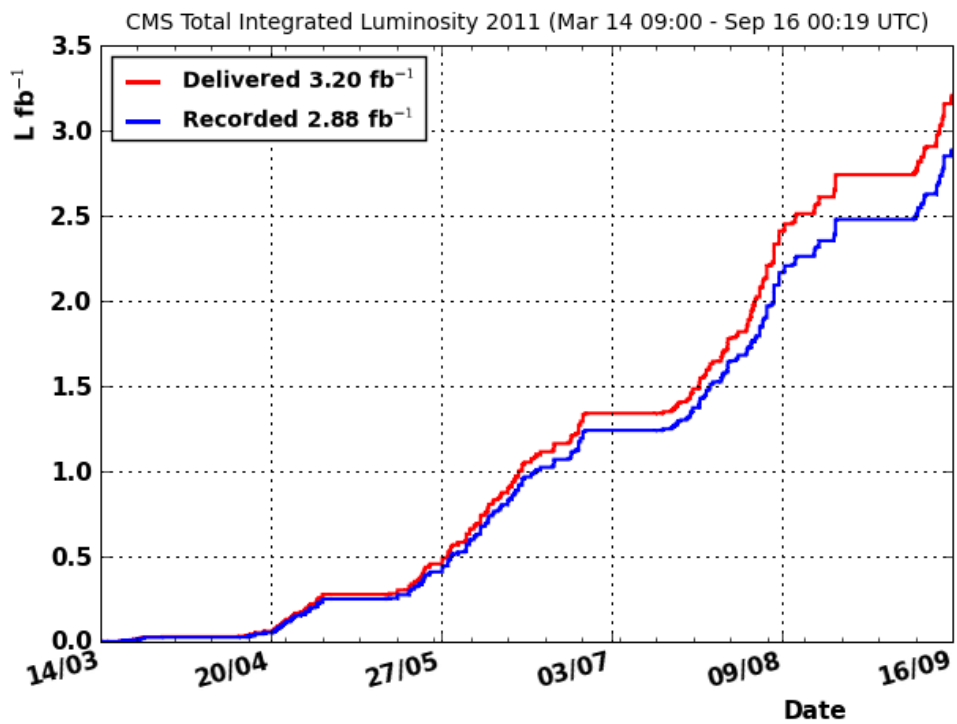
Figure 4.1: The integrated luminosity vs time delivered to (red) and recorded by (blue) CMS during stable beams at $\sqrt{s} = 7\,\text{TeV}$.

4.2 H_T and Missing Transverse Energy ($\not{E}_T$)

H_T is the scalar sum of the p_T of all jets with $p_T > 40\,\mathrm{GeV}$. The H_T gives a measure of the activity in the event.

$$H_T = \sum p_T^{jet} \tag{4.1}$$

Particles such as neutrinos and the LSP in SUSY events are not detected by CMS. Momentum conservation in the proton collision means that the undetected particles show up as an imbalance of reconstructed particles. $\not{E}_T$ is the negative vector sum of the transverse momenta of all the reconstructed particles. The transverse component is used because much of the longitudinal momentum goes down the beampipe (i.e. outside the acceptance of the detector). For high energy photons and jets the most accurate measurement of the momentum comes from the energy in the calorimeters. The transverse energy, $\vec{E}_T$, of an energy deposit E is calculated using Equation 4.2. The missing transverse energy $\not{E}_T$ is given by Equation 4.3.

$$\vec{E}_T = E \sin\theta \cos\phi \vec{x} + E \sin\theta \sin\phi \vec{y} \tag{4.2}$$

$$\not{E}_T = \left| -\sum \vec{E}_T \right| \tag{4.3}$$

H_T and $\not{E}_T$ are the two variables used to search for GMSB in the data. Figures 4.2 and 4.3 show the distribution of H_T and $\not{E}_T$ in the signal events compared to the background from MC.

4.3 Monte Carlo Samples

Events of QCD processes, SUSY signal models and Electroweak processes are generated using Monte Carlo (MC) techniques followed by detector simulation. The simulated data gives predictions to be compared with obsevations and used to validate analysis methods. The samples are generated using Pythia 6 [61] and GEANT 4 [62] is used for the detector simulation.

Pile-up is simulated in the MC samples however the MC does not reproduce the vertex mutiplicity distribution seen in the data. To correctly simulate pile-up the MC is re-weighted
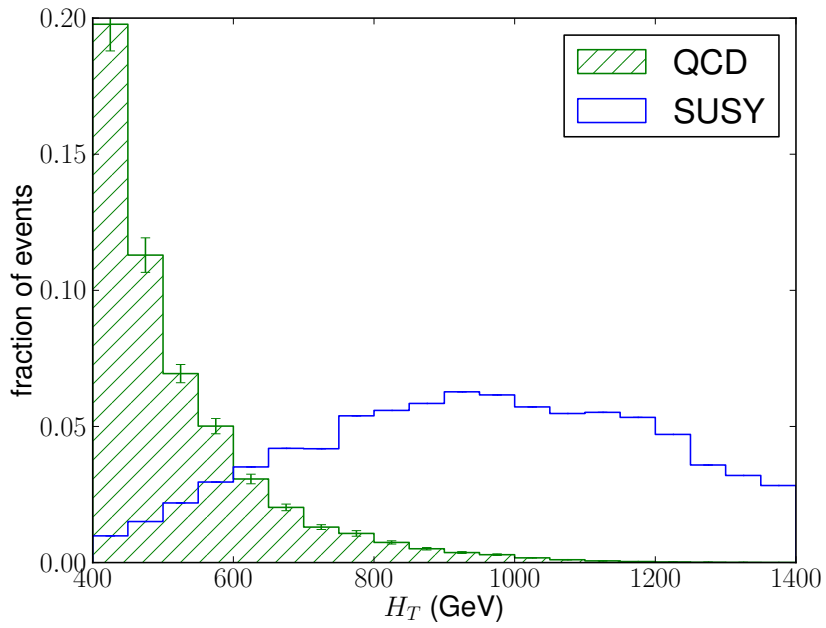
Figure 4.2: The H_T distribution in SUSY events compared to the background from MC samples.
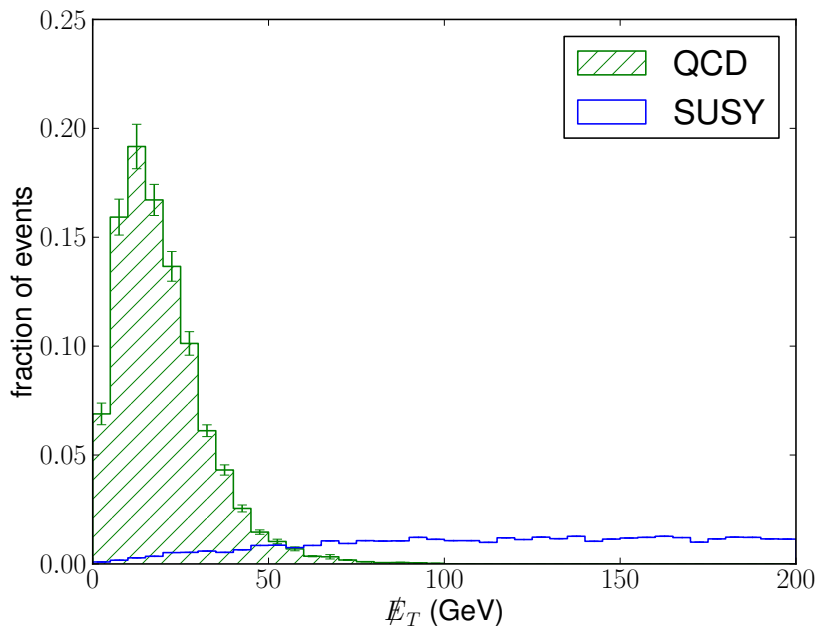
Figure 4.3: The $\not{E}_T$ distribution in SUSY events compared to the background from MC samples.

66
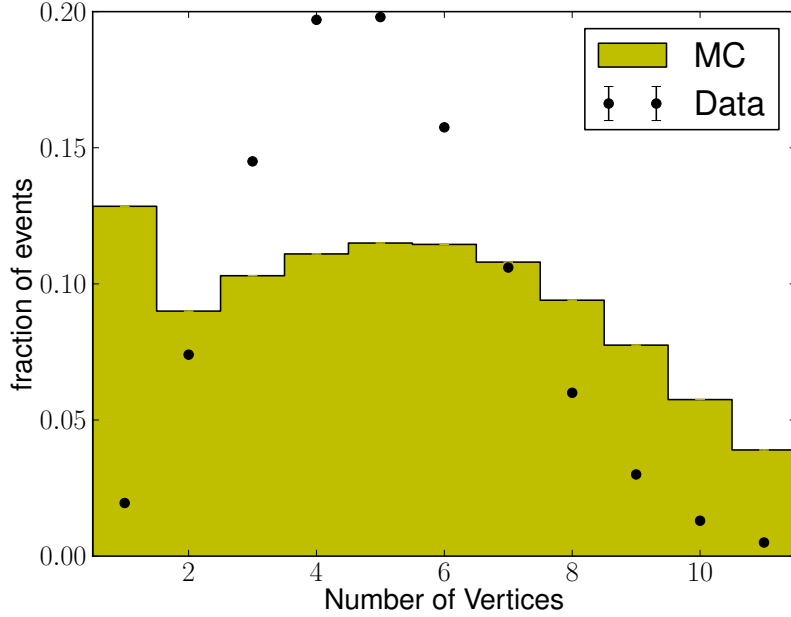
Figure 4.4: The distribution of number of vertices in the data compared to the MC

to reproduce the number of vertices distribution seen in the data. Figure 4.4 shows the distribution of number of vertices in the data and MC.

Figure 4.5 shows plots of H_T and $\not{E}_T$ to show how accurately the MC models the data. The prediction is good for H_T, but the $\not{E}_T$ distribution is broader in the data than the MC. This shows that jets with $p_T > 40\,\text{GeV}$ are well described by the MC, but lower energy jets and unclustered energy are less well modelled.

4.4   Trigger

Based on the properties of strong production GMSB, a photon $+$ H_T trigger is ideal for this search. Table 4.1 shows a list of all the photon $+$ H_T triggers in the 2011 data with the corresponding L1 seed and the rate at $10^{33}\,\text{cm}^{-2}\text{s}^{-1}$. The $70\,\text{GeV}$ photon $+$ $350\,\text{GeV}$ H_T trigger is used for this search.

As the luminosity has increased more stringent trigger requirements have been necessary
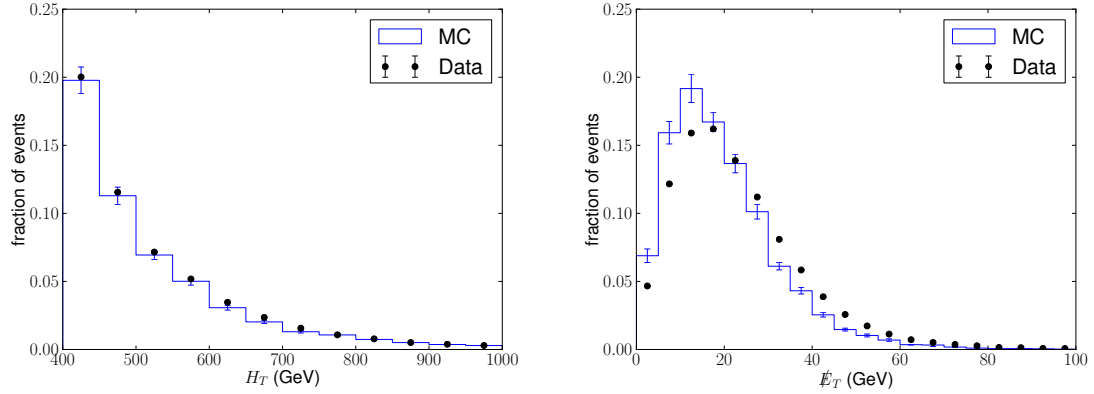
Figure 4.5: Plots of H_T and $\not{E}_T$ in data and Monte Carlo to show how accurately the Monte Carlo models the data.

	L1 seed	Rate at $10^{33}\,\mathrm{cm}^{-2}\mathrm{s}^{-1}$
HLT_Photon60_CaloIdL_HT200	L1_SingleEG20	(pre-scaled)
HLT_Photon70_CaloIdL_HT200	L1_SingleEG20	(pre-scaled)
HLT_Photon70_CaloIdL_HT300	L1_SingleEG20	4 Hz
HLT_Photon70_CaloIdL_HT350	L1_SingleEG20	2.5 Hz

Table 4.1: A table of the photon and H_T triggers available in the 2011 data along with the corresponding L1 seed and rate at $10^{33}\,\mathrm{cm}^{-2}\mathrm{s}^{-1}$.
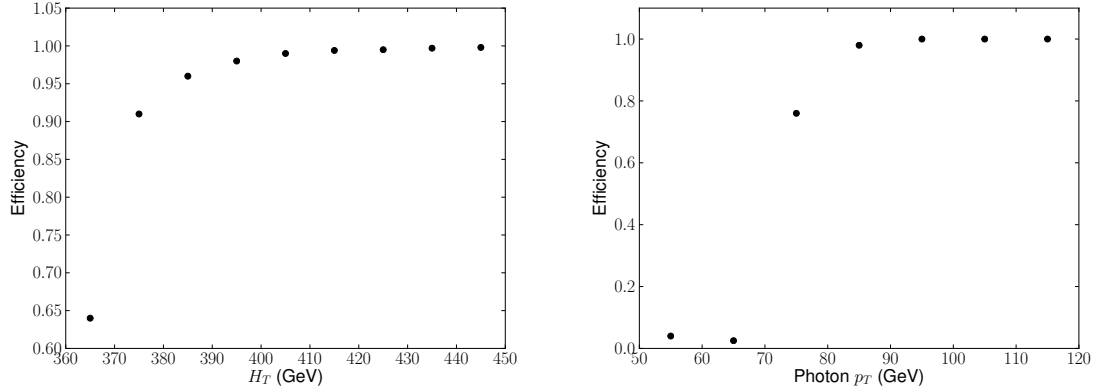
Figure 4.6: The trigger efficiency vs H_T (left) and vs photon p_T (right) relative to a lower threshold trigger.

to keep the data rate manageable. If the rate of a trigger becomes too high, the trigger must be pre-scaled. This means that only every n^{th} event which fires the trigger is read out where n is the prescale factor.

If there were no offline jet energy corrections, then the trigger H_T value would be identical to the offline H_T value and therefore there would be no trigger inefficiency coming from the H_T cut. Due to offline jet energy corrections there is an inefficiency for events close to the H_T boundary. The offline cuts for H_T and photon p_T are chosen to avoid any inefficiency of the trigger due to the thresholds.

The efficiency of the trigger is evaluated with respect to a lower threshold trigger to determine at which H_T value the offline cut should be placed for the trigger to be fully efficient for the event selection. The thresholds are chosen such that all the events with H_T above the offline cut will pass the lower threshold trigger. Some of the events which would have passed the offline H_T cut will not pass the trigger because of the offline jet energy corrections and some events will pass the trigger despite having an offline H_T below the trigger threshold. The offline H_T distribution of events passing both triggers is divided by the offline H_T distribution of events passing the lower threshold trigger. This does not give an absolute efficiency of the trigger. The resulting efficiency curve shows where to put the off-line cut in H_T such that the ineffeciency due to the H_T cut is negligible. Figure 4.6 shows the trigger efficiency against H_T and photon p_T.

69

Variable	Cut value
ECAL isolation	$4.2 + 0.006 p_T$
HCAL isolation	$2.2 + 0.0025 p_T$
Track isolation	$2.0 + 0.001 p_T$
H/E	0.05
Shower Shape	0.012 (EB), 0.030 (EE)
No Pixel Seed	True

Table 4.2: The photon selection cuts.

4.5 Photon Selection

Photons are selected based on variables such as isolation and shower shape which are designed to select prompt photons over fakes from jets. The photon reconstruction is described in detail in Section 3.10. The cut values on each of the photon selection varaibles are listed in Table 4.2. These cut values were chosen to have $90\,\%$ efficiency for prompt photons according to MC [63].

4.6 Jet Selection

Two jets with $p_T > 80\,\mathrm{GeV}$ and $|\eta| < 2.5$ are required. The η threshold corresponds to the tracker boundary. The p_T threshold should be chosen as high as possible to reject background, but with the signal efficiency close to 100%. Figure 4.7 shows the signal efficiency and the background rejection as a function of the jet p_T threshold.

4.7 Event Selection

The event selection criteria are listed below.

- $H_T > 400\,\mathrm{GeV}$

- ≥ 2 jets

- ≥ 1 photon

- $\not{E}_T > 50\,\mathrm{GeV}$
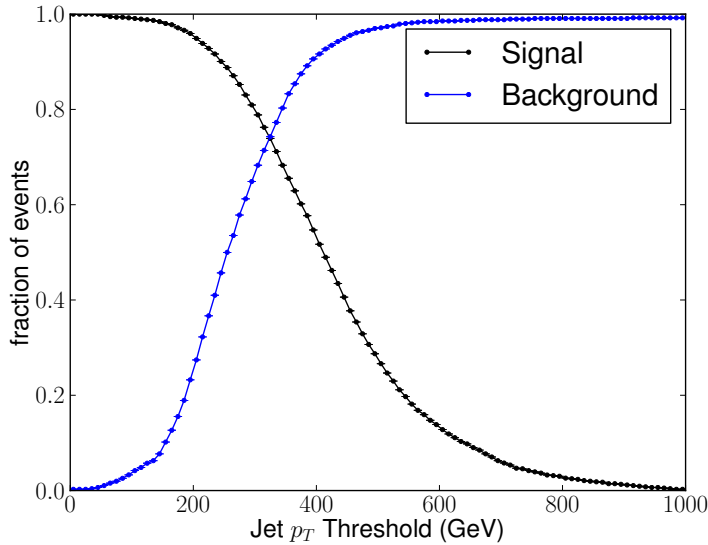
Figure 4.7: A plot of the efficiency of the signal (black) and the background rejection (blue) as a function of the jet p_T threshold.

A H_T cut is applied because strongly produced SUSY events have high H_T since high mass particles (squarks and gluinos) are produced. The value of this cut is motivated by the desire for the trigger to be fully efficient for the event selection. Figure 4.6 shows that the trigger becomes fully efficient in H_T at around $400\,\mathrm{GeV}$.

The ≥ 2 jets cut is well motivated from the SUSY perspective: strong production SUSY events start with two squarks/gluinos each of which decay to a quark/gluon (which forms a jet in the detector) and the next SUSY particle in the mass hierarchy.

In strong production GMSB the Next-to-Lightest SUSY Particle (NLSP) is the neutralino ($\tilde{\chi}^0$) which decays to a photon and a gravitino. At least two photons are expected in each event. However, due to the high activity in these events, photons often fall inside the cone of a jet and so only one photon is reconstructed. Hence the ≥ 1 photon cut.

The background estimation is done in bins of $\not{E}_T$ and H_T, but an initial $\not{E}_T$ cut is made to avoid the low $\not{E}_T$ bins where there is no sensitivity due to the huge amount of background. Figure 4.8 shows the signal efficiency and the background rejection as a function of $\not{E}_T$
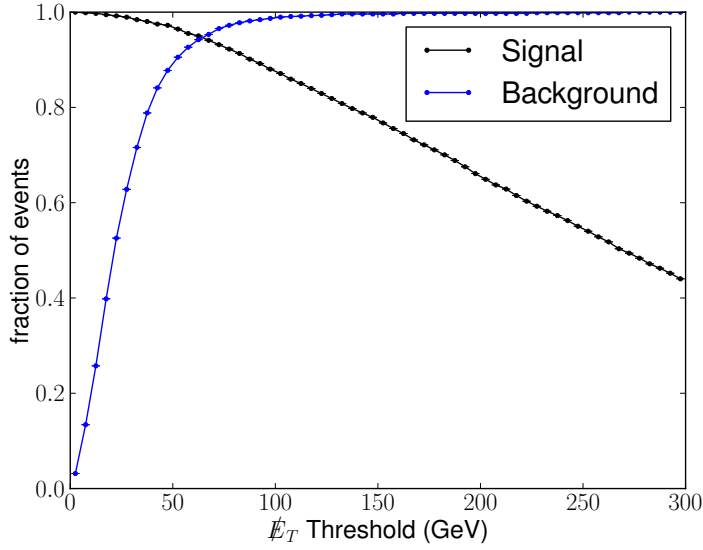
Figure 4.8: The signal efficiency (black) and background rejection (blue) as a function of $\not{E}_T$ cut.

cut.

The total number of events passing the selection in bins of H_T and $\not{E}_T$ is given in Table 4.3.

4.8 Outline of the Search

The event selection is applied to the data and the number of events passing the selection is recorded in bins of $(H_T, \not{E}_T)$.

$\not{E}_T \downarrow |H_T \rightarrow$	$400 - 500\,\mathrm{GeV}$	$500 - 600\,\mathrm{GeV}$	$600 - 700\,\mathrm{GeV}$	$700\,\mathrm{GeV}+$
$50 - 100\,\mathrm{GeV}$	835	591	398	609
$100 - 150\,\mathrm{GeV}$	35	30	26	44
$150 - 200\,\mathrm{GeV}$	5	5	2	7
$200\,\mathrm{GeV}+$	9	4	4	7

Table 4.3: The number of events passing the selection in bins of H_T and $\not{E}_T$. The bin used to search for signal is on the bottom right ($H_T > 700\,\mathrm{GeV}$, $\not{E}_T > 200\,\mathrm{GeV}$).

An estimate is made for the expected number of background events in each $(H_T, \not{E}_T)$ bin. The background estimation is done using a sample from data and checked using the MC.

A prediction for the number of signal events in the only significant bin ($H_T > 700\,\text{GeV}$, $\not{E}_T > 200\,\text{GeV}$) is made by applying the event selection to the signal MC. The prediction is made for a variety of signal models with different squark mass and gluino mass. Systematic uncertainties are estimated by varying within their uncertainties the variables that could affect the signal prediction.

The CLs method is used to exclude the signal at $95\,\%$ CL in the squark mass vs gluino mass parameter space.

Chapter 5

Background Estimation

5.1   Introduction

The Standard Model backgrounds to the search are estimated in 16 bins of $(H_T, \not{E}_T)$. The H_T bins are $400-500\,\mathrm{GeV}$, $500-600\,\mathrm{GeV}$, $600-700\,\mathrm{GeV}$ and $> 700\,\mathrm{GeV}$ and the $\not{E}_T$ bins are $50-100\,\mathrm{GeV}$, $100-150\,\mathrm{GeV}$, $150-200\,\mathrm{GeV}$ and $> 200\,\mathrm{GeV}$. Only the $(H_T > 700\,\mathrm{GeV}$, $\not{E}_T > 200\,\mathrm{GeV})$ bin is significant in terms of setting a limit on the GMSB cross-section. The other bins are used only to give confidence in the background estimation procedure.

The main background comes from QCD processes. These events have only fake $\not{E}_T$ due to detector imperfections. The size of the QCD background is estimated using a control sample from the data.

The electroweak background is small in comparison to the QCD background. Electroweak processes can contribute real $\not{E}_T$ through the production of neutrinos that are not detected. The size of the electroweak background is estimated using MC.

5.2   QCD Background

The largest background comes from QCD processes. There are three different components to the QCD background:

- **Fakes from jets $(\pi^0 \to \gamma\gamma)$:** π^0s are one of the main constituents of jets. The two photons from a high energy π^0 can easily be mistaken for a single photon. Most π^0s

will be non-isolated due to the surrounding jet. However there is a distribution of isolation and given the large cross section of QCD, some of these events will end up in the isolated tail.

- **Prompt γ+jet:** In these events the photon comes directly from the parton hard scattering. The other jet can come from gluon radiation or jet fragmentation. These events contain prompt photons which tend to be isolated and have good shower shape.

- **QCD jets with ISR/FSR:** A QCD jets event where an initial state quark or final state quark radiates a photon. These events also contain prompt photons which tend to be isolated and have good shower shape. The cross section of this process falls with the p_T of the photon.

QCD events are balanced in the transverse plane. All three sources of QCD background have only fake $\not{E}_T$. Fake $\not{E}_T$ can come from the HCAL resolution, severe mismeasurements such as "dead" regions, poor HCAL response or from fluctuations inherent in the hadronic showering process.

In the ECAL there are single crystals and groups of crystals (ECAL trigger towers) which are non-functioning or partially functioning resulting in "dead" areas – energy deposited in these regions is not reconstructed resulting in fake missing transverse energy. Figure 5.1 shows a map of the ECAL barrel with the dead regions marked.

Poor HCAL response is another cause of large fake $\not{E}_T$. Sometimes a jet is reconstructed with a much lower p_T than it actually has. Such mismeasurements are extremely unusual (at a rate smaller than 1 in 10^5 events) and not at all well understood. These are not correlated with any specific region of the detector.

The core resolution is approximately Gaussian in x and y components of $\not{E}_T$ while the severe mismeasurements contribute a non-Gaussian tail to the $\not{E}_T$ distribution. Both components scale with H_T. The core resolution scales as $\sim \sqrt{H_T}$ while the tails increase because higher H_T events contain higher p_T objects which give larger $\not{E}_T$ when missed.
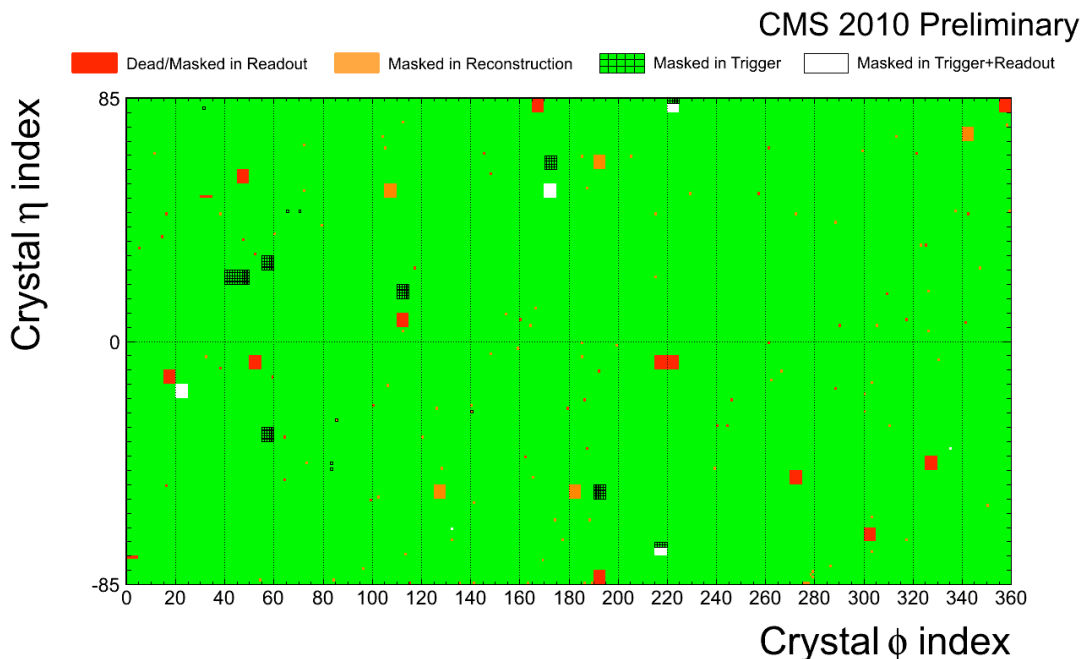
Figure 5.1: A map of the ECAL barrel showing the dead regions. Of the 2448 trigger towers in the ECAL barrel, 27 are dead. Reproduced from [10].

Any background estimation method needs to be able to estimate these detector effects. If the Monte Carlo were to be used we would be relying on its ability to correctly model all the causes of fake $\not{E}_T$. Not just the core resolution but also the $\not{E}_T$ tail with severe mismeasurements. Using a control sample from data gives a perfect simulation of the CMS detector. The problem is reduced to finding a control sample with the same kinematic properties as the selected sample rather than trying to simulate the most extreme elements of detector response.

A control sample is defined to contain events which pass all the selection criteria except for the isolation. This control sample is used to estimate the $\not{E}_T$ shape of the QCD background in each H_T bin. The absolute number of events is obtained by normalising the $\not{E}_T$ distribution to the number of events with $\not{E}_T < 50\,\mathrm{GeV}$.

The assumption in this method is that the control sample has the same $\not{E}_T$ distribution as the selected sample in each H_T bin. The control sample is very similar to the selected sample. It has the same objects with the same kinematic cuts. All events contain at least

76

one photon with good shower shape. The only difference is that in the control sample the photon is non-isolated while in the selected sample it happens to be isolated. Although they contain the three sources of QCD background in different proportions, in both cases the source of $\not{E}_T$ is the same: detector effects. So we can expect them to have the same $\not{E}_T$ distributions.

The background estimation is shown to work in Monte Carlo and in data using a sideband region. Figure 5.2 shows the regions used for the background estimation. The (non-isolated) control sample is used to estimate the background in the (isolated) selected sample. The sideband region is used to check that the background estimation works i.e. the non-isolated and isolated samples have the same $\not{E}_T$ distribution.

To assess how well the background estimation technique works, the $\not{E}_T$ distribution of the selected events is compared to the prediction of the $\not{E}_T$ distribution using the control sample. This is done using the MC and the sideband region to give two independent checks each with different qualities. The check of the background estimation using the MC shows how well the technique works in principle. It has the advantage that it is probing a kinematically identical region to the data, but the disadvantage that the MC does not accurately reproduce the $\not{E}_T$ distribution in data. The check of the background estimation technique using the sideband region in data uses a kinematically similar, but not idential region. It has the advantage that being from data it reliably reproduces the detector idiosyncrasies which cause the fake $\not{E}_T$.

Figure 5.3 shows the $\not{E}_T$ distribution in the MC for the selected events compared to the prediction of the $\not{E}_T$ distribution using the control sample. The data are split bins of H_T: $400 - 500\,\mathrm{GeV}$, $500 - 600\,\mathrm{GeV}$, $600 - 700\,\mathrm{GeV}$ and $700\,\mathrm{GeV}$. A straight line is fitted to the difference plot to give a quantatative measure of the performance of the background estimation. The important number to compare is the number of events in the search bin ($H_T > 700\,\mathrm{GeV}$, $\not{E}_T > 200\,\mathrm{GeV}$), which is predicted to be 0.17 ± 0.04 using the control sample in the MC. The true value in the MC is 0.24 ± 0.06.

Figure 5.4 shows the predicted and observed $\not{E}_T$ distribution in the sideband region. The number of events in the search bin for the sideband region is predicted to be 0.09 ± 0.04
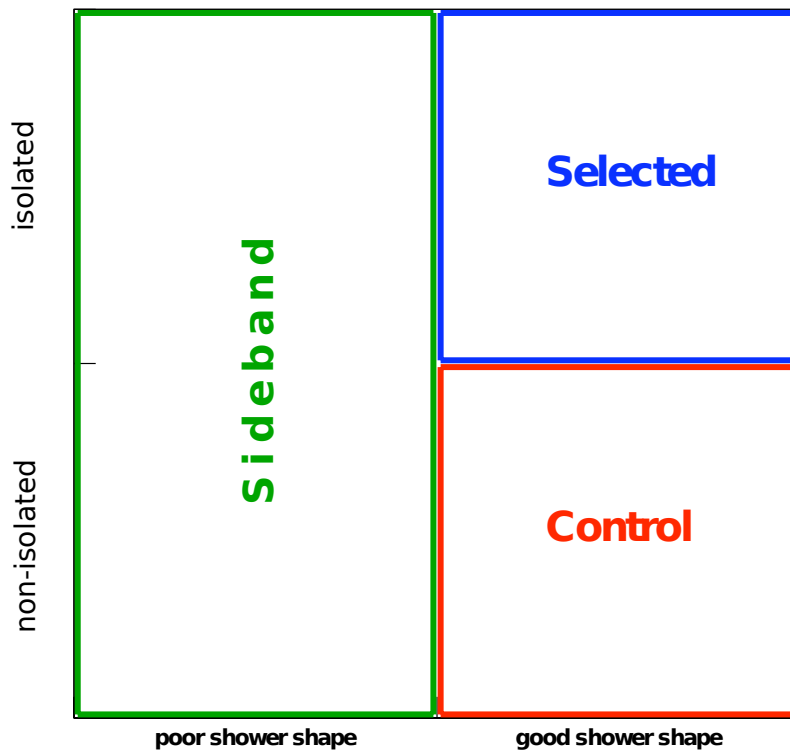
Figure 5.2: A graphic showing the layout of the regions used for the QCD background estimation. The control sample is used to estimate the $\not{E}_T$ distribution in the selected sample. The sideband region is used to check that the background estimation works.
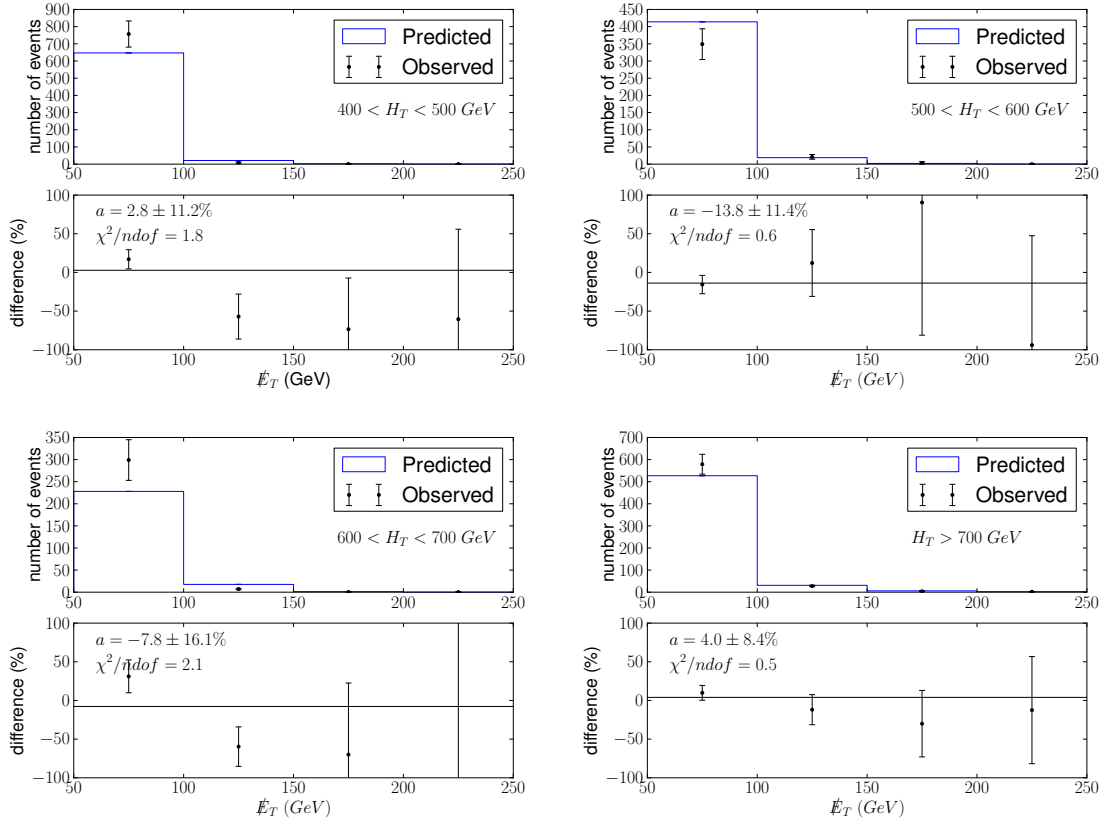
Figure 5.3: The estimation of the $\not{E}_T$ distribution of the background using the control sample in the MC compared to the true $\not{E}_T$ distribution of the background according to the MC in bins of H_T. The percentage difference between the estimated and observed number of events is plotted and a flat line is fitted.
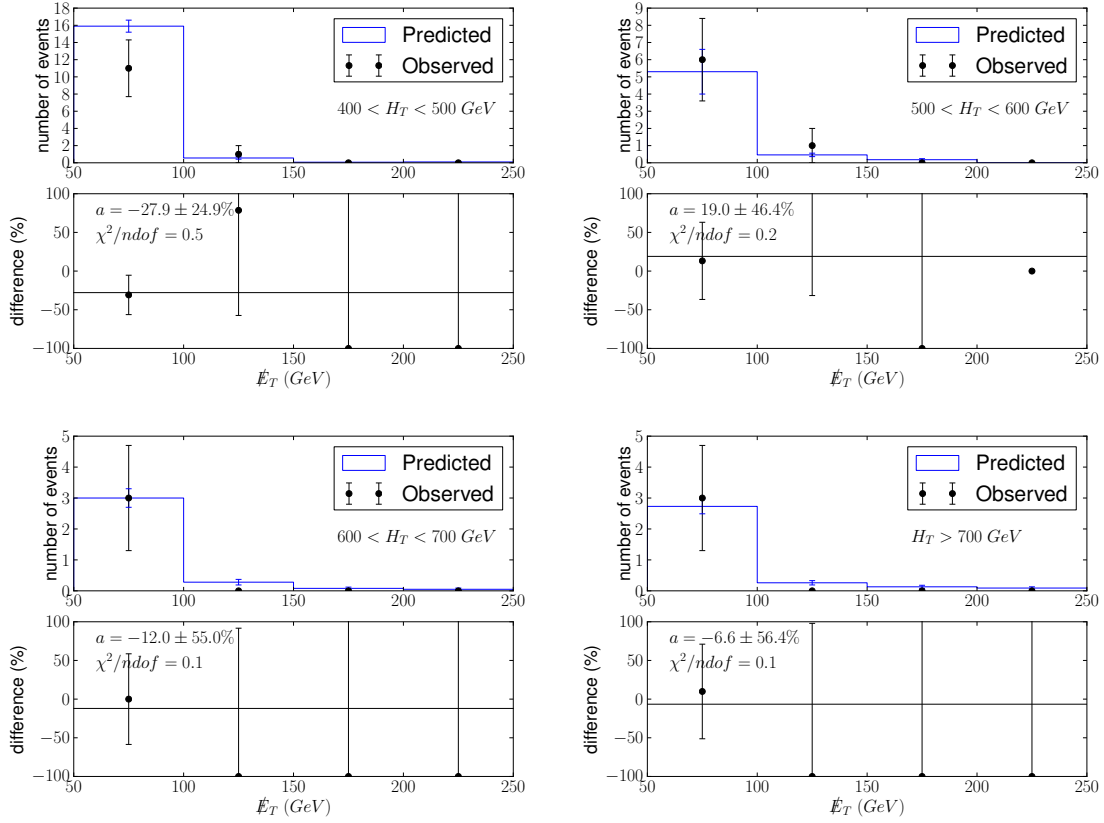
Figure 5.4: The estimated $\not{E}_T$ distribution of isolated events using the non-isolated events in the sideband region compared to the true $\not{E}_T$ distribution of the isolated events in the sideband region in bins of H_T. The percentage difference between the estimated and observed number of events is plotted and a flat line is fitted.

compared to an observation of 0. The prediction is consistent with the observed number of events.

Now that background estimation procedure has been shown to work using the MC and using the sideband region, it can be used on the data to make the background estimation for this search. Figure 5.5 shows the $\not{E}_T$ distribution of the background estimation in bins of H_T. The important number for this search is the estimated number of background events in the ($H_T > 700\,\text{GeV}$, $\not{E}_T > 200\,\text{GeV}$) bin because that is the most significant bin in terms of the limit placed on the GMSB cross-section. The estimated number of backgound events in this bin along with its statistical uncertainty is 7.7 ± 2.1.
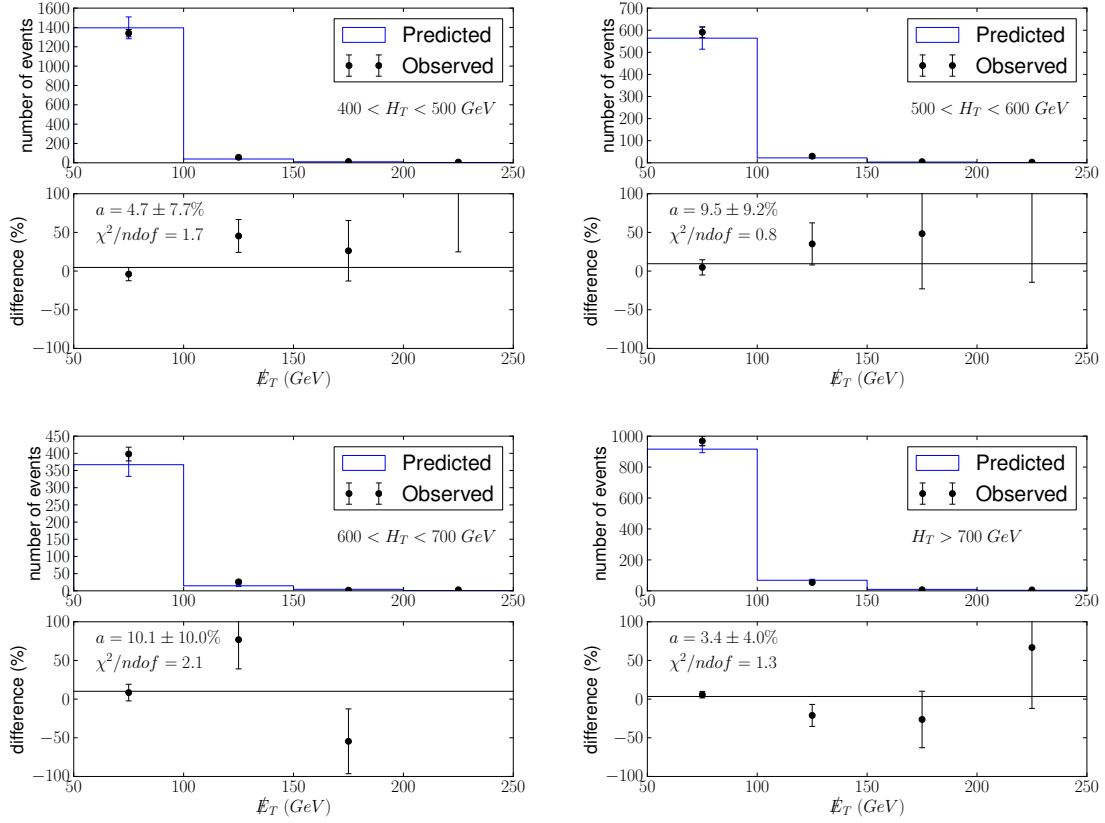
Figure 5.5: The estimated $\displaystyle{\not}E_T$ distribution of background using the control sample compared to the observed $\displaystyle{\not}E_T$ distribution of the selected events in bins of H_T. The percentage difference between the estimated and observed number of events is plotted and a flat line is fitted.

The systematic uncertainty on the background estimation comes from the assumption that the control sample accurately estimates the number of selected events. Due to the small number of events in the sideband region, the MC alone is used to determine the systematic uncertainty. The uncertainty is taken to be the magnitude of the difference between the estimation and the truth in the MC, σ_δ, added in quadrature to the statistical uncertainty on the knowledge of that value, σ_{stat} (Equation 5.1).

$$\sigma_{total} = \sqrt{\sigma_\delta^2 + \sigma_{stat}^2} \tag{5.1}$$

The value of σ_δ is 29 % and the value of σ_{stat} is 25 %. Thus the total systematic uncertainty on the background estimation is 38 %. The estimate of the number of background events including statistical and systematic uncertainties is $7.7 \pm 2.1(stat.) \pm 2.7(syst.)$.

5.3 Electroweak and $t\bar{t}$ Backgrounds

The Electroweak background is small in comparison to the QCD background. Electroweak processes can contribute real $\not{E}_T$ through the neutrino which is not detected. The cross section of electroweak processes is much lower than that of QCD and this rules out any background due to fakes from jets. There are two possible sources of photons: $W \rightarrow e\nu$ where the electron has been misidentied as a photon or W/Z with ISR/FSR.

The $W \rightarrow e\nu$ background is estimated using the MC and by measuring the electron/photon misidentification rate in data. The misidentification rate is measured using $e\gamma$ and ee events from data where the electron is selected using the same selection criteria as the photon (the only difference is that the electron has a track). For each sample a function is fitted to the invariant mass peak to determine the number of $Z \rightarrow ee$ events. The electron/photon misidentification rate is the number of Z events in the $e\gamma$ sample compared to the number of Z events in the ee sample. The misidentification rate is found to be 0.014 ± 0.004 [12]. This agrees well with the value from MC: 0.012 ± 0.002. The total number of $W \rightarrow e\nu$ events passing the selection is $0.52 \pm 0.10(stat.)$. The W/Z+γ background is estimated to be 0.030 ± 0.030 from the MC. A conservative estimate of the systematic uncertainty of 100 % is made to cover the jet energy scale, jet energy resolution, cross-section and luminosity uncertainties.

The $t\bar{t}$ background also has real $\not{E}_T$, but it is negligible due to the low cross-section. The $t\bar{t}$ background is estimated using Monte Carlo to be 0.007 ± 0.007, where again a systematic uncertainty of 100 % is used as conservative estimate.

Ignoring the $W/Z + \gamma$ and $t\bar{t}$ backgrounds because they are so small, the total electroweak background is 0.5 ± 0.5 events.

5.4 Conclusions

The background from QCD processes in the only significant bin ($H_T > 700\,\mathrm{GeV}$, $\not{E}_T > 200\,\mathrm{GeV}$) is estimated to be $7.2 \pm 2.1(stat.) \pm 2.9(syst.)$ events. The background from electroweak processes is estimated to be 0.5 ± 0.5 events.

Chapter 6

Signal Prediction and Systematics

6.1 Introduction

The predicted number of signal events, s, is given by Equation 6.1.

$$s = \epsilon \sigma L \qquad (6.1)$$

where ϵ is the efficiency $\times$ acceptance for the event selection, σ is the cross section and L is the integrated luminosity.

The signal cross section comes from theoretical calculations. A total of 441 different signal models are considered with different values for squark mass and gluino mass. The squark mass and gluino mass each take 21 values from $400\,\mathrm{GeV}$ to $2000\,\mathrm{GeV}$ in intervals of $80\,\mathrm{GeV}$. The cross section is $\sim 0.01\,\mathrm{pb}$ in the region close to exclusion depending on the squark and gluino masses. The largest uncertainty in the signal prediction comes from the cross section ($\sim 20\,\%$).

The integrated luminosity comes from LHC measurements of the beam. $1.1\ \mathrm{fb}^{-1}$ of data is used in this analysis. The uncertainty on the integrated luminosity is about $5\,\%$.

The efficiency $\times$ acceptance for the signal is found by applying the selection cuts to the signal MC. Corrections need to be made relating to the difference between the photon efficiency in data and MC and to account for pile-up. In addition to these corrections uncertainties on the signal prediction need to be determined. These include statistical

errors and systematic errors. Since 10,000 events were used for each signal point, the statistical error is small and so it is the systematic error on which attention must be focussed.

Cuts are made on jets, photons, H_T and $\not{E}_T$. The major sources of uncertainty for the jet and H_T cuts are the jet energy scale and jet energy resolution. For the photons the main sources of uncertainty come from the photon efficiency correction and from pile-up which affects the photon isolation efficiency. Both the H_T and $\not{E}_T$ distributions are also affected by pile-up, but this is a small effect.

The numbers and plots relating to the systematic uncertainties presented in this section use a signal parameter point close to the exclusion limit with squark mass 1200 GeV and gluino mass 1200 GeV. The systematic uncertainties are also determined for all the other parameter points in the same way.

6.2   Photon Efficiency Correction

The photon efficiency needs to be determined to calculate the signal efficiency. The photon efficiency could be found using the MC, but that relies heavily on the correct modelling of the shower shape, isolation and other variables which may not be well modelled in the MC. The photon efficiency is measured from data. In the absence of a suitable pure photon sample in the data, electrons from $Z \to ee$ events are used. This relies on the similarity in detector response between electrons and photons. A scale factor to correct the MC photon efficiency to the real photon efficiency in data is obtained using the electrons (Equation 6.2).

$$\epsilon_\gamma^{data} = \frac{\epsilon_e^{data}}{\epsilon_e^{MC}} \times \epsilon_\gamma^{MC} \tag{6.2}$$

Where:

- ϵ_γ^{data} = photon efficiency in data;

- ϵ_γ^{MC} = photon efficiency in MC;

- ϵ_e^{data} = electron efficiency obtained using $Z \to ee$ events in data that satisfy the photon selection;
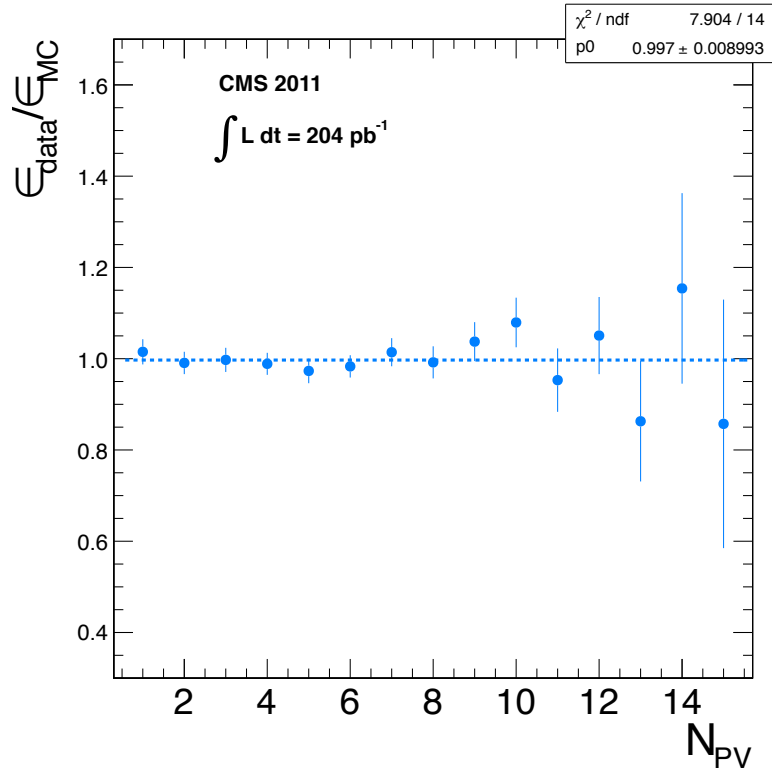
Figure 6.1: The efficiency correction between data and MC as a function of the number of primary vertices.

- ϵ_e^{MC} = electron efficiency obtained using $Z \to ee$ events in MC that satisfy the photon selection.

The selection criteria for electrons are the same as those for photons except that electrons have a track. The distribution in photon or electron identification variables is similar for isolated photons and electrons. Using $Z \to ee$ events in data, the tag-and-probe method is used to find the electron efficiency. One electron (tag) is selected with stringent criteria to be sure that it is an electron. Another electron (probe) with looser requirements is located such that the invariant mass of the two electrons lies in the Z peak.

Figure 6.1 shows the variation of the efficiency correction as a function of the number of reconstructed primary vertices. The MC photon efficiency is $\epsilon_\gamma^{MC} = 0.824 \pm 0.003$ and the scale factor is found to be $\epsilon_e^{data}/\epsilon_e^{MC} = 0.953 \pm 0.014(stat.)$. Two possible sources of systematic uncertainty on this number were considered:

Electrons and photons behave differently in MC: Both electrons and photons give EM showers in the ECAL and the selection cuts have been chosen to be similarly efficient for electrons and photons. However, one can imagine that there may be a slight difference between the two e.g. because of bremsstrahlung. To check this effect the MC electron efficiency from $Z \to ee$ events was compared with the MC photon efficiency from γ+jet events. Half the difference between the two results, $0.5\,\%$, was taken as a systematic error on the scale factor.

Pile-up: The MC may not accurately model the data in a high pile-up environment. To estimate the size of this effect the scale factor was calculated for events with fewer than 5 primary vertices and events with at least 5 primary vertices. The number 5 was chosen because that is approximately where the distribution of primary vertices in the data peaks. The difference between the scale factors in the two samples, 0.024, was taken as a systematic error on the scale factor.

Combining the systematic errors above with the statistical error yields a final data-MC efficiency scale factor of $\epsilon_e^{data}/\epsilon_e^{MC} = 0.953 \pm 0.038$. This uncertainty on the scale factor translates into an uncertainty of 3.8% on the signal prediction.

6.3   Jet Energy Scale

Jets are reconstructed from energy deposits in the calorimeters. p_T and η dependent jet energy corrections are applied to the raw calorimeter energy to get the jet energy. Any variation in these corrections would change the jet p_T, the H_T and the $\not{E}_T$.

The appropriate jet energy corrections are determined from γ+jet events in data. The photon is used as a reference object because its energy is well measured by the ECAL. The response $\frac{p_T^{jet}}{p_T^{\gamma}}$ is measured in bins of jet p_T and η to get the jet energy corrections. Details of the procedure to determine the jet energy corrections and their uncertainties are given in [11]. Figure 6.2 shows the jet energy correction factors as a function of jet p_T for jets with $|\eta| = 1.0$ and as a function of η for jets with $p_T = 200\,\text{GeV}$.
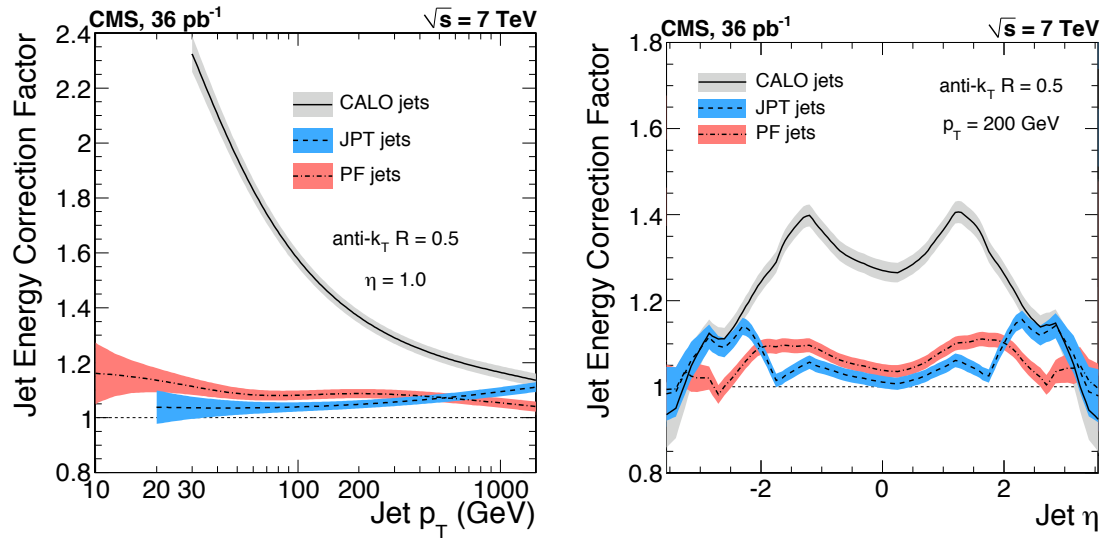
Figure 6.2: The jet energy correction factor as a function of p_T with $\eta = 1.0$ (left) and as a function of η with $p_T = 200\,\text{GeV}$ (right). Three diferent jet reconstructions are shown: CALO, JPT and PF. PF jets are used in this analysis. The bands indicate the corresponding uncertainties. Reproduced from [11]

The uncertainty is $\sim 3\,\%$ on jets above $50\,\text{GeV}$ and $\sim 5\,\%$ on smaller jets and unclustered energy. Figure 6.3 shows the jet energy scale uncertainty against jet p_T for central jets and Figure 6.4 shows the jet energy scale uncertainty against jet η for $100\,\text{GeV}$ jets.

In order to evaluate the effect of the jet energy scale uncertainty on the signal efficiency $\times$ acceptance, the p_T of all the jets is modified upward and downward according to the jet energy uncertainties before applying the event selection. The $\not{E}_T$ can be expressed as Equation 6.3.

$$\not{E}_T = -\Sigma \, \text{jets} - \text{photon} - \text{unclustered energy} \qquad (6.3)$$

The $\not{E}_T$ is modified to take account of the jet energy correction uncertainties by the following procedure:

- Add the photon to the $\not{E}_T$ (i.e. remove it from consideration).

- Add the jets also to get the unclustered energy.

- Modify the unclustered energy up and down by $5\,\%$ in a correlated way with the jet energy correction uncertainties.

88
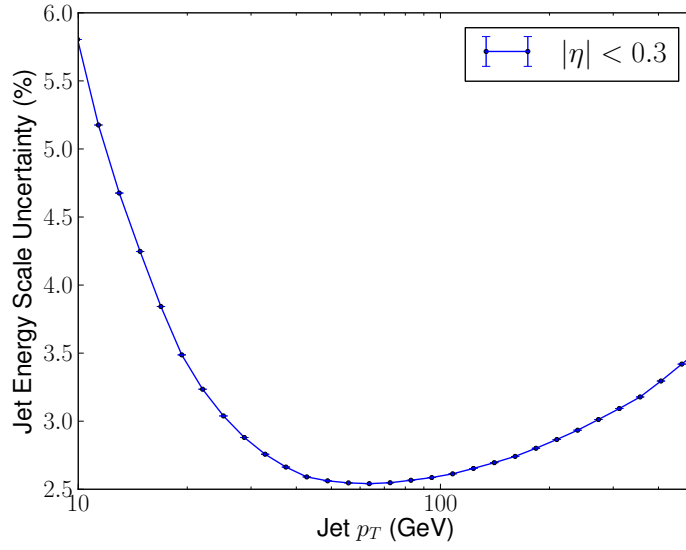
Figure 6.3: The jet energy scale uncertainty as a function of p_T for central jets ($|\eta| < 0.3$).
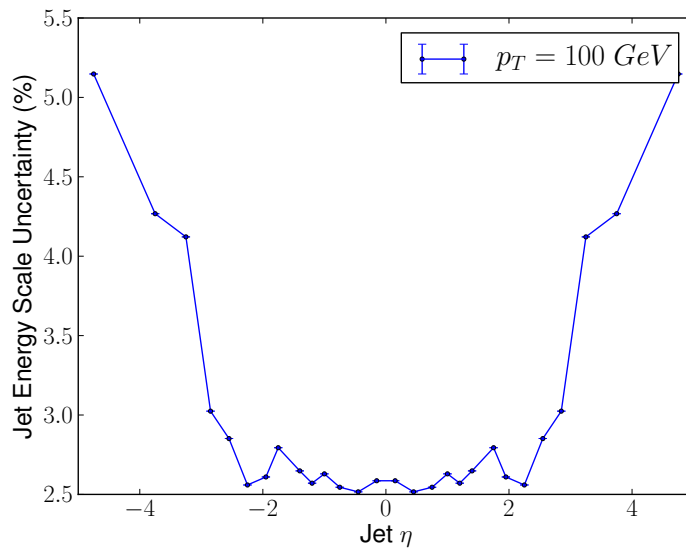
Figure 6.4: The jet energy scale uncertainty as a function of η for 100 GeV jets.
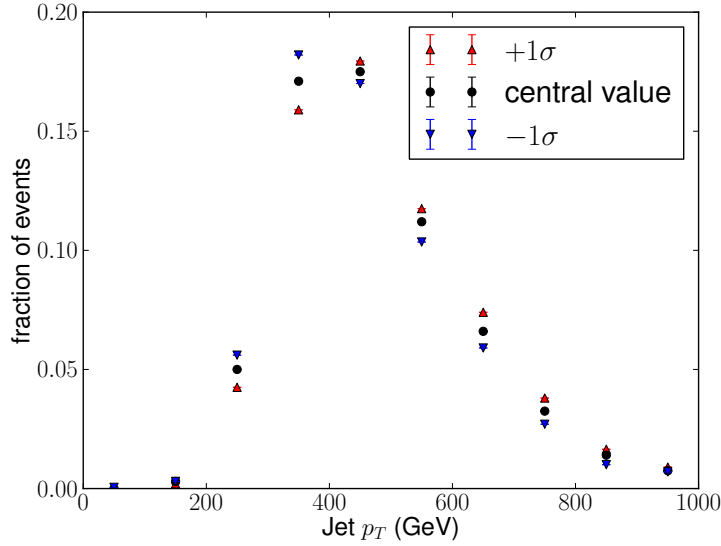
Figure 6.5: The leading jet p_T distribution in signal events with a one sigma upward variation (red) and one sigma downward variation (blue) in jet energy scale.

- Subtract the jets scaled both up and down according to the jet energy correction uncertainties.

- Subtract the photon to get the modified $\not{E}_T$.

Figure 6.5 shows the leading jet p_T distribution with a one sigma upward variation and a one sigma downward variation in jet energy scale. Figure 6.6 shows how the variation in jet energy scale affects the $\not{E}_T$ and H_T distributions.

The variation in signal efficiency $\times$ acceptance resulting from the $\pm 1\sigma$ variations of the jet energy scale on the jet p_T, $\not{E}_T$ and H_T is extracted. The value of ϵ varies about its nominal value, 0.382, by 0.017 when the jet energy scale is varied within its uncertainty. This means the uncertainty on the signal efficiency $\times$ acceptance from the jet energy scale is 4.4 %.

6.4   Jet p_T Resolution

The jet p_T resolution is determined using two different methods:
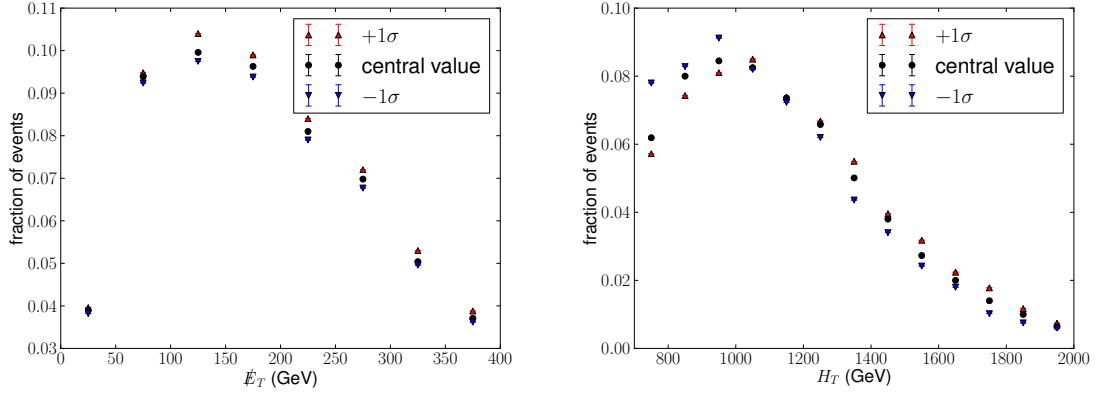
Figure 6.6: The $\not{E}_T$ distribution (left) and H_T distribution (right) in signal events with a one sigma upward variaton (red) and one sigma downward variation (blue) in jet energy scale.

- **Di-jet asymmetry:** This method uses balanced di-jet events which are abundant in data and considers p_T conservation. An asymmetry variable is constructed from the p_T of the two jets:

$$A = \frac{p_T^1 - p_T^2}{p_T^1 + p_T^2} \tag{6.4}$$

The variance of the asymmetry variable can be expressed as:

$$\sigma_A^2 = \left(\frac{\partial A}{\partial p_T^1}\right)^2 \sigma_{p_T^1}^2 + \left(\frac{\partial A}{\partial p_T^2}\right)^2 \sigma_{p_T^2}^2 \tag{6.5}$$

For jets which lie in the same η bin and the same p_T bin, the p_T's are the same and the resolutions are the same so there is an expression for the fractional p_T resolution in terms of the variance in the asymmetry which can be measured in the data:

$$\frac{\sigma_{p_T}}{p_T} = \sqrt{2}\sigma_A \tag{6.6}$$

- **γ/Z+jet balance:** This method uses γ+jet or Z+jet events from data and uses the γ or Z as a well measured reference object to which the jet p_T can be compared. In balanced events the γ/Z has the same p_T as the jet. The variation of the ratio, R, of the jet p_T relative to the γ/Z p_T in bins of γ/Z p_T gives the jet p_T resolution.

$$R = \frac{p_T^{jet}}{p_T^{\gamma/Z}} \tag{6.7}$$

Further details on the jet p_T resolution measurement and determination of the associated uncertainty can be found in [11]. The jet p_T resolution as a function of jet p_T and for
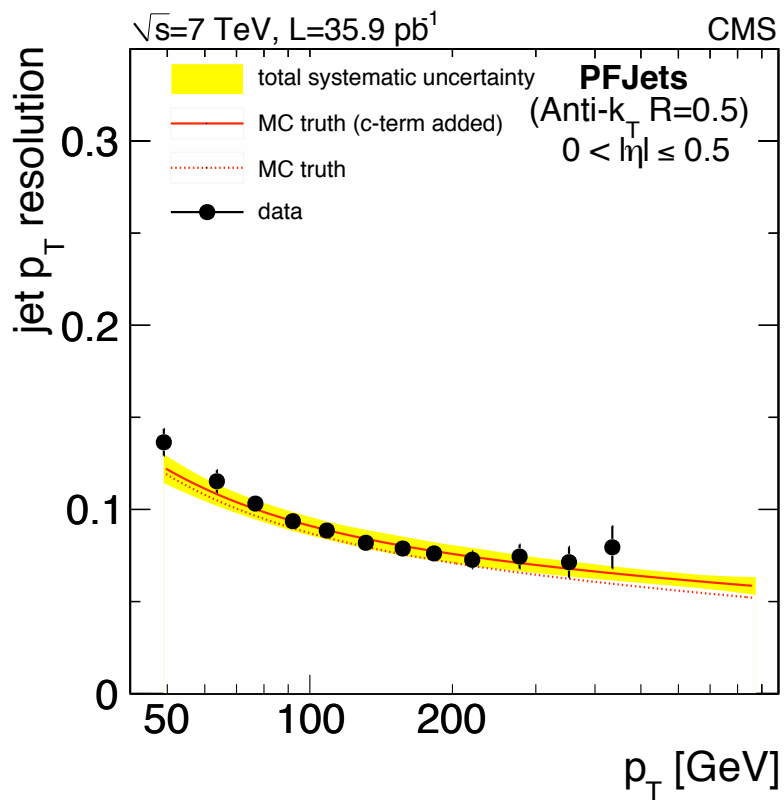
Figure 6.7: The jet p_T resolution measured from data for jets with $|\eta| < 0.5$ (black points) compared to MC (red line). The yellow band gives the systematic uncertainty. Reproduced from [11].
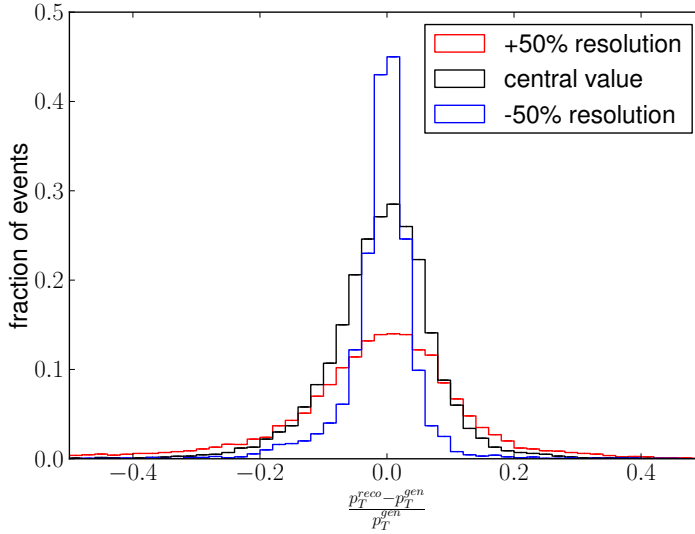
Figure 6.8: The jet p_T resolution compared to generator level jets (grey) and the same distribution after an upward (red) and downward (blue) variation of 50 % in the jet p_T resolution.

$|\eta| < 0.5$ is shown in Figure 6.7. The figure also shows that MC agrees well with the data as far as jet energy resolution is concerned. For the SUSY events the "true" jet energy comes from matching the reconstructed jets to the generator level in the MC. The jet energy resolution is determined by comparing the reconstructed jet energy with the generator level jet energy. This gives a jet p_T resolution similar to that measured in [11].

The resolution is varied upward and downward by 50 %, which correspond to the uncertainty on the forward jets but is conservative for the central jets. Figure 6.8 shows the jet energy resolution with an upward and a downward variation.

Figure 6.9 shows the effect of the variation in resolution on the H_T and $\not{E}_T$ distributions. The important result is how the variation in jet energy resolution affects the signal efficiency. The signal efficiency is 0.382 ± 0.005 when the jet energy resolution is varied within its uncertainty. This means the uncertainty on the signal efficiency from the jet energy resolution is 1.2 %.
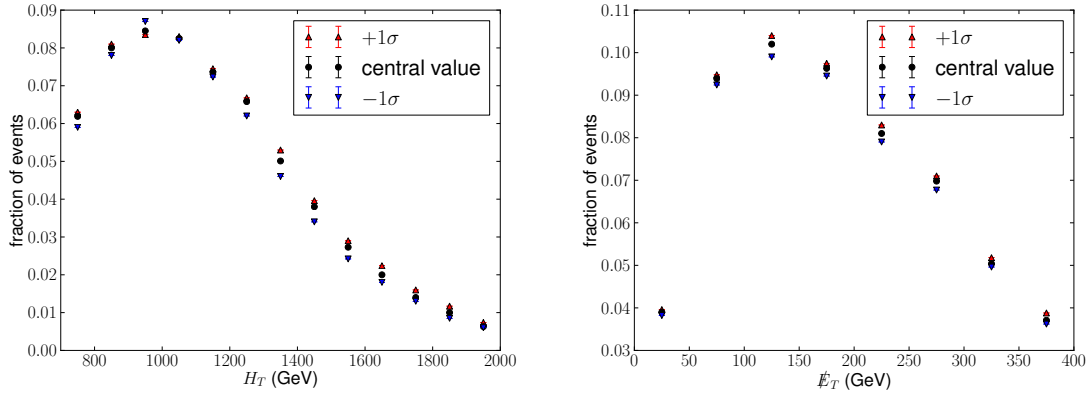
Figure 6.9: The effect of an upward (red) and a downward (blue) variation of the jet p_T resolution on the H_T and $\not{E}_T$ distributions.

6.5 Pile-up

Pile-up is where there are multiple interations per bunch crossing. Pile-up affects the number of signal events in several ways:

- The H_T increases due to jets and underlying event activity from other interactions in the same bunch crossing.

- The $\not{E}_T$ distribution is broadened by the introduction of more jets and underlying event activity.

- The photon isolation efficiency is reduced since there is more surrounding activity which can populate the isolation cone.

Most of the pile-up events are soft with, at most, low p_T jets and do not contribute much to H_T. Since the signal MC does not have pile-up simulated, the effect of pile-up on the H_T is evaluated by looking at the H_T distribution in MC QCD events with and without pile-up. A shift of 6.8 ± 0.8 is applied to the no pile-up H_T distribution to match the pile-up H_T distribution (Figure 6.10). With a $\pm 1\sigma$ variation in the H_T shift the signal efficiency is 0.3821 ± 0.0003, an uncertainty of 0.1%.

The $\not{E}_T$ distribution is broadened by the introduction of more jets and underlying event activity from other interactions in the same bunch crossing. The pile-up events will mostly be low H_T and balanced so will have only a little effect on the $\not{E}_T$. The $\not{E}_T$ distribution
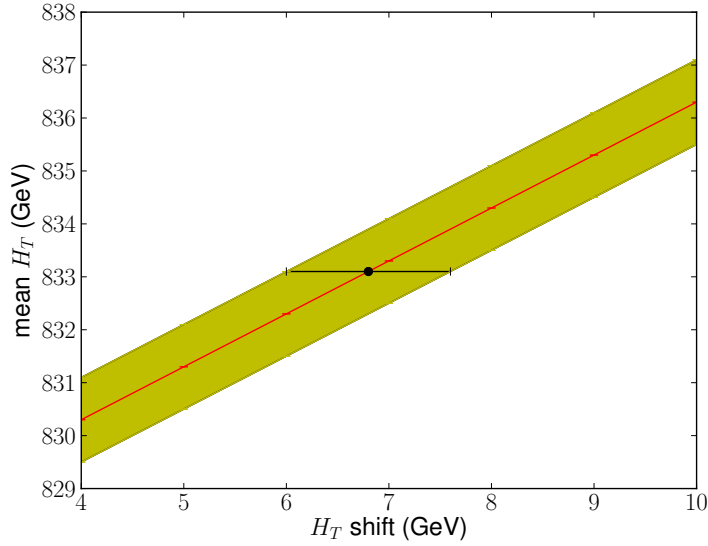
Figure 6.10: The mean H_T as a function of H_T shift (red) with one sigma band (yellow) in QCD events with a similar H_T to the signal. The mean H_T with pile-up is shown in black.

is smeared to account for pile-up. To determine the amount of smearing necessary a QCD sample with similar H_T and no pile-up is smeared until the shape agrees with the $\not{E}_T$ distribution with pile-up. Figure 6.11 shows the average $\not{E}_T$ in QCD events without pile-up as a function of the $\not{E}_T$ smearing. From the plot a $\not{E}_T$ smearing of 3.5 ± 0.5 GeV is applied to account for pile-up. The important number is the uncertainty in the signal efficiency due to the uncertainty in the $\not{E}_T$ smearing to account for pile-up, which is found to be 0.3821 ± 0.0004. This corresponds to an uncertainty of 0.1%.

The photon isolation efficiency is particularly affected by pile-up because activity from other events in the same bunch crossing can populate the isolation cone. To quantify this effect QCD MC events with a similar H_T were used to determine the photon efficiency in MC as a function of the number of primary vertices. Figure 6.12 shows the photon efficiency as a function of the number of primary vertices. The efficiency is shown relative to the efficiency when there is only a single reconstructed primary vertex. Taking the distribution of number of primary vertices from data, the efficiency expected in the presence of pile-up can be calculated. This method assumes that photons in SUSY events have a
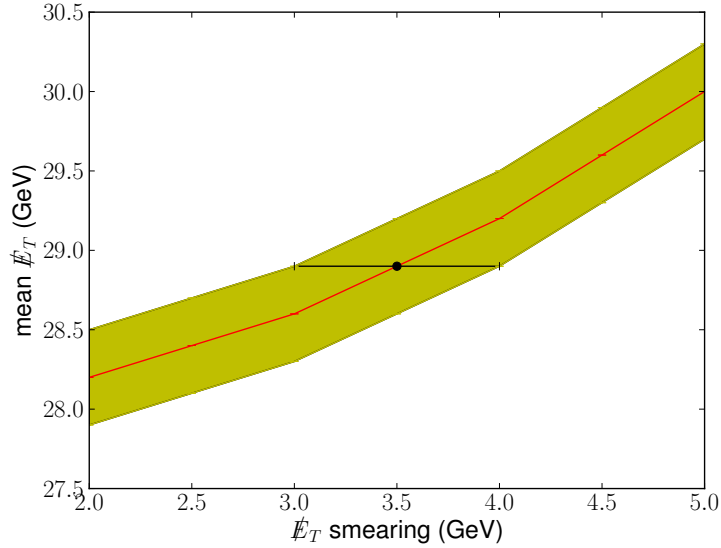
Figure 6.11: The mean $\not{E}_T$ as a function of $\not{E}_T$ smearing (red) with one sigma band (yellow) in QCD events with a similar H_T to the signal. The mean $\not{E}_T$ with pile-up is shown in black.

similar behaviour in the presence of pile-up to photons in QCD events. This assumption is reasonable beacause the pile-up affects mainly the isolation through extra surrounding activity which is a property of the event rather than the photon. This method also relies on MC modelling the photon efficiency in pile-up well. This can be checked by looking at $Z \rightarrow ee$ events in data. The efficiency requires only a small correction between data and MC which is relatively stable with respect to the number of reconstructed primary vertices (Figure 6.1). The photon efficiency correction due to pile-up is 0.83 ± 0.01. This produces an uncertainty of $2.6\,\%$ on the signal efficiency *times* acceptance.

6.6 Signal Cross-Section

To calculate the cross-section for $p + p \rightarrow X$, the parton collision $a + b \rightarrow X$ must first be considered (Figure 6.13). The cross-section for partons a and b with momentum fractions x_1 and x_2 is calculated. To get the cross-section from protons the PDFs must be folded in and the possible partons must be summed over as in Equation 6.8.
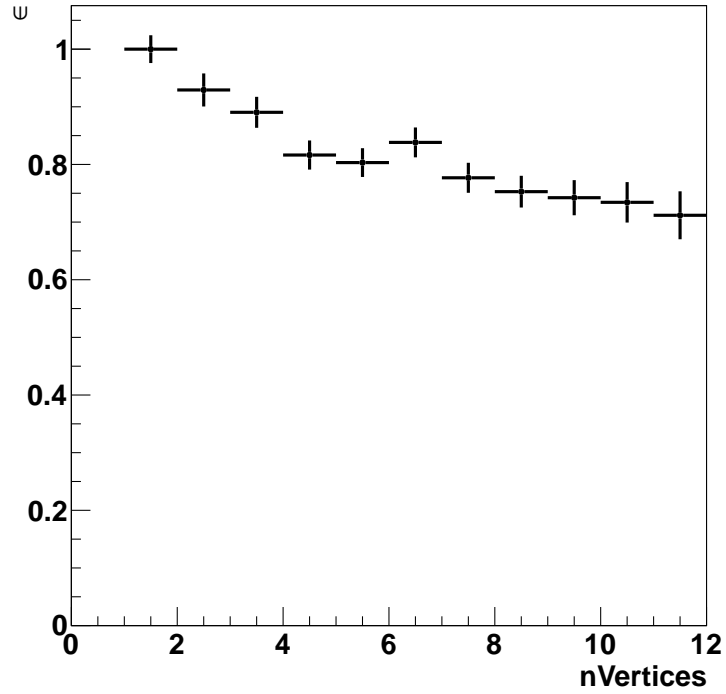
Figure 6.12: The photon efficiency as a function of the number of primary vertices relative to the photon efficiency with only one primary vertex.
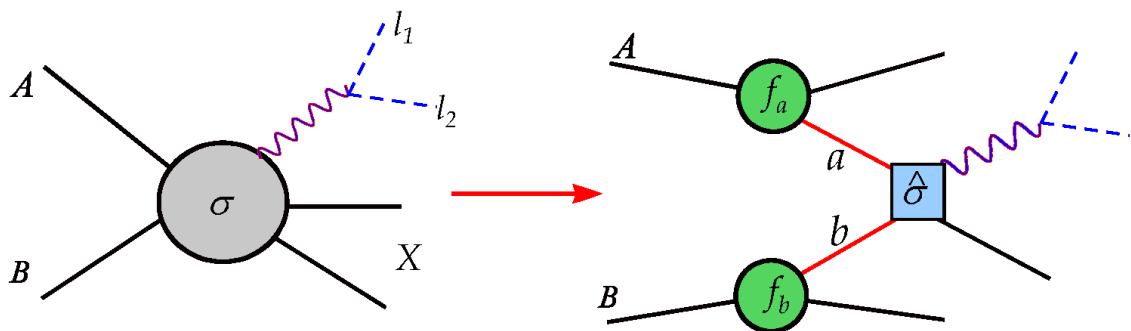
Figure 6.13: In proton collisions the cross-section must be factorised into the individual parton cross-sections.
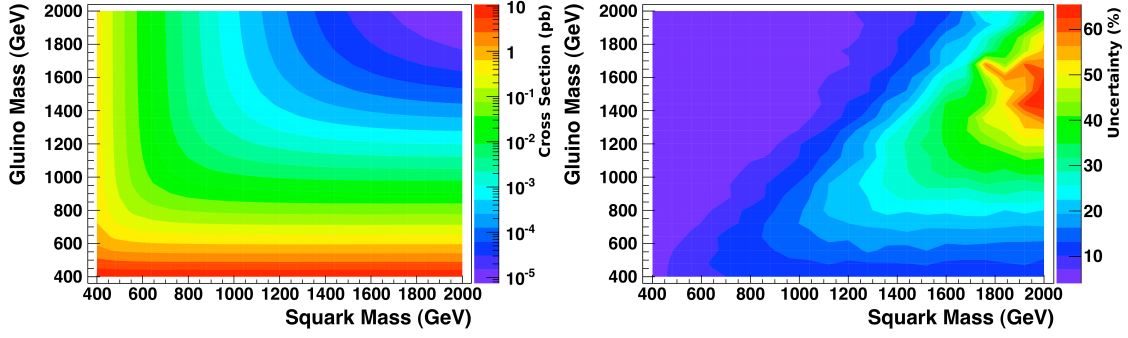
Figure 6.14: The cross-section (left) and total percentage uncertainty (right) for each parameter point in the mSquark vs mGluino plane. Reproduced from [12].

$$\sigma(s) = \sum_{a,b} \int_0^1 dx_1 \int_0^1 dx_2 f_a(x_1, Q^2) f_b(x_2, Q^2) \sigma_{ab}(\hat{s}) \tag{6.8}$$

The cross-section for the parton process $a + b \to X$ is an infinite sum over terms corresponding to processes with extra Feynman diagram vertices and radiations as in Equation 6.9. The terms get smaller as more vertices are introduced. To do the calculation the series must be cut off at some order. Here the series is cut off at Next to Leading Order (NLO).

$$\sigma = \sigma_0 + \sigma_1 + ... \tag{6.9}$$

Thus there are two major sources of uncertainty on the signal cross-section:

- The uncertainties on the PDFs, $f_a(x, Q^2)$ and $f_b(x, Q^2)$ above.

- The uncertainty from higher order terms.

Figure 6.14 shows the cross-section and total percentage uncertainty for each parameter point in the mSquark vs mGluino plane.

6.7 Integrated Luminosity

The luminosity is calculated using the HF and normalised by van der Meer scans of the beam profile [64]. The integrated luminosity can be written as:

98

$$L = \frac{\mu n_b f}{\sigma_{eff}} \tag{6.10}$$

where:

- μ is the mean number of interactions per bunch crossing;

- n_b is the number of bunches;

- f is the revolution frequency of the bunches;

- σ_{eff} is the effective cross-section of the selection.

The number of bunches and the revolution frequency are known precisely. The mean number of interactions per bunch crossing is determined from the fraction of empty towers in the HF. A relative value for the effective cross-section is found from the linear relationship between tower E_T and luminosity.

The normalisation of the luminosity measurement is done using van der Meer scans of the transverse beam profile [65]. The size and shape of the interaction region is measured as a function of transverse beam separation. With a proton density of $F(x,y) = f_x(x)f_y(y)$ and N protons per bunch, the absolute luminosity can be written as:

$$L = \frac{N^2 f n_b F(0,0)}{\int f_{x'} dx' \int f_{y'} dy'} \tag{6.11}$$

Assuming a gaussian transverse beam profile, the denominator can be calculated as $4\pi\sigma_x\sigma_y$, where σ_x and σ_y are extracted from gaussian fits to the transverse beam profile.

The dominant uncertainty on the luminosity measurement comes from the beam current measurement (3.1 %). The total uncertainty on the integrated luminosity measurement is 5 %.

6.8 Summary of Systematics

Table 6.1 shows a summary of all the systematic uncertainties for the backgrounds and the signal. These are the uncertainties on the number of events in the ($H_T > 700\,\text{GeV}$, $\not{E}_T > 200\,\text{GeV}$) bin.

Source of Systematic Uncertainty	Uncertainty
Background Estimation	38 %
Photon Efficiency	3.8 %
Jet Energy Scale	4.4 %
Jet Energy Resolution	1.2 %
Pile-up: HT shift	0.1 %
Pile-up: MET smearing	0.1 %
Pile-up: photon efficiency	2.4 %
Signal Cross-Section	20 %
Integrated Luminosity	5 %
Total signal uncertainty	22 %

Table 6.1: A summary of the systematic uncertainties and how they affect the expected number of events in the signal and the background.

Chapter 7

Limit Setting and Results

7.1 Introduction

Once the event selection and background estimation procedure have been defined and the data has been collected one needs to determine the limit on the cross section of a possible SUSY signal (according to a specific model) or, if a discovery has been made, the significance of that discovery. In the present case no discovery has been made so a limit on the cross section must be found. There are various statistical procedures for doing this and no consensus on the best method. Here the CLs method is used [18, 66, 67, 68]. The CLs method is widely used in the field of particle physics. The results are interpreted as an exclusion in the squark mass vs gluino mass plane.

A likelihood function must be defined. The likelihood is the probability of the data being observed given a model. The CLs method encompasses the statistical uncertainties on the expected number of events as well as the systematic uncertainties associated with the background estimation and signal prediction (e.g. luminosity measurement and jet energy scale uncertainty). Parameters in the likelihood include the parameter of interest on which we wish to set a limit – the amount of signal in this case – in addition to nuisance parameters associated with the systematic uncertainties.

The goal is to find a confidence interval for the parameter of interest based on the likelihood. This gives an upper limit on the size of a possible SUSY signal at a given confidence level. An exclusion plot with the expected limit and the observed limit is given for the

GMSB models considered here in squark mass vs gluino mass parameter space. The exclusion plot for another CMS analysis of the same dataset looking at the same SUSY models is shown for comparison.

7.2   Likelihood Function

The likelihood function is the probability of observing the data given the model. There is a statistical component to the likelihood based on the number of events we can expect given a model prediction. The statistical component follows a poisson distribution. There are also systematic uncertainties based on how well the signal and background are predicted. These contribute a Gaussian component to the likelihood.

Let:

- b = Estimated number of background events;

- s = Number of expected signal events according to the model being tested;

- n = Number of events observed.

Considering only the statistical uncertainty on the expected number of events, which follows a Poisson distribution, the likelihood for the background only hypothesis is given by Equation 7.1.

$$L_b = p(n|b) = \frac{b^n e^{-b}}{n!} \tag{7.1}$$

And for the signal plus background hypothesis the likelihood is given by Equation 7.2.

$$L_{s+b} = p(n|s+b) = \frac{(s+b)^n e^{-(s+b)}}{n!} \tag{7.2}$$

The number of signal events can be written as:

$$s = f\epsilon\sigma L \tag{7.3}$$

This is the same as Equation 6.1 for the number of signal events, except that a signal strength factor, f, has been added. f is the parameter of interest on which we are seeking to set a limit. The likelihood for the signal plus background hypothesis can now be written as Equation 7.4.

$$L_{s+b}(f) = \frac{(f\epsilon\sigma L + b)^n e^{-(f\epsilon\sigma L+b)}}{n!} \tag{7.4}$$

Systematic uncertainties are introduced to the likelihood by allowing the parameters in the likelihood (b, ϵ, σ and L) to vary according the their uncertainties. These parameters are called nuisance parameters. To implement this, Gaussian terms are added to the likelihood with mean equal to the estimated value and sigma equal to the uncertainty. This allows them to vary away from their estimated value, but the Gaussian constrains them according to their uncertainty by paying a penalty in the likelihood. For example, the integrated luminosity was measured to be $1.100\pm0.044\,\text{fb}^{-1}$ so a Gaussian term with mean 1.100 and sigma 0.044 is added to the likelihood. Equation 7.5 shows the full likelihood function, including nuisance parameters.

$$
\begin{aligned}
L_{s+b}(f; \theta_b, \theta_\epsilon, \theta_\sigma, \theta_L) &= \frac{(\theta_\epsilon\theta_\sigma\theta_L + \theta_b)^n e^{-(\theta_\epsilon\theta_\sigma\theta_L+\theta_b)}}{n!} \\
&\cdot \frac{1}{\sqrt{2\pi}\sigma_b} e^{-\frac{1}{2}\left(\frac{\theta_b-b}{\sigma_b}\right)^2} \\
&\cdot \frac{1}{\sqrt{2\pi}\sigma_\epsilon} e^{-\frac{1}{2}\left(\frac{\theta_\epsilon-\epsilon}{\sigma_\epsilon}\right)^2} \\
&\cdot \frac{1}{\sqrt{2\pi}\sigma_\sigma} e^{-\frac{1}{2}\left(\frac{\theta_\sigma-\sigma}{\sigma_\sigma}\right)^2} \\
&\cdot \frac{1}{\sqrt{2\pi}\sigma_L} e^{-\frac{1}{2}\left(\frac{\theta_L-L}{\sigma_L}\right)^2}
\end{aligned}
\tag{7.5}
$$

The likelihood is used in the CLs method to find the upper limit on the parameter of interest, f.

7.3 CLs

The CLs method is used to determine the confidence interval for the parameter of interest, f. The method is widely used within particle physics: it was used at the Tevatron for the Higgs limit [69] and at the LHC for the Higgs limit [70] and SUSY searches [71]. The CLs method profiles the nuisance parameters to incorporate systematic uncertainties in the limit.

The procedure for finding the confidence interval using CLs is:

- Construct a likelihood function. Equation 7.5 in this case.

- Construct a test statistic q_f for performing a hypothesis test. There are various possible choices for the this, here the profile likelihood ratio is used (Equation 7.6).

$$q_f = \frac{L_{s+b}(f; \hat{\boldsymbol{\theta}})}{L_b(0; \hat{\boldsymbol{\theta}})} \tag{7.6}$$

- Step through the possible values of the parameter of interest, f.

- Consider two hypotheses: the signal + background hypothesis and the background only hypothesis. For each hypothesis generate pseudo data according to the likelihood. Call the generated data "MC toys".

- Calculate the the p-values:

$$\begin{aligned} CLsb &= P(q_f \geq q_f^{obs} | \text{signal + background}) \tag{7.7} \\ CLb &= P(q_f \geq q_f^{obs} | \text{background only}) \tag{7.8} \end{aligned}$$

  These are the fraction of MC toys for which the test statistic is greater than the observed value given the signal + background hypothesis (Equation 7.7) and given the background hypothesis (Equation 7.8).

- Construct CLs as a ratio of p-values (Equation 7.9). This cannot be interpreted as a p-value itself. It gives an idea of how much more probable to observe the data given the signal + background hypothesis than the background only hypothesis.

$$CLs = \frac{CLsb}{CLb} \tag{7.9}$$

- Those values of f for which $CLs < \nu$ are excluded at a confidence level (CL) of $1 - \nu$. Here the CL is taken to be 95%. The upper limit on f at 95% CL is the value of f for which $CLs = 0.05$.

The CLs method is used to calculate the upper limit on f for each point in the parameter space. Figure 7.1 shows the upper limit on f in the squark mass vs gluino mass plane for the 441 points in the grid.

7.4 Interpolation and Smoothing

The grid of SUSY parameter points is rather coarse giving a jagged exclusion line. To make a smooth limit an interpolation is performed between the points on the grid to make
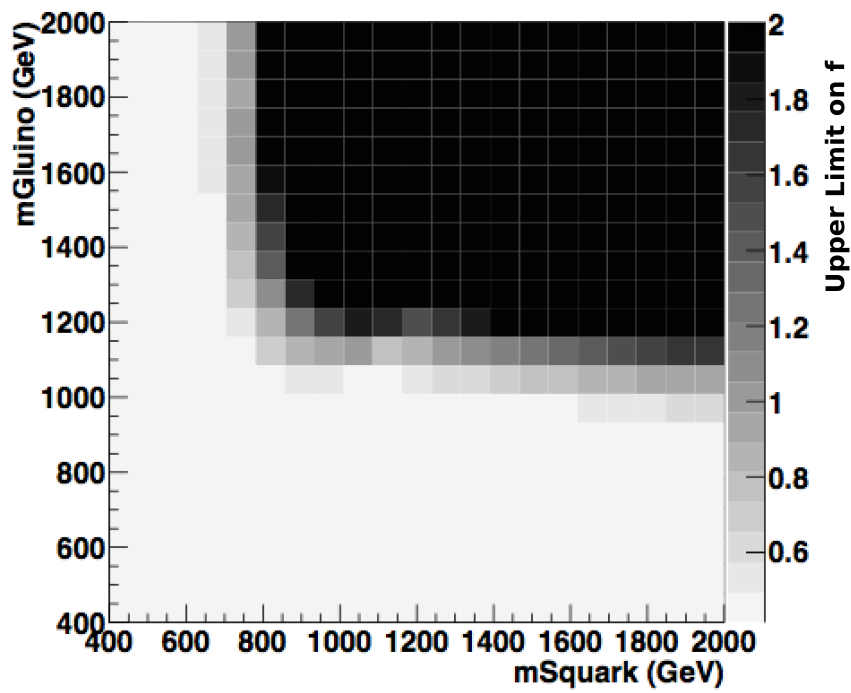
Figure 7.1: The expected upper limit on f in the squark mass vs gluino mass plane using the CLs method. Points with upper limit on f ¡ 1 are excluded at 95% confidence level.

Figure 7.2: The expected upper limit on f in the squark mass vs gluino mass plane after a linear interploation between the points. Points with upper limit on f < 1 are excluded at 95% confidence level.

a finer grid with more points in the parameter space. The upper limit on f is taken to vary linearly between points on the grid. Figure 7.2 shows the finer grid after linear interpolation between the points. The resulting exclusion line is still slightly jagged due to the finite number of points in the interpolation. To smooth the line each point along the line is replaced by a moving average which is the mean of the closest five points.

7.5 Expected and Observed Limit

An expected limit without looking at the data can be calculated. Pseudo data is generated using the background model. An expected limit is calculated using any of the above methods using the pseudo data as if it were data.

Many sets of pseudo data are generated and a limit on the cross section of a possible SUSY signal is calculated for each. An expected limit can be drawn on the SUSY parameter

space by linking those parameter points for which the signal can be excluded at 95% confidence level in half of the pseudo experiments. The 1σ band, a line linking the parameter points where the signal is excluded for 68% of the pseudo experiments, is also drawn.

Figure 7.3 shows the final limit plot at 95% CL with the expected limit, the ± 1 sigma band and the observed exclusion limit. The exclusion limit from another CMS analysis, RA3 [12], looking at the same signal model is also shown for comparison.

The limits on GMSB from previous experiments such as ALEPH [52], CDF [54] and D0 [53] are concerned with electroweak production rather than strong production. A direct comparison is difficult since the results are interpreted in a different parameter space, but these experiments have a much lower reach in terms of squark and gluino mass due to the lower $\sqrt{s}$.

The limit presented here is similar to the RA3 limit at high gluino mass, but excludes more parameter space at high squark mass (Figure 7.3). The RA3 search selects events using the $\gamma\gamma + \not{E}_T$ signature which is better in a cleaner environment with fewer jets, but worse in an environment with more jets because the photon efficieny is lower as a photon may be lost in a jet. Parameter points with high squark mass tend to have more jets.
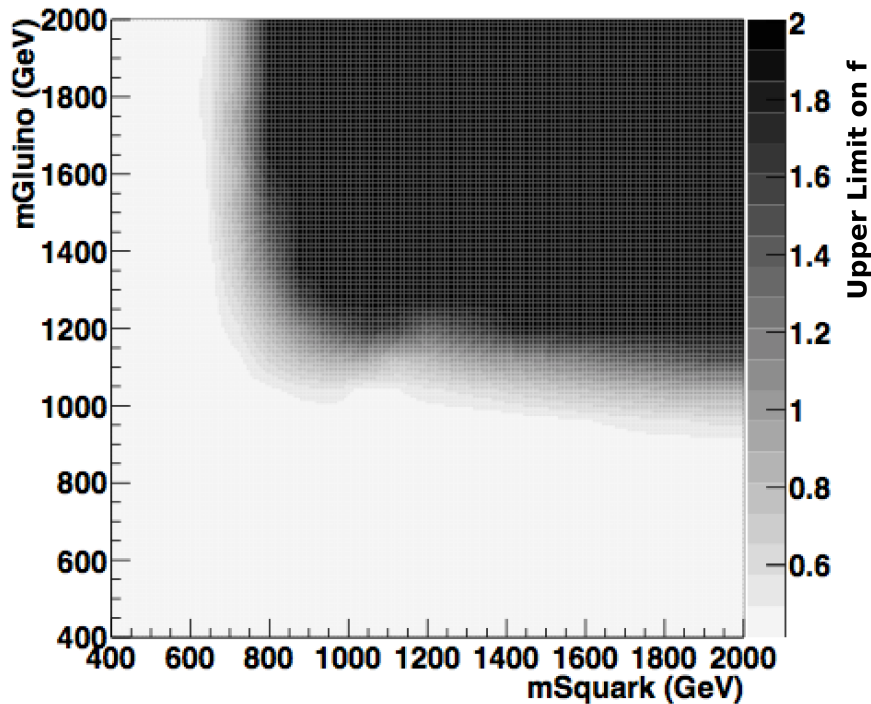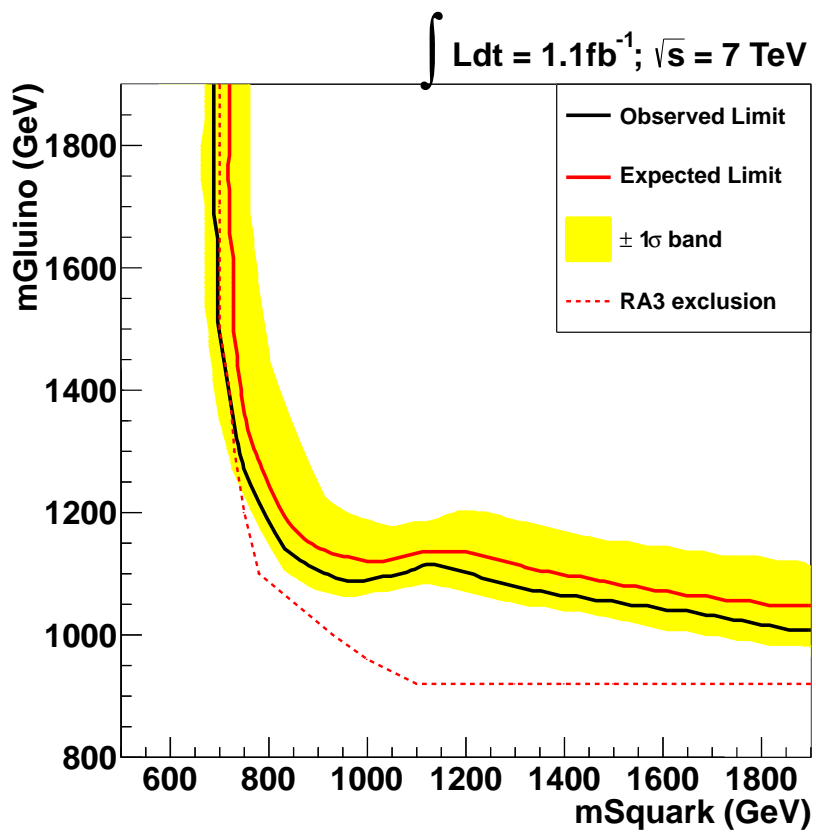
Figure 7.3: The expected upper limit on f in the squark mass vs gluino mass plane after a liner interploation between the points.

Chapter 8

Conclusions

A limit has been placed on the GMSB cross-section using $1.1\,\text{fb}^{-1}$ of proton-proton colli-
sions data at $\sqrt{s} = 7\,\text{TeV}$ from the CMS detector. The event selection was based on the
signature: $\gamma + \text{jets} + \not{E}_T$. Variables H_T and $\not{E}_T$, which indicate the energy scale of the
event and the missing transverse energy of the event respectively, were used to search for
GMSB. The background from QCD processes was estimated using a control sample from
data in which the isolation cut on the photons was inverted. The negligible electroweak
background was estimated using Monte Carlo simulation. A grid of signal samples in
squark mass versus gluino mass parameter space was available. The signal efficiency for
each parameter point was estimated using the MC samples. Systematic uncertainties due
to the jet energy scale, jet energy resolution, photon efficiency and pile-up were considered.
The signal efficiencies were multiplied by the signal cross-section and integrated luminos-
ity to get the predicted number of signal events. With an observed number of events, a
background estimation and a signal prediction, the CLs method was used to put a limit
on the GMSB relative cross-section in squark mass versus gluino mass parameter space.

Bibliography

[1] MissMJ, "Elementary Particle wikipedia page", Wikipedia (2006), `http://en.wikipedia.org/wiki/File:Standard_Model_of_Elementary_Particles.svg`.

[2] F. D. Aaron *et al.* (H1 and ZEUS Collaborations), "Combined Measurement and QCD Analysis of the Inclusive ep Scattering Cross Sections at HERA", JHEP **1**, 109 (2010).

[3] N. Foundation, "The Nobel Prize in Physics 2004", Nobelprize.org (2012), `http://www.nobelprize.org/nobel_prizes/physics/laureates/2004/`.

[4] S. Chatrchyan *et al.*, *CMS Physics Technical Design Report Volume 1: Detector Performance and Software* (CERN, 2006).

[5] S. Chatrchyan *et al.* (CMS Collaboration), "Tracking and Vertexing results from first collisions", (2010), CMS-PAS-TRK-10-001.

[6] S. Chatrchyan *et al.* (CMS Collaboration), "The CMS Experiment at the CERN LHC", JINST **3**, S08004 (2008).

[7] S. Chatrchyan *et al.* (CMS Collaboration), "Jet Performance in pp Collisions at 7 TeV", (2010), CMS-PAS-JME-10-003.

[8] S. Chatrchyan *et al.* (CMS Collaboration), "MET resolution vs. SumET in Minimum Bias 7 TeV events", (2010), CMS-AN-AN-10-142.

[9] WLCG, "Worldwide LHC Computing Grid", WLCG website (2012), `http://lcg.web.cern.ch/lcg/`.

[10] S. Chatrchyan *et al.* (CMS Collaboration), "Electromagnetic calorimeter commissioning and rst results with 7TeV data", (2010), CMS-NOTE-2010/012.

[11] S. Chatrchyan *et al.* (CMS Collaboration), "Determination of Jet Energy Calibration and Transverse Momentum Resolution in CMS", JINST **6**, P11002 (2010).

[12] S. Chatrchyan *et al.* (CMS Collaboration), "Search for General Gauge Mediated Supersymmetry with Two Photons and Missing Transverse Energy", Phys. Rev. Lett. **106**, 211802 (2011).

[13] T. S. Pettersson and P. Lefevre, "The Large Hadron Collider: conceptual design", (1995), CERN-AC-95-05 LHC.

[14] G. Aad *et al.* (ATLAS Collaboration), "The ATLAS Experiment at the CERN Large Hadron Collider", JINST **3**, S08003 (2008).

[15] P. Higgs, "Broken symmetries and the masses of gauge bosons", Phys. Rev. Lett. **13**, 508 (1964).

[16] S. P. Martin, "A Supersymmetry Primer", (2011), arXiv:hep-ph/9709356v6.

[17] N. Arkani-Hamed, S. Dimopoulos, and G. Dvali, "The Hierarchy Problem and New Dimensions at a Millimeter", Phys. Lett. B **429**, 263 (1998).

[18] K. Nakamura *et al.*, "Review of Particle Physics", J. Phys. G **37**, 075021 (2010), http://pdg.lbl.gov/.

[19] F. Halzen and A. D. Martin, *Quarks and Leptons: An Introductory Course in Modern Particle Physics*, 1st ed. (Wiley, 1984).

[20] D. Perkins, *Introduction to High Energy Physics*, fourth ed. (Cambridge University Press, 2000).

[21] D. Grifiths, *Introduction to Elementary Particles*, 2nd ed. (Wiley, 1987).

[22] P. A. M. Dirac, "The Quantum Theory of the Electron", Proc. R. Soc. Lond. A **117**, 610 (1928).

[23] R. P. Feynman, *QED: The strange theory of light and matter* (Princeton University Press, 1985).

[24] W. Lamb and R. Retherford, "Fine Structure of the Hydrogen Atom by a Microwave Method", Phys. Rev. **72**, 241 (1947).

[25] D. Hanneke, S. F. Hoogerheide, and G. Gabrielse, "Cavity Control of a Single-Electron Quantum Cyclotron: Measuring the Electron Magnetic Moment", Phys. Rev. A **83**, 052122 (2011).

[26] W. Pauli, "Zur alteren und neueren Geschichte des Neutrinos", Naturforsch. Ges. Zurich **102**, 387 (1957).

[27] C. L. Cowan and F. Reines, "The Neutrino", Nature **178**, 446 (1956).

[28] Y. Fukuda *et al.* (Super-Kamiokande Collaboration), "Evidence for oscillation of atmospheric neutrinos", Phys. Rev. Lett. **81**, 1562 (1998).

[29] M. Gell-Mann, "A Schematic Model of Baryons and Mesons", Phys. Lett. **8**, 214 (1964).

[30] C. S. Wu *et al.*, "Experimental Test of Parity Conservation in Beta Decay", Phys. Rev. **150**, 1413 (1956).

[31] A. Salam and J. C. Ward, "Electromagnetic and Weak interactions", Phys. Lett. **13**, 168 (1964).

[32] S. Weinberg, "A Model of Leptons", Phys. Rev. Lett. **19**, 1264 (1967).

[33] G. Arnison *et al.* (UA1 Collaboration), "Experimental observation of isolated large transverse energy electrons with associated missing energy at $\sqrt{s} = 540\,\text{GeV}$", Phys. Lett. B **122**, 103 (1983).

[34] LWG, "LEP Design Report", (1984), CERN-LEP/84-01.

[35] B. Adeva *et al.* (L3 Collaboration), "Measurement of Electroweak Parameters from Hadronic and Leptonic Decays of the Z^0", Z Phys. **51**, 179 (1991).

[36] E. Noether, "Invariante Variationsprobleme", Nachr. v. d. Ges. d. Wiss. zu Gttingen 235 (1918).

[37] M. Livio, "The Equation That Couldn't Be Solved: How Mathematical Genius Discovered the Language of Symmetry", (2005).

[38] V. Rubakov, *Classical Theory of Gauge Fields*, 1st ed. (Princeton University Press, 2002).

[39] I. J. R. Aitchison and A. J. G. Hey, *Gauge Theories in Particle Physics*, 3rd ed. (Taylor and Francis Group, 2003).

[40] J. Alitti *et al.* (UA2 Collaboration), "A measurement of the W and Z production cross sections and a determination of Γ_W at the CERN $p\bar{p}$ collider", Phys. Lett. B **276**, 365 (1992).

[41] S. Schael *et al.* (LEP Collaborations), "A Combination of Preliminary Electroweak Measurements and Constraints on the Standard Model", (2002), arXiv:hep-ex/0112021v2.

[42] I. Abt *et al.* (H1 Collaboration), "The H1 Detector at HERA", Nucl. Instr. and Meth. A **386**, 310 (1997).

[43] M. Derrick *et al.* (ZEUS Collaboration), "Initial Study of Deep Inelastic Scattering with ZEUS at HERA", Phys. Lett. B **303**, 183 (1993).

[44] J. D. Bjorken, "Asymptotic Sum Rules at Infinite Momentum", Phys. Rev. **179**, 1547 (1969).

[45] G. Hinshaw *et al.* (WMAP Collaboration), "Five-year Wilkinson Microwave Anisotropy Probe observations: Data processing, sky maps, and basic results", Astrophysical Journal Supplement **180**, 225 (2009).

[46] F. Zwicky, "Die rotverschiebung von extragalaktischen nebeln", Hel. Phys. Acta **6**, 110 (1933).

[47] V. C. Rubin and W. K. F. Jr., "Rotation of the Andromeda Nebula from a Spectroscopic Survey of Emission Regions", Astrophysical Journal **159**, 379 (1970).

[48] D. Clowe *et al.*, "A direct empirical proof of the existence of dark matter", Astrophysical Journal **648**, L109 (2006).

[49] D. S. Akerib *et al.* (CDMS Collaboration), "Low-threshold analysis of CDMS shallow-site data", Phys. Rev. D **82**, 122004 (2010).

[50] I. J. R. Atchinson, *Supersymmetry in Particle Physics: An Elementary Introduction*, 1st ed. (Cambridge University Press, 2007).

[51] M. Tetwort, "Searches for GMSB at the LHC", (2008), arXiv:0805.2524v2.

[52] A. Garcia-Bellido, "Searches for gauge mediated supersymmetry breaking at ALEPH with centre-of-mass energies up to 209 GeV", (2002), arXiv:hep-ex/0212024v1.

[53] V. M. Abazov *et al.* (D0 Collaboration), "Search for supersymmetry in di-photon final states at $\sqrt{s} = 1.96 TeV$", Phys. Lett. B **659**, 856 (2008).

[54] T. Aaltonen *et al.* (CDF Collaboration), "Search for Supersymmetry with Gauge-Mediated Breaking in Diphoton Events with Missing Transverse Energy at CDF II", Phys. Rev. Lett. **104**, 011801 (2010).

[55] G. Aad *et al.* (ATLAS Collaboration), "Search for Diphoton Events with Large Missing Transverse Energy with $36\,\mathrm{pb}^{-1}$ of $7\,\mathrm{TeV}$ Proton-Proton Collision Data with the ATLAS Detector", Eur. Phys. J. C **17**, 1744 (2011).

[56] V. I. Klyukhin *et al.*, "Measurement of the CMS magnetic field", IEEE Trans. on appl. Superc. **18**, 395 (2008).

[57] S. Chatrchyan *et al.* (CMS Collaboration), "Precise mapping of the magnetic field in the CMS Barrel Yoke using cosmic rays", JINST **5**, T03021 (2009).

[58] S. Chatrchyan *et al.* (CMS Collaboration), "A Review of clustering algoritms and energy corrections in the Electromagnetic Calorimeter", (2010), CMS-IN-2010/008.

[59] M. Cacciari, G. P. Salam, and G. Soyez, "The anti-k_t jet clustering algorithm", JHEP **2008**, 063 (2008).

[60] S. Chatrchyan *et al.* (CMS Collaboration), "Performance of Jet Algorithms in CMS", (2007), CMS-PAS-JME-07-003.

[61] T. Sjostrand, S.Mrenna, and P. Skands, "Pythia 6.4 Physics and Manual", JHEP **05**, 026 (2006).

[62] S. Agostinelli *et al.* (GEANT4 Collaboration), "GEANT4 – a simulation toolkit", Nucl. Instr. and Meth. A **506**, 250 (1988).

[63] S. Chatrchyan *et al.* (CMS Collaboration), "Isolated Photon Reconstruction and Identification at $\sqrt{s} = 7\,\mathrm{TeV}$", (2011), CMS-PAS-EGM-10-006.

[64] S. Chatrchyan *et al.* (CMS Collaboration), "Measurement of CMS Luminosity in the 2010 Run", (2010), CMS-AN-AN-2010/175.

[65] S. V. der Meer, "Callibration of the Effective Beam Height in the ISR", (1968), ISR-PO/68-31.

[66] T. Junk, "Confidence level computation for combining searches with small statistics", Nucl. Inst. Meth. A **434**, 435 (1999).

[67] A. Read, "Modified frequentist analysis of search results (the CLs method)", (2000), Technical Report CERN-OPEN-2000-005.

[68] G. Aad *et al.* (ATLAS and CMS Collaborations), "Procedure for the LHC Higgs boson search combination in Summer 2011", (2011), ATL-PHYS-PUB/CMS NOTE 2011-11, 2011/005.

[69] G. Davies *et al.* (TEVNPH Working Group), "Combined CDF and D0 Searches for Standard Model Higgs Boson Production", (2012), arXiv:1203.3774v1.

[70] S. Chatrchyan *et al.* (CMS Collaboration), "A search using multivariate techniques for a standard model Higgs boson decaying into two photons", (2012), CMS-PAS-HIG-12-001.

[71] S. Chatrchyan *et al.* (CMS Collaboration), "Search for Supersymmetry at the LHC in Events with Jets and Missing Transverse Energy", Phys. Rev. Lett. **107**, 221804 (2011).